Nanoscale

Recent Progress in 2D Hybrid Heterostructures from Transition Metal Dichalcogenides and Organic Layers: Properties and Applications in Energy and Optoelectronics

Journal:	*Nanoscale*
Manuscript ID	NR-REV-03-2022-001358.R1
Article Type:	Review Article
Date Submitted by the Author:	14-Jun-2022
Complete List of Authors:	Ji, Jaehoon; Purdue University, Mechanical Engineering Choi, Jong Hyun; Purdue University, Mechanical Engineering

Recent Progress in 2D Hybrid Heterostructures from Transition Metal Dichalcogenides and Organic Layers: Properties and Applications in Energy and Optoelectronics

Jaehoon Ji and Jong Hyun Choi*
School of Mechanical Engineering, Purdue University
West Lafayette, Indiana 47907, United States
*Corresponding author: jchoi@purdue.edu

Abstract

Atomically thin transition metal dichalcogenides (TMDs) present extraordinary optoelectronic, electrochemical, and mechanical properties that have not been accessible in bulk semiconducting materials. Recently, a new research field, 2D hybrid heteromaterials, has emerged by integrating TMDs with molecular systems including organic molecules, polymers, metal-organic frameworks, and carbonaceous materials that can tailor the TMD properties and exploit synergetic effects. The TMD-based hybrid heterostructures can meet the demands of future optoelectronics, including flexible, transparent, and ultrathin devices, and energy applications offering high energy and power densities with a long cycle life. To realize such applications, it is necessary to understand the interactions between the hybrid components and to develop strategies for exploiting the distinct benefits of each component. Here, we overview the current understanding of new phenomena and mechanisms involved in TMD/organic hybrids and the potential applications harnessing such valuable materials in an insightful way. We highlight recent discoveries in the multicomponent hybrid materials. Finally, we conclude this review by discussing the challenges with the hybrid heteromaterials and presenting future directions and opportunities in this research field.

Keywords

Transition metal dichalcogenides, 2D materials, hybrid heterostructure, organic layer, optoelectronics, energy

ORCID

Jaehoon Ji: 0000-0003-2372-8566
Jong Hyun Choi: 0000-0002-0507-3052

1. Introduction

Two-dimensional (2D) materials have attracted great attention for the fundamental studies of low-dimensional physics and various designs of novel devices.[1, 2] Among the 2D families, transition metal dichalcogenides (TMDs) such as MoS_2, $MoSe_2$, WS_2, and WSe_2 exhibit promising semiconducting properties, including sizable bandgaps and fast carrier mobilities.[3] These are the highly desirable properties to build atomically thin (opto)electronic applications and complement other 2D layers, such as graphene (semimetal) and hexagonal boron nitride (insulator).[4, 5] Thanks to the semiconducting characteristics, a MoS_2 based field-effect transistor (FET) was first introduced in 2007.[6] Since then, the research on atomically thin TMDs has advanced at an astonishing pace, with the aim to overcome the challenges in scaling down bulk semiconductor devices including short-channel effects, current leakage, and high power consumption in a limited area.[7-9] The bandgaps of ultrathin TMDs corresponding to the energy levels of the visible spectrum of light are adequate to develop versatile optoelectronics, such as photovoltaic energy harvesters, phototransistors, light-emitting diodes (LED), and photodetectors.[10-12] In addition to the exceptional optoelectronic properties, the atomically thin TMDs offer high mechanical strength, flexibility, and light-weight, which may be utilized to develop flexible and wearable devices.[13, 14]

Looking beyond individual 2D materials, a new research field of heterostructures from dissimilar ultrathin TMDs has emerged, expecting synergetic effects between constituent flakes.[15-19] Due to the various combinations of 2D layers, the artificially stacked hetero-layers held by interlayer van der Waals (vdW) interaction exhibit versatile architectures and distinct properties for potential applications. For example, 2D MoS_2/WSe_2 heterojunctions can be prepared by stacking MoS_2 and WSe_2 monolayers. Given their properties as electron- (n-type; MoS_2) and hole-rich (p-type; WSe_2) semiconductors, the heterojunctions display rectifying current-voltage (CV) behaviors, which may not be achieved by the individual TMDs.[20] Unlike conventional materials that require an entirely matched lattice growth, the vdW heterostructures may be constructed via various design schemes with different interlayer distance, twisted angles, and Moiré patterns of constituent layers.[21-24] The additional degrees of freedom in the methods allow excellent tunabilities in the heterojunctions. The Moiré patterns in $MoSe_2/MoS_2$ hetero-layers, for instance, display periodic interlayer potentials and split the energy levels of excitonic transitions.[21] The heterostructures are not just limited to the vertically stacked vdW junctions; they may also be prepared with different chemistries such as covalent and ionic interactions.[18, 25, 26] For example, heteromaterials made of MoS_2 covalently

bonded to graphene can be utilized for energy storage thanks to the high ion capacity of MoS_2 and the high conductivity of graphene.[27, 28] Thus, the TMD-based heterostructures may open many possibilities for discovering new physics and developing novel applications.

While the science on TMDs and TMD-based heterostructures has advanced tremendously over the past decade, the field has not matured yet, and numerous challenges remain unresolved for realizing TMD-based practical applications.[25, 29, 30] For example, reliable and scalable synthesis of the materials and controllable doping for tuning the carrier types and amounts must be addressed to fabricate 2D-material-based market products. Organic-integrated 2D hybrid heterostructures have been proposed to address the issues. Molecular systems, including organic molecules, polymers, metal-organic frameworks (MOFs), and carbonaceous composites, are suitable for low-cost production and scalable synthesis.[30, 31] The molecular systems may be integrated with TMDs and TMD-based heterostructures via vdW forces, covalent chemistry, or electrostatic interaction.[32] For example, TMD/organic hybrid structures can be formed by simply dipping the substrate-supported TMDs into the organic molecule-containing solution at room temperature.[33, 34] This will enable facile mass production of TMD/organic hybrid structures. Moreover, a wide range of organic-integrated TMD hybrids are possible, given the extensive library of organic molecules to meet various demands of applications.[35-37]

In contrast to the conventional doping (e.g., ion implantation and diffusion) that may impair the crystalline structures of ultrathin TMDs, the carrier types and amounts in TMDs can be modulated by organic functionalization without damaging the 2D flakes.[38] The organic molecules interfacing the TMD flakes may lead to several distinct interlayer charge transfer processes, depending on the energy level difference between the reduction/oxidation potentials of the molecular system and the work functions of ultrathin materials. Furthermore, due to the soft nature of organic and polymer layers, the organic functionalized TMD hybrid structures may be utilized for flexible devices.[37] Lastly, organic layers can play a role in passivating defects in TMDs.[39, 40] Defects (e.g., vacancies and adatoms) in atomically thin crystals may deteriorate the optoelectronic properties, leading to unexpected degradation of the device performances.[41] The defects can be controlled via chemical reactions between TMDs and organic layers, where the molecules may fill the vacancies or remove the adatoms with covalent reactions.

This article will discuss the state-of-the-art in the organic-integrated TMDs and TMD-based heterostructures. It is worth noting that the studies of 2D materials are incredibly vast, and this work will not cover the entire field. The scope of this review includes the fundamental properties and mechanisms of organic-integrated TMD hybrids and their applications. Especially, we will introduce the most recent advances in the multicomponent hybrid structures. In section 2, we discuss the fundamental properties of TMDs and TMD-based heterostructures. The discussion will also include why organic functionalization is desirable for tuning the properties of TMDs and how the interactions between TMDs and organic layers lead to synergetic outcomes for (opto)electronic and energy devices. In section 3, various properties of organic-embedded heterostructures are presented, including dielectric screening, doping, dipole interaction, and interfacial chemistry between organic layers and ultrathin materials. Section 4 highlights the applications of organic-functionalized TMD hybrid heterostructures, including phototransistors, photovoltaics, LED, and optical memories as well as energy storage devices such as supercapacitors and catalysts for energy applications. Lastly, we conclude with current opportunities and challenges that will be worth exploring to advance 2D materials science and technology.

2. Overview of Organic-TMD Hybrid Materials

2.1. TMDs

TMDs indicate a family of materials with the formula MX_2, consisting of a transition metal (M = Mo, W, Re, etc.) and chalcogen atoms (X = S, Se, or Te).[31] The transition metal is sandwiched by two chalcogen atoms via a strong covalent bond. The MX_2 crystals form layered structures with relatively weak vdW interaction between the layers. Such layered materials exhibit two common symmetries: hexagonal (1H or 2H) and tetragonal (1T) geometries.[3] The polytypes of geometries determine the electronic properties of TMDs. For example, 1T-MoS_2 shows a metastable metallic nature which tends to be converted to the stable hexagonal phases with semiconducting properties.[42] The layered features allow one to exfoliate TMDs in various ways. For example, mechanical exfoliation of bulk crystals using sticky tapes, termed ‘scotch-tape method’, has been widely adopted to prepare atomically thin TMDs with minimal structural disruption and defects.[9] TMDs can be chemically exfoliated into thin flakes in solutions by ion intercalation or ultrasonication methods, which have the potential for large scale manufacturing.[10, 25] Besides the top-down preparation techniques, bottom-up growth approaches are also available, including chemical vapor deposition (CVD) or solvothermal synthesis.[43, 44] TMDs with a few tens of micrometers in size have been demonstrated with the

CVD method for optoelectronic devices.[43, 45, 46] Here, TMD flakes are formed by chemical reaction of volatile precursors containing transition metal and chalcogen atoms on various substrates under well-controlled environments with low pressure and high temperature.[45] TMD nanomaterials may also be prepared in a hot pressurized vessel that allows the chemical reaction between the hetero-atoms in an aqueous solution.[47-49] This approach may enable a scalable production of TMDs with various morphologies, including edge-rich flower-like nanostructures,[49] hollow tubular structures,[50] and agglomerated nanoparticles.[51] More detailed discussions on the TMD fabrication can be found elsewhere.[43, 44, 52]

Semiconducting 2D TMDs possess promising properties for optoelectronics and spintronics. The bandgaps of TMDs depend on several factors such as the constituent elements[53-55] and layer number.[34] TMD monolayers have direct bandgaps that are larger than those of the bulk crystals with indirect gaps. The monolayers show stronger photoluminescence (PL) with large exciton binding energies (few hundreds of meV), allowing for stable formation of excitons around room temperature.[34, 56-58] Monolayer (1L) TMDs also have strong piezoelectric coupling of charges, which may be adopted for low-power electronics.[59] Another unique feature of monolayer 2H-TMDs is that they exhibit broken inversion symmetry that results in a large valley splitting in energy band and a strong spin valley coupling.[60] This may allow for electrical and magnetic manipulation of charge carriers in spin-based devices. In addition, the layered nature of TMDs provide distinct advantages for energy applications. Atomically thin TMDs exhibit large surface areas, and their stacked lamellar structures may store ions between adjacent layers, thus having high ion capacity for energy storage devices.[26]

2.2. TMD-based Heterostructures

Combining different 2D materials as heterostructures can further expand the boundary of the physics in ultrathin materials and open new doors for future applications.[15] Figure 1a illustrates 2D TMD heterostructures made of dissimilar layers.[61] With a proper combination of the components, it is possible to fabricate atomically thin heterostructures for high-performance, low-power-consumption electronic devices.[2, 58] For example, p-n junctions that are fundamental building blocks for electronics can be prepared by integrating an n-type MoS_2 layer with a p-type WSe_2 flake. As atomically thin heterostructures may not form charge depletion layers, vdW p-n junctions such as WSe_2/MoS_2, $MoTe_2/MoS_2$, and WSe_2/WS_2 exhibit unique anti-ambipolar behaviors that are rarely found in bulk electronics.[62-64] The devices demonstrate a local maximum conductance at a particular gate potential, which is different

from typical ambipolar characteristics.[64] Such a unique behavior may be harnessed to build new electronic applications including neuromorphic devices, ternary logic circuits, and gate-tunable diodes.[65-67] TMD sandwiched by top and bottom graphene layers (i.e., graphene/WS_2/graphene) in Figure 1b performs as a vertically tunneling FET with a high on/off ratio (~10^6) and a small subthreshold swing (below 60 meV/decade), enabling a low power consumption operation of FET.[68, 69] Here, TMD serves as a tunneling barrier, while graphene has a role of a charge injecting layer.

TMD/TMD heterostructures exhibit exciting phenomena arising from strong light-matter interactions. As shown in Figure 1c, an interlayer exciton (IX), a bound state of an electron and a hole separately residing in opposite layers, is observed in type II TMD/TMD heterostructures.[70] This is distinct and different from the intralayer excitons confined in the individual layers.[22, 24, 70] The PL emissions from individual WSe_2 and $MoSe_2$ flakes are observed from 1.6 to 1.75 eV (see the top and bottom panels). In contrast, the $MoSe_2$/WSe_2 heterostructure exhibits an additional peak near 1.4 eV from the radiative recombination of IX. Figure 1d illustrates the interlayer emission process in the $MoSe_2$/WSe_2 heterobilayer.[71] The photoexcited electron in WSe_2 is transferred to $MoSe_2$, while the hole in $MoSe_2$ migrates to WSe_2 due to the staggered band alignment. The spatially separate electron-hole pair in the heterolayers has strong Coulombic interactions which lead to a large binding energy (~100 meV) and stable PL emission with a long lifetime (~100 ns) and a scalable diffusion length (~a few μm).[21, 70, 72, 73] These characteristics may allow one to harness IX as a new class of information carrier similar to charges in FET. If the bound charges are aligned in a particular direction, for example, they may behave as aligned dipoles which can be electrically controlled in excitonic devices.[74]

TMD heterolayers can be prepared by several methods, including (i) mechanical stamping with an elastomer, (ii) consecutive CVD growth, and (iii) solution phase synthesis.[15, 18, 20] (i) The constituent layers in a heterostructure may be prepared from separate micromechanical exfoliations and stacked by stamping against each other with an elastomeric polymer.[18] For example, a TMD layer can be positioned in a desired location of an elastomer such as polydimethylsiloxane (PDMS), which may then be placed on top of another 2D flake on a silicon substrate using a position manipulator. This method often produces high-quality specimens suitable for the fundamental studies of materials properties. (ii) For scalable manufacturing, sequential growth of constituent layers with CVD methods may be favored.

Several TMD/TMD heterobilayers with sizes of several tens of micrometers were demonstrated, including MoS_2/WS_2, MoS_2/WSe_2, and $SnSe_2/MoS_2$ as well as TMD/other-2D-flake (e.g., hBN/MoS_2 and graphene/MoS_2).[75] (iii) Hetero-assemblies may also be prepared by co-dispersing different TMD flakes in a solution.[76, 77] With the vdW interaction between the colloidal flakes, the layers can constitute a heterostructure. Yun et al. demonstrated this approach by flocculating MoS_2 and WSe_2 flakes into self-assembled homo- and hetero-layers.[77] The approach could be adopted for cost-effective ink-printing electronics.

2.3. Organic-integrated TMD Hybrids

The TMDs and TMD-based heterostructures show various promising properties which may be exploited for future applications. Despite the significant efforts in recent years, the studies are still in the early stage. Numerous challenges remain unaddressed, which may be classified into three distinct categories: (i) fabrication difficulties, (ii) necessity of doping, and (iii) engineering environmental conditions. First, individual TMD structures may be prepared by mechanical exfoliation, CVD, or solvothermal synthesis. Manual stacking of micromechanically exfoliated TMD flakes for heterostructures can produce high quality samples; however, it requires a series of laborious preparation steps which may be handled only by skillful operators. This is not desirable for industrial fabrication.[15] The CVD-based approaches may ameliorate the difficulties.[43] However, the methods offer only a few limited combinations of hetero-assemblies, and the synthesized samples often bear structural defects and imperfection. The heterolayers constructed by solution phase methods may have inhomogeneous properties such as different layer numbers and sizes as well as uncontrolled stacking of multiple flakes.[76]

Second, the behavior and performance of electronic and optoelectronic devices depend highly on the charge carrier type and concentration in semiconducting channel layers.[25] Thus, it is crucial to control the charges in TMD-based heterostructures with efficient doping processes. Conventional doping techniques widely accepted for silicon-based devices include thermal diffusion and ion implantation. These methods, however, may not be useful for atomically thin materials, as they could damage the TMD layers significantly.[29] Lastly, due to the 2D nature and quantum confinement, TMDs and TMD-based heterostructures are extremely sensitive to their local microenvironments. For example, MoS_2 transistors prepared on silicon (Si)/silicon dioxide (SiO_2) substrates demonstrate poor mobility and on/off behaviors compared with those

on hBN, because of dielectric inhomogeneity and trapped charges in Si/SiO_2.[78] In addition, the inherent defects in TMDs such as vacancies and adatoms may influence the device performances, thus a proper interfacial engineering should be applied to control the defects.

The integration of 2D materials with organic molecular systems has been explored as a promising approach to address the challenges discussed above.[25, 29, 30, 79] The molecular systems include organic molecules, polymers, and metal-organic frameworks (MOF). They offer several distinct advantages for 2D materials. Unlike the challenging 2D material fabrication, a wide range of organic molecules can be prepared at large scale and low cost.[35, 36] They may be further customized to meet various requirements of applications. The organic functionalization on 2D layers is a non-destructive and defect-free process of doping, which can control the charge density and polarity in the TMDs. Moreover, TMD/organic systems may be designed to exploit synergetic effects of TMDs and organic layers.[36, 80-84] For example, environmentally switchable molecules including photo-, electro-, chemo-, and thermo-sensitive molecules may provide additional tunability on TMD-organic hybrid structures.[85-88] Photochromic molecules can change their conformations with external light stimuli (e.g., UV and visible light), and their energy levels are modulated accordingly.[67] With the switching behaviors, the functionalized molecules may control the interlayer charge transfer at the TMD/organic interface. Such properties could make the hybrid heterostructures useful as optical memory applications (see section 4.1).

The TMD interfaces may also be engineered with the organic adlayers. For example, the organic layers (e.g., fluoropolymer) can perform as a low dielectric layer for TMD FETs, when coupled with a high dielectric film (e.g., Al_2O_3).[89] The complex dielectric system may increase the carrier mobility and reduce the subthreshold swing by minimizing unwanted scattering of charges. Organic layers may also be used for tuning the dielectric screening on the charges. The screening can significantly affect the energy level of excitons by modulating their binding energies, ultimately leading to shifts in emission wavelength.[90, 91] Furthermore, organic molecules can passivate the defects in TMDs by filling vacancies and removing adatoms with covalent chemistries.[29] Generally, the defect-engineered TMDs exhibit an enhanced carrier mobility and an improved PL quantum yield.[38, 92] Lastly, it was recently reported that the organic functionalization may tailor not only the properties of the individual layer but also the interlayer interaction in the TMD-based heterojunctions such as TMD/TMD, TMD/graphene, and TMD/hBN.[90, 93, 94] The organic layers embedded in the multicomponent hetero-assemblies

can control the interlayer charge and energy transfer.[93, 94] The embedded molecular systems also modify the emission characteristics of IX in TMD/TMD heterostructures by converting the charge transfer pathways from tunneling to type II junction-supported transport and modulating the dielectric screening strength.[90]

The organic functionalization on TMDs may be categorized into two groups: covalent and noncovalent methods.[25, 29-31] The physisorption of organic layers may occur on smooth surfaces of crystalline structures without significant dangling bonds, leading to stable vdW interaction between TMDs and organics. The examples include solution-based processes, including drop casting, spin coating, and simple immersion of the substrate-supported TMDs (Figures 2a-c).[95, 96] The organic layers may behave as a donor or acceptor for TMDs depending on the energy level difference between the redox potentials of the organics and the TMD work functions. Chamlagain et al. reported that benzyl viologen (BV) molecules deposited on a MoS_2-based device by immersion can serve as a donor for MoS_2, thereby controlling the carrier density.[95] Here, the BV's redox potential is higher than the work function of MoS_2, where the electron transfer from the molecular system to MoS_2 is favorable. Organic molecules may also be deposited on various 2D layers by gas-phase processes, such as molecular beam epitaxy (or thermal vapor deposition) as illustrated in Figure 2d.[97-99] For instance, perylene tetracarboxylic dianhydride (PTCDA) and titanyl phthalocyanine (TiOPc) can be evaporated in a low-pressure chamber, and the vaporized molecules may form a uniform layer on 2D layers.[98, 99]

Furthermore, the molecular systems may form self-patterned layers in a particular shape, which is attributed to the strong intermolecular interaction and the relatively weak interaction between 2D materials and organic molecules.[96, 100-103] For example, Wang et al. demonstrated that oleamide molecules on TMDs form interesting nanoribbon patterns with an angle of ~120 degrees in three directions as illustrated in Figure 3a.[96] Figure 3b shows the AFM images of such self-patterned oleamide nanoribbons on $MoSe_2$ (top) and WSe_2 (bottom), where the nanoribbons are aligned with 3-fold symmetry on TMD layers. They attributed this phenomenon to the tip-to-tip interaction between oleamide molecules. Other molecules with strong intermolecular interactions such as PTCDA and 2,3-diaminophenazine (DAP) were shown to form herringbone patterns on 2D materials.[100, 101] In addition, Lin et al. demonstrated that pentacene and iron phthalocyanine (FePc) could cluster and form assemblies on 1H phase of $PtSe_2$ but not on 1T metallic phase, because of the higher electron affinity of 1H phase resulting in a stronger electrostatic interaction with the organic system.[102]

Beside vdW interactions, the TMD/organic heterointerfaces may be constructed with covalent chemistry.[92, 104-109] The covalent functionalization can be divided into defect-mediated and phase-assisted processes which are illustrated in Figures 3c and 3d, respectively.[104, 109] TMDs with inherent defects may react with functional groups in organic molecules. For example, MoS_2 may have sulfur vacancies or adatoms that can react with molecules bearing thiol groups.[92] The thiol groups form disulfide bonds with MoS_2 at the vacancy sites. Solution-based and vapor-deposition processes have been introduced for the reaction.[25] It was demonstrated that MoS_2 could be decorated with 4-amino thiophenol (4ATP) and 4-nitro thiophenol (4NTP) by immersing MoS_2 phototransistors in the solutions containing the molecules.[105] The functionalized phototransistors exhibited a greater photoresponsivity due to the engineered band structure. With a similar covalent, yet distinct method, Cho et al. reported that thiol-molecules such as decanethiol (DT) and perfluorodecanethiol (PFDT) deposited by thermal evaporation provided tunneling paths on MoS_2-based electronic devices and improved charge injection behaviors.[108] The phase-assisted process was first introduced by Voiry et al.[109] The metastable 1T-phase MoS_2 prepared via liquid exfoliation by butyllithium intercalation showed electron-rich characteristics. The 1T-MoS_2 facilitated charge transfer to organic halides, resulting in the covalent binding of the organic halides covering up to 30 % of the MoS_2 surface. The stable functionalization drastically modified the optoelectronic properties of the TMD layer, generating a strong PL.

3. Properties of Hybrid Structures

3.1. Dielectric screening

Ultrathin TMDs have strong Coulomb interactions between charge carriers due to a weak self-dielectric screening originating from the quantum confinement effects (i.e., 2D limit).[110] This brings out many unique optoelectronic properties of TMDs, including a significant renormalization of the electronic energy levels and high binding exciton energies. Since the extraordinary properties are strongly affected by the dielectric conditions of TMDs, significant efforts have been devoted to tailoring their local dielectric environments.[89, 111, 112] Molecular systems are excellent candidates for achieving the goals. For example, the bandgap of 2D materials may be renormalized by the dielectric screening due to organic-layer-induced surface polarization.[113] As illustrated in Figure 4a, the charges in the 2D semiconducting layer encapsulated with a dielectric (red box) may experience a weaker electric field than those without the dielectric layer.[110] Given the weakened electric fields (i.e., increased dielectric

screening), the charges may consequently possess a reduced self-energy. As a result, the energy level difference of charges in the conduction band minimum (CBM) and valance band maximum (VBM) (i.e., bandgap) may be smaller at the heterointerface as shown in Figure 4a. Winkler et al. reported the renormalization behavior of bilayer MoS_2 by intercalating TiOPc molecules. They estimated that the organic-molecule-inserted MoS_2 bilayer has a smaller bandgap by ~0.3 eV than pristine MoS_2.[114] The bandgap renormalization due to the dielectric screening have been discussed in detail elsewhere.[113, 115, 116]

The electrostatic interaction of charges in the 2D layers may be inversely proportional to the dielectric strength.[90, 111] Excitons in a TMD layer covered with an organic layer may experience a stronger dielectric screening and, accordingly, a weaker Coulomb interaction than those exposed to air. The phenomenon is attributed to a higher dielectric constant of the organic layer than that of the air. For example, an organic layer made of eosin Y (EY) may have a relative dielectric constant ($\varepsilon \approx 3$), greater than that of the air ($\varepsilon \approx 1$).[117] Given the increased dielectric screening with the organic layer, the excitons in the TMD/organic may have a smaller binding energy than those in the TMD/air, as shown in Figure 4b. The interplay of screening-induced changes in the bandgap (E_G) and the exciton binding energy (E_B) will determine the PL emission energy (E_E) of a TMD sample.[113, 118]

$$E_E = E_G - E_B \quad (1)$$

As illustrated in Figure 4b, the TMD under stronger dielectric screening effects may be renormalized to have a reduced bandgap energy. Its exciton binding energy may also be diminished, eventually having a reduced emission energy and exhibiting the redshifted PL.

As an example, Figure 4c demonstrates the PL spectra of 1L MoS_2 with and without an EY layer.[90] The 1L MoS_2 flake covered with an EY layer exhibits its PL emission peak at ~660 nm, which is approximately 6 nm longer (or lower emission energy by ~17 meV) than that of MoS_2/air. In Figure 4c, another noticeable change in the PL spectra of the TMDs in the presence of the organic layer is the PL intensity difference. This may be attributed to the doping effects at the TMD/organic interface, which will be discussed in section 3.2.

In addition to the bandgap engineering and the binding excitons energies in TMDs, dielectric polymers have been explored to minimize unwanted phonon scattering on the charges. Chamlagain et al. reported a $MoSe_2$ FET on a parylene layer (CYTOP®) (Figure 4d).[112] The

organic layer attenuated phonon scattering from the bottom Si/SiO_2 substrate. The TMD/organic device showed a higher electric conductivity than the pristine TMD FET as shown in Figure 4e. The hybrid demonstrated a three-times faster carrier mobility than the control sample. A similar behavior was observed by Shokouh and coworkers.[89] A WSe_2 transistor with a gate dielectric made of sapphire and fluoropolymer showed a high hole mobility of ~100 cm^2/Vs with an on/off ratio > 10^7. The device also demonstrated good stability in ambient air with a relative humidity of 45 % for over 7 days. They attributed the high performance to the reduced phonon scattering and the moisture protection by the organic layer.

3.2. Doping

Doping is one of the most effective ways to tune electronic and optoelectronic properties of semiconducting materials. The success of traditional silicon technologies is partly hinged on the doping-friendly properties of silicon. Its carrier type and density can be efficiently controlled with several doping techniques, including ion diffusion and implantation.[119, 120] Such methods can convert silicon channels into non-degenerate or degenerate p- and n-type materials for various purposes. However, the conventional strategies may not be useful in tailoring (opto)electronic properties of 2D TMDs. The processes may deteriorate the TMD structures severely, introducing several unwanted effects such as a decrease of the charge mobility and additional defects in the layer.[121, 122] Therefore, it is necessary to develop sophisticated and reliable doping methods for 2D materials.[11, 123] Organic molecules are potential candidates to achieve non-destructive doping on 2D TMDs, where interlayer charge transfer may be induced at the interface between TMDs and molecular layers. Here, we classify the molecule-induced doping into two distinct mechanisms: dark-state doping and dipole-induced charge transfer. Table 1 highlights the interactions between various TMDs and molecular systems as well as the methods used for preparing the hybrid structures.

Dark-state doping refers explicitly to the interlayer charge transfer at the TMD/organic interface without illumination.[7, 29, 30, 33, 38, 95, 124] The process is determined by the energy level difference between the redox potential of the organic system and the work function of TMDs. Here, the redox (i.e., reduction/oxidation) potentials indicate the energy levels of the organic system (e.g., organic molecules, layers, frameworks, and polymers) to withdraw or donate charges to any interfacing substrates. When the hetero-materials are brought into contact, the electrons in one layer with a higher potential may flow to the opposite layer. For example, if the redox potential of the molecule is higher than the TMD work function, the electrons in the

organic layer can spontaneously migrate to the TMD as illustrated in Figure 5a. This represents an n-doping process, where the molecules are electron donors. The doping process with an opposite energy level alignment is a p-doping, where the organic system withdraws electrons from TMDs, as presented in Figure 5b.

With the organic-induced doping, both carrier type and density in TMDs can be modulated. For example, Kirya and coworkers demonstrated an n-doping on MoS_2 by decorating BV on the mechanically exfoliated TMD layers (with a thickness of ~5 nm) via vdW interaction (Figure 6a).[125] Figure 6b shows that after the heavy n-doping the BV-coated MoS_2 transistor exhibited a current of ~10^{-4} A under a gate potential of -40 V at a source-drain voltage (V_D) of 1V. The electron density after the BV-assisted doping was estimated to be ~1×10^{13} cm^{-2}. The undoped, pristine MoS_2 transistor generated six orders magnitude smaller current under the same operating conditions because of the insufficient amount of charge carriers. Benjamin et al. demonstrated a drastic switching of major carrier types in TMD FETs by functionalizing metalated tetra-sulfonic-phthalocyanine (TsPc) molecules.[126] Figure 6c shows that a Na_2TsPc-attached WSe_2 FET demonstrated suppressed p-branch currents and enhanced n-branch currents. The threshold voltage transitioned from ~10 V to ~-10 V after the functionalization. Here, the threshold value was determined by finding the gate-voltage axis intercept at zero current from the linear extrapolation in the current-voltage curve. This indicates that the hole-rich condition of the device may have been converted into the n-type. Figure 6d shows a completely opposite modulation of the carrier type in a MoS_2 FET. The polarity of the MoS_2 channel was switched from n-type to p-type by functionalization of CuTsPc. The Cu-chelated TsPc may lower the work function of MoS_2 due to the p-doping effects, resulting in the shift of the carrier polarity.

Beyond the effects on individual TMD layers, the organic functionalization may also control the electronic properties of TMD-based heterostructures.[33, 94] For example, Kim et al. reported that the hole conductance of WSe_2/MoS_2 p-n heterojunction FETs may be enhanced by functionalizing poly(methyl methacrylate-co-methacrylic acid) (PMMA-co-PMAA) on the TMD heterolayers (Figure 6e). The p-doping on the heterojunction increased the hole current and broadened the region of anti-ambipolar FET characteristics. They reported that the range of the voltage window showing the anti-ambipolar behavior was expanded from ~15 V without functionalization to ~25 V with the organic layer. Due to the p-doping effects, the potential

window of hole dominant current in the organic-layer-attached p-n junction spans from −56 V to −37 V (Figure 6f), which is two times wider than that (−64 V to −55 V) of TMD-only heterojunction.

The molecular doping may also affect the optoelectronic properties of TMDs. Under light illumination, a photoexcited electron may form a bound state with a hole (i.e., exciton). In addition to the charge-neutral excitons, negatively or positively charged excitons (termed trions) are also possible. The negatively or positively charged trions show the electron- or hole-rich nature of TMDs, respectively. The levels of neutral and charged excitons in TMDs can be controlled by the dark-state doping process. Figure 6g shows the effect of dark-state doping on the radiative recombination of excitons and trions in WS_2.[127] Peimyoo et al. demonstrated an effective p-doping on as-prepared n-type WS_2 via 2,3,5,6-tetrafluoro7,7,8,8-tetracyanoquinodimethane (F_4TCNQ) functionalization.[127] The as-prepared electron-rich WS_2 exhibits only trion emission at ~1.97 eV; in contrast, the doped WS_2 with a balanced level of electrons and holes shows both excitonic and trionic emissions at approximately 2.05 and 1.97 eV, respectively. It is worth noting that as the WS_2 sample was functionalized with F_4TCNQ multiple times (Figure 6h), the emission intensity increased correspondingly due to the increased quantum yield of exciton emission compared to that of trion transition.[128] Besides, the report included a small yet distinct change (~3 cm^{-1}) in the in-plane Raman shift (E^1_{2g}) from the p-doped sample compared to the control, which was attributed to the softened electron-phonon interaction.[129]

Organic molecules bearing electric dipoles may develop localized electric fields on ultrathin TMDs, modulating charge densities like applying gate voltage on semiconducting channels. Especially, the molecules with strong intermolecular interaction forming self-patterned layers on TMD surfaces give rise to aligned dipoles in a particular direction. The alignment may amplify the effects of dipole-induced potential. Several molecules have been introduced to induce the electric dipole moments on the semiconducting materials, including aminopropyltriethoxysilane (APTES), octadecyltrichlorosilane (OTS), octadecyltrichlorosilane (ODTS), Trichloro-(1H,1H,2H,2H-perfluorooctyl)silane (FOTS) and (3-mercaptopropyl)trimethosysilane (MPS).[130-132] Depending on the direction of the dipole moment, the molecular assemblies may lead to p- or n-doping on TMDs. For example, if an organic molecule develops a positive dipole moment (i.e., upward dipole) on a semiconductor, it may provide a p-doping effect. Kang and coworkers reported that approximately 1.4×10^{11}

cm^{-2} of electrons could be removed from a MoS_2 transistor after OTS functionalization, while APTES-attached WSe_2 gained electrons by ~10^{11} cm^{-2}.[130] They explained the OTS-induced doping with the schematic in Figure 7a. The TMD energy bands are twisted by the electrical dipole-induced potential on the TMD layer, which promotes the hole injection from the Pt electrode. With the injected positive charges, the transistor with the organic dipoles exhibits a higher current level than the control (Figure 7b). Accordingly, the threshold voltage (V_{th}) in the WSe_2 transistor transitions from ~-5 V to 5 V with the OTS functionalization. In contrast, V_{th} in the MoS_2/APTES sample is shifted to a lower voltage (Figure 7c), which is attributed to the dipole-induced n-doping. Wang et al. reported a similar dipole-induced doping on MoS_2 FETs.[133] They functionalized 2-fluoropyridine (2-FP) and 4-aminopyridine (4-AP) on 2D MoS_2 layers to induce a dipolar potential. They also inserted zinc phthalocyanine (ZnPc) layers between the functional molecules and the TMD layers to align the molecules in the same direction (downward dipole). Otherwise, the molecules would be randomly oriented and might not induce the net dipole effects. The aligned molecules can provide the negative dipole moments on the MoS_2 FET, thereby shifting the threshold voltage of the device to a lower voltage.

Dipole-induced doping may also impact the exciton emission by controlling the charge densities in ultrathin TMDs. A TMD monolayer with a balanced charge polarity will show stronger PL than those under electron- or hole-rich conditions. Najmaei and coworkers reported that MoS_2 flakes functionalized with self-assembled dipolar molecules such as MPS exhibited approximately four times greater PL intensity than the pristine MoS_2.[134] The dipolar molecule assembly may induce a p-doing on electron-rich MoS_2, which can promote the exciton formation, while suppressing the trions. As a result, brighter PL is observed from the p-doped MoS_2. Other examples of dipole-induced doping are listed in Table 1.

3.3. Photoinduced Charge and Energy Transfer

Molecular systems may build various energy level alignments with TMDs. A staggered band alignment may facilitate the interlayer charge transfer, while a straddling band can promote interfacial energy transfer from a larger energy gap material to a smaller one. The different types of the band alignment may present new ways of tunability that is not available with individual 2D materials and that governs the behaviors and functions of optoelectronics and energy devices.[98, 135, 136] Figure 8a illustrates a staggered energy level alignment (i.e., type II) between TMD and organic layers, which may facilitate both electron and hole transfer after

photoexcitation. The transfer at the TMD/organic interface is determined by the energy level alignments of the TMD's CBM and VBM against the lowest unoccupied molecular orbital (LUMO) and the highest occupied molecular orbital (HOMO) of the organic molecule.[10, 25, 80] At the heterointerface, the electrons in a higher energy level may spontaneously migrate to a lower level, while the electron transfer in the opposite direction is forbidden (i.e., energetically unfavorable). Simultaneously, the hole transfer takes place from a layer possessing a lower energy level to the opposite layer, but not the other way around.

The photoinduced charge transfer at the type II interface may govern the optoelectronic properties of the TMD/organic structures and the performances of the hybrid junction devices. Huang and coworkers investigated the effects of photoinduced charge transfer process by functionalizing a MoS_2 flake with ZnPc, forming a staggered alignment as shown in Figure 8a.[137] They observed an electron transfer from ZnPc to MoS_2 and the hole transfer in the opposite direction. As the excitons in MoS_2 were dissociated at the interface, the MoS_2/ZnPc heterolayer exhibited a significant drop of PL intensity compared to the as-prepared, pristine MoS_2 flake. The exciton dissociation at the interface can also lead to a faster photoresponse. They studied the photoresponse by measuring the time needed for the increase of the electric current under light illumination. Figure 8b shows the ZnPc-functionalized MoS_2 exhibited three orders magnitude faster photoresponse than the pristine MoS_2 in Figure 8c.

It should be noted that while this review discusses the dark-state doping (section 3.2) and the photoinduced charge transfer separately to emphasize their differences, both mechanisms may take place simultaneously in a sample. For example, EY leads to a dark-state p-doping on monolayer WSe_2 due to its lower redox potential than the WSe_2 work function. The organic layer also facilitates photoinduced charge transfer at the TMD/organic interface, attributed to the type II energy level alignments.[34] Figure 8d demonstrates the work function transition of WSe_2 via EY functionalization measured by Kelvin probe force microscopy (KPFM). Due to the dark-state doping process, the EY-decorated WSe_2 samples with different layer numbers from 1L to 8L exhibit a lower work function than the pristine WSe_2 of corresponding layers. Additionally, as the type II alignment is developed at the WSe_2/EY interface, the excitons populated in the TMD layer may be easily dissociated at the interface. As a result, the hybrid junction generates a greater amount of photocurrent than the unmodified WSe_2 as shown in Figure 8e.

In contrast to the type II alignment, type I heterolayers may facilitate resonant energy transfer (RET) from a lager bandgap material to a smaller one.[98, 138] Park et al. showed that PTCDA forms a type I energy level alignment with monolayer MoS_2 on a sapphire substrate, allowing the RET from the organic layer to the TMD (Figure 9).[98] It is worth noting that other research groups studying the same MoS_2/PTCDA heterojunction deposited on a Si/SiO_2 substrate observed a type II band behavior, where interlayer charge transfer was dominant.[100, 139] The different energy level alignments with the same components may originate from the band renormalization in MoS_2 due to the different dielectric environments as discussed above. The sapphire and the silicon dioxide substrates have dielectric constants of approximately 11.5 and 3.8, respectively. With a stronger dielectric substrate (sapphire), the MoS_2 bandgap may be reduced to a greater extent via bandgap renormalization (see section 3.1, regarding the effect of dielectric screening on the energy band), thus developing a straddling gap between the TMD and PTCDA. Figure 9a shows that the LUMO of PTCDA is located slightly higher than the MoS_2 CBM by ~0.17 eV, while the HOMO is situated lower than the MoS_2 VBM by ~0.27 eV.[98] Contrary to the PL quenching due to the exciton dissociation and interlayer charge transfer by the type II alignment, the straddling alignment may lead to an enhancement of MoS_2 PL intensity via RET. In Figure 9b, the MoS_2/PTCDA hybrid has a higher PL intensity than the control (MoS_2) by a factor of two. The more detailed discussions on the charge/energy transfer mechanisms at the TMD/organic heterointerfaces are described elsewhere.[32, 111, 138, 140-142]

The design schemes for hybrid heterostructures also have been investigated to add a new degree of freedom for TMD/TMD or TMD/other 2D layers. The attached organic layers on TMD-based heterolayers govern the energy/charge transfer at the interface.[33, 90, 93, 142-146] Qiao et al. reported that pentacene molecules inserted between the $MoSe_2$/graphene oxide (GO) hybrid structure may behave as an energy funneling channel (Figure 9c).[93] The photo-excitation energy in the GO layer is successively transferred to pentacene and then to the $MoSe_2$ layer with the consecutive type I/type I alignment as illustrated in Figure 9d. This results in an increase of PL intensity in the hybrid structure, which is significantly higher than that of pristine $MoSe_2$ (Figure 9e). To confirm the behavior, they explored the PL enhancement under different excitation energies. In Figure 9f, the $MoSe_2$/1L pentacene hybrid junction exhibits a sudden jump in PL enhancement above the excitation energy of ~1.9 eV which corresponds to the HOMO-LUMO gap energy of pentacene. Additionally, the ternary $MoSe_2$/1L pentacene/GO shows another significant increase in PL intensity, where all three layers are

excited by photo-irradiation above ~2.5 eV. It is worth noting that the hybrid junction made of monolayer pentacene demonstrates a significantly greater PL increase than the hybrid layers with bulk (thick) pentacene layer. They attributed the difference in the PL enhancement to the distinct charge transfer processes. As illustrated in Figure 9g, the monolayer pentacene may have the face-on configuration, while the thick pentacene is stacked with upright packing (Figure 9h). The photoexcited charges in 1L pentacene may be immobile across the organic layer due to the lack of π–π^* stacking. Therefore, the electrons can be readily transferred to the $MoSe_2$ layer. In comparison, the charges in the bulk pentacene layer may be delocalized along the lateral direction rather than transported to the heterolayer as shown in Figure 9h. The results suggest that organic layers may regulate the interlayer energy transfer, based on the stacked topology and the energy level alignments in multilayered hybrid structures. Similar energy transfer mechanisms were reported by Cheng and coworkers.[142] They deposited organic dyes on substrate/MoS_2/hBN to enhance the photoresponsivity via RET processes. The MoS_2-based hybrid photodetector shows about 90 % enhancement in photoresponsivity compared to the detector without an organic layer.

Molecular systems may also affect the behavior of IXs in TMD-based heterojunctions depending on their energy level alignments.[33] For exampl1e, our group constructed the consecutive type II alignments of tetracyanoquinodimethane (TCNQ) functionalized WSe_2/MoS_2, where photoinduced electrons in the WSe_2 CBM and the MoS_2 CBM are transferred to the TCNQ LUMO as illustrated in Figure 10a. Here, the IXs formed in the TMD/TMD heterostructure were dissociated at the TMD/TMD/organic interface, resulting in a drastic quenching of interlayer emission at ~772 nm (Figure 10b). On the other hand, an EY-deposited WSe_2/MoS_2 hybrid junction forming the successive type II and type I interfaces in Figure 10c demonstrated well-preserved interlayer emission (Figure 10d). Due to the straddling alignment at the TMD/organic interface, the interlayer charge transfer will be prohibited from MoS_2 to the organic layer. The results suggest that the molecular system may play a critical role in tuning the optoelectronic characteristics of TMD/TMD heterostructures.

Taking a step further, it has been shown that the intercalated organic layers between TMD/TMD heterobilayers may regulate interlayer charge transfer mechanisms and govern the dielectric screening on IXs and.[90] Figures 11a illustrates that an organic layer, 1,3-bis(3,5-dipyrid-3-ylphenyl)-benzene or B3PyPB, forms type I alignments with both MoS_2 and WSe_2. Due to the large energy barrier by B3PyPB, the charges in MoS_2 and WSe_2 flakes may be

transferred (i.e., electrons from WSe_2 to MoS_2 and holes from MoS_2 to WSe_2 as indicated by blue arrows) by quantum decaying processes similar to the charge tunneling in pristine MoS_2/WSe_2.[147] In Figure 11b, the B3PyPB-inserted hybrid structure exhibits its interlayer emission peak at ~1.60 eV, which is significantly blueshifted from that (~1.55 eV) of MoS_2/WSe_2 heterobilayers. The intercalated organic layer may increase the separation distance between the charges in an IX and reduce the dielectric screening on the quasi-particle, thus resulting in a reduction of IX binding energy. Such a modulation on IX ultimately leads to the increased emission energy (see equation 1). In contrast, the embedded EY layer between WSe_2 and MoS_2 flakes develops consecutive type II alignments as shown in Figure 11c, where electron transfer between the TMDs may be facilitated by the organic layer. In addition to the energetically favorable electron transfer, MoS_2/EY/WSe_2 may have an improved hole transfer compared to the B3PyPB-embedded heterostructure. As shown in Figures 11a and 11c, the barrier height between the EY HOMO and the MoS_2 VBM for the hole transfer is smaller than that between the B3PyPB HOMO and MoS_2 VBM. Therefore, a greater amount of photoinduced electrons (holes) may be accumulated in MoS_2 (WSe_2) of the EY-embedded hybrid compared to the B3PyPB-inserted structure. As a result, there will be an increased IX population in the EY-based hybrid and a stronger IX emission is observed (Figure 11d). This observation is also consistent with the increased IX energy in the EY-intercalated heterolayers (by ~25 meV) compared with that of MoS_2/B3PyPB/WSe_2, as reported in our recent publication.[90] This is because the IXs form out-of-plane dipoles and the more IXs may experience stronger repulsive interactions, leading to a spectral shift. More detailed analysis on the population-dependent behavior of IXs may be found elsewhere.[148]

3.4. Defects and Imperfection

Intrinsic defects in TMDs present two opposite effects; they may be either detrimental to the unique (opto)electronic properties of TMDs or engineered to introduce novel functionalities. The methods utilizing the defects, for example, as binding sites to attach functional molecules have been discussed elsewhere.[32, 42, 149] Here, we focus on the drawbacks of defects and how the structural disorder can be cured by using molecular systems. Electronic and optoelectronic transport properties of 2D TMDs are limited by the defects because they behave as charge traps and scattering poles. The defects distributed in TMDs may develop unwanted local potential and alter carrier densities, resulting in uncontrollable carrier behaviors. According to McDonnell et al., the TMD transistors prepared with Au metal contacts and silicon dioxide back gate exhibit distinct n-type and p-type behaviors with defect-free and defect-rich MoS_2

flakes, respectively.[150] This observation indicates that the work function of MoS_2 could be altered based on the defect levels. Thus, it may be necessary to regulate the defect states in the 2D semiconductors.

Covalent chemistry has been widely adopted to control the extent of defects, which may be exploited to improve device characteristics. Here, the chemistry often indicates a covalent reaction between thiolated molecules and sulfur vacancies in TMDs.[25, 40, 151] Yu et al. reported that the carrier mobility of a MoS_2 transistor could be significantly improved by attaching MPS molecules on the MoS_2 surface.[92] The molecules with thiol groups will heal the sulfur vacancy (SV) defects via a chemical reaction: $HS(CH_2)_3Si(CHO_3)_3$ + SV-MoS_2 = $(CH_2)_3Si(CHO_3)_3$-MoS_2. They observed that the mobility improved significantly from ~127 $cm^2V^{-1}S^{-1}$ with as-exfoliated MoS_2 to ~410 $cm^2V^{-1}S^{-1}$ with the MPS-functionalized transistor. Sim and coworkers utilized similar defect-healing strategies, functionalizing MoS_2 with mercaptoethylamine (MEA) and FDT (Figure 12a) to regulate the carrier densities in MoS_2.[39] Given the electron-rich nature of MoS_2, the n-doping on MoS_2 with MEA functionalization reduced excitonic PL emission (Figure 12b), because the doping increased the electron population in MoS_2. In contrast, FDT withdrew the excessive electrons from MoS_2, resulting in the enhanced PL intensity as shown in Figure 12c. Other combinations of TMDs and organic layers may be adopted for organic-based defect engineering and related applications which are listed in Table 1.

4. Optoelectronic and Energy Applications

A broad range of optoelectronic and energy applications with organic-integrated TMD systems have been demonstrated to exploit the distinct benefits of the hybrid materials. In particular, molecular systems may enhance the carrier transport and the PL yield of TMDs and control the carrier type and density as well as transfer pathways in the ultrathin materials. The organic layers can provide stable and reliable environments for the TMD-based devices, functioning as dielectric layers and substrates for minimizing trapped charges and reducing unwanted phonon scattering. The organic layers in the hybrid structures may also behave as charge transport or light-absorbing layers, thus providing additional functionalities. Furthermore, TMDs and molecular systems can complement each other to develop high-performance energy devices. For example, TMDs may offer high ion capacity for the electrochemical applications, while they may not provide enough openings (i.e., pores) to allow a fast ion diffusion. Such a limitation may be overcome by integrating TMDs with pore-rich MOFs that present ion

diffusion paths. In this section, we overview the recent advances in optoelectronics and energy applications utilizing the organic-integrated TMD systems. Tables 1 and 2 summarize the examples of the optoelectronics based on binary and ternary TMD-organic hybrids, respectively. Similarly, Table 3 introduces energy applications based on the organic/TMD composites. The purposes of the hybrid structures and their working mechanisms to achieve the goals are also included.

4.1. Phototransistors

Phototransistors use photoinduced charges as information carriers, where the number of charges in the material can be modulated by light illumination, similar to the gate switching mechanisms in electrically driven transistors. TMD monolayers are excellent candidate materials for photo-switching applications due to their sizable direct bandgaps and high carrier mobility.; They show excellent switching behaviors with a high on-off ratio upon photoirradiation. However, TMD-based phototransistors may have an unwanted photoconductance; that is, they do not return to the off-state when the light is removed. This may originate from the charge trapping at the interface of substrate/TMD and inherent trap states in the ultrathin materials.[137] The trapped carriers may delay the response time. To overcome the issues, molecular systems that build type II alignments with TMDs have been introduced. The photoexcited charges in excitons can be rapidly dissociated with the built-in potential at the type II interface, facilitating a fast photoresponse.[152-156] The TMD-organic hybrids can generate a greater photoresponse than pristine TMDs, because the charges in the interface may be spontaneously transferred to the opposite layers and contribute to electrical currents. Moreover, a set of organic systems can be selected for absorbing a wide range of light wavelengths, which may enable a broadband operation of TMD-organic phototransistors.

In Figure 13a, Pak et al. showed that p-type copper phthalocyanine (CuPc) and n-type MoS_2 formed a type II p-n heterojunction which outperforms the phototransistor made of pristine MoS_2.[155] The performance metrics they used included photosensitivity [S_P = photocurrent (I_p) / dark current (I_d)], photoresponsivity [$R_P = (I_p-I_d)$ / radiation power (P_r)], photo-detectivity (D_P), and external quantum efficiency (EQE). The photodetectivity was estimated with a formula: $D_P = (R_P*A^{1/2})/(2q*I_d)^{1/2}$, where A is the illuminated area, and q is the electrical charge (1.6×10^{-19} C). The EQE was defined as $(I_p/q)/(P_r/hv)$, where hv is the irradiated photon energy. CuPc molecules were thermally evaporated on MoS_2, inducing a p-doping on the MoS_2 channel

(Figure 13b). As the thickness of the stacked CuPc layer increases to 10 nm, the threshold voltage to turn on the device gradually transitions from ~0 V to ~12 V due to the p-doping effects. Figure 13c shows that both photoresponsivity and photodetectivity of the MoS_2 phototransistor increased by ten-fold after the molecular functionalization. Additionally, MoS_2/CuPc demonstrated an EQE of ~12 % which is more than twice that of the pristine sample at 400 nm. The results indicate that the TMD/organic hybrid performs significantly better than the pristine TMDs in the visible spectrum.

Molecular systems can lead to not only an enhanced quantum efficiency, but also a faster photoresponse in TMD phototransistors.[137, 157] According to Huang and coworkers, a ZnPc-coated MoS_2 phototransistor formed a type II heterojunction and exhibited significantly faster photoresponse than the MoS_2 device.[137] The ZnPc layer was deposited by dipping the MoS_2 on a substrate in a solution containing ZnPc. Figure 13d shows the measured photoresponse time which decreases with increasing the duration of immersion. Here, the purple dots indicate the required time to turn on the phototransistor, whereas the black symbols represent the response time to switch off the device. The fully functionalized MoS_2 had three orders of magnitude faster photoresponse than the pristine sample. It is evident that the organic layer forming a staggered energy level alignment with MoS_2 can reduce the trapped charges and facilitate photoinduced charge transfer.

In addition to the studies of organic-attached individual TMD phototransistors, the strategies were extended to heterostructures (e.g., MoS_2/graphene).[143] Zhou et al. introduced a MoS_2/ZnPc/graphene hybrid heterostructure by first decorating MoS_2 with the immersion method, and then, stamping graphene onto the MoS_2/ZnPc heterolayers.[143] ZnPc molecules may behave as p-dopants reducing the trapped charges and develop a staggered band alignment with the MoS_2 layer. Thus, photogenerated electrons in MoS_2 were dissociated at the TMD/organic interface and transferred to graphene which were collected at the gold electrodes.[158] They reported in their original work that the organic-embedded heterostructure showed a substantially higher photosensitivity than the MoS_2/graphene device.

Ko et al. reported organic-decorated flexible graphene/MoS_2/graphene heterostructures, where the top and the bottom graphene layers were doped with bis (trifluoromethanesulfonyl)-amide (TFSA, p-dopant) and triethylene tetramine (TETA, n-dopant), respectively.[159] As illustrated in Figure 13e, the fermi level of TFSA-graphene is located below the Dirac point, while that

of TETA-graphene is higher than the Dirac energy. This allows a consecutive electron transfer from TETA-graphene to TFSA-graphene under forward bias, while holes move in the opposite way. As a result, stable charge transport was observed across the MoS_2 channel, and the device shows a high photoresponsivity under forward bias in Figure 13f. Additionally, they reported that the response time of the ternary hybrids for turning on/off the device under light illumination was extremely fast, estimated to be 50 μs. This response time is orders of magnitude faster than the response of binary MoS_2/ZnPc device in Figure 13d. Moreover, they explored the organic-functionalized TMD-based heterostructures for flexible phototransistors. To examine the long-term stability of the bendable device, they tested the retention of photoresponsivity under cyclic loads. After 2,000 bending cycles, the organic-integrated flexible phototransistor shows up to 87% of the initial photoresponsivity.

4.2. Light Emitting Diodes (LED)

LED have been studied extensively as one of the most fundamental elements in display technology over the past decades.[160] LED consist of several components, including light emitting channels, electron (hole) injection layers, and transparent electrodes. The light emitting and charge injecting layers can be prepared from various organic/inorganic materials. TMD-based inorganic-organic LED (IOLED) have garnered great attention to overcome the disadvantages of conventional organic LED (OLED), including high energy consumption, instability in the ambient environment, and poor charge injection efficiency due to the large energy barrier between organic channels and electrodes.[161, 162] Moreover, TMDs may offer a higher charge mobility than organic semiconducting materials.[29] To use TMDs as charge injecting layers, researchers have explored CVD-grown TMDs with a high crystallinity and solvent processed TMDs (via solvothermal synthesis or liquid exfoliation).[161, 163, 164] While the high-crystalline ultrathin TMDs are suitable to study the fundamental characteristics, the solution processed samples may be useful for large-scale commercial applications given the scalability.

Guo and coworkers reported that MoS_2-based IOLED could be useful for blue-fluorescent flexible device applications.[162] Their device was prepared by sequential chemical deposition of multiple layers, including MoS_2 and various organic layers, on a flexible polyethylene terephthalate (PET)/indium tin oxide (ITO) substrate. As shown in Figure 14a, the MoS_2 CBM near the work function of ITO may receive electrons from the electrode (cathode) and the small barrier height between MoS_2 and the adjacent organic layer allows a smooth electron transfer

to the light emitting layer. Simultaneously, holes can be transferred from the anode to MoO_3. The injected electrons and holes in the LED may radiatively recombine and emit the electroluminescence in a blue color range as shown in Figure 14b. The image reveals that the diode can operate under a severe bending (e.g., with an angle of 150°) due to the all-bendable features of MoS_2 and organic layers. They reported that the device exhibited nearly uniform luminescence for 500 bending cycles. Here, the EQE of MoS_2-integraed IOLED was estimated to be approximately 7 % at the luminance of ~9100 cd/m^2, which is about two times higher than the LED without the MoS_2 layer. They attributed the enhanced performance to the light extraction effect of the MoS_2 layer, where the MoS_2 flakes on the flexible PET/ITO substrate forms nano-arrays as shown in Figure 14c. The arrays with a height of ~30 nm as shown in Figure 14d may reduce the reflectivity of the emission surface by suppressing the internal reflection of electroluminescence, resulting in the high luminance.

TMDs can also be exploited as a hole injection layer (HIL) in IOLED. Conventional HILs such as poly(3,4-ethylenedioxythiophene):poly(styrenesulfonate) (PEDOT:PSS) have limitations including acidity and hygroscopicity of the organic layer that degrade the contact electrode.[164, 165] TMD-based HIL approach has been explored to overcome the limitations. Park and coworkers utilized a hetero-composite made of chemically exfoliated MoS_2 and GO synthesized by Hummer's method as a HIL component.[164, 166] They hypothesized that MoS_2 may reduce the hole injection energy barrier and that GO can suppress the unwanted recombination of the holes and electrons in MoS_2, thus enhancing the conductivity of the device.[164] They reported that an IOLED prepared with a 3:2 mass of MoS_2 and GO showed the highest power efficiency and the lowest turn-on voltage to yield a luminance of 10 cd/m^2.

4.3. Photovoltaics

Organic-integrated TMDs are promising candidate materials for photovoltaic applications thanks to their semitransparency and strong photo-absorbance as well as the direct bandgaps and high mobility.[10, 80, 167-170] Similar to IOLED, photovoltaic cells generally consist of active channels, electron and hole extraction/transport layers, and contact electrodes. TMD-organic hybrids may serve as the active channels or the charge transport layers. In 2013, Fontana et al. reported multilayered MoS_2 as a light absorbing channel for a photovoltaic device.[171] They fabricated the photovoltaic cell by interfacing the TMD channel with asymmetric electrodes made of Pd and Au. Under laser irradiation, the photogenerated charges in the semiconducting channel were dissociated at the contact interface with the built-in potential, leading to the

photovoltaic currents. They estimated the photovoltaic conversion efficiency (PCE) of the cell to be approximately 2 %, where the PCE was evaluated by comparing the maximum electrical power of the device to the power of the incident laser.

Kesavan and coworkers introduced a photovoltaic system made of poly[[4,8-bis[(2-ethylhexyl)oxy]benzo[1,2-b:4,5-b']dithiophene-2,6-diyl][3-fluoro-2-[(2-ethylhexyl)carbonyl] thieno[3,4-b]thiophenediyl]] (PTB7), bis-[6,6]-Phenyl C_{71}butyric acid methyl ester ($PC_{71}BM$), and MoS_2 nanosheets as illustrated in Figure 15a.[172] The ternary composite including 30 % loading of MoS_2 by mass demonstrated a PCE of over 7 % (Figure 15b), which is approximately 17 % improved from the sample without TMDs (marked as neat). They explained the enhanced efficiency with several factors. As shown in Figure 15c, the ternary blend (device-B) exhibits (i) a greater absorbance than the device-A made of the organic layers alone. With the staggered energy alignments between the active materials (Figure 15a), the composite may facilitate (ii) energetically favorable charge transfer from PTB7 to the MoS_2 layer. Moreover, MoS_2 structure may play a role in (iii) increasing the carrier mobility, due to a higher electron mobility of TMDs compared to that of organic semiconductors. Similarly, Ahmad et al. reported that the inorganic-organic blends made of MoS_2, $PC_{71}BM$, and poly(3-hexylthiophene-2,5-diyl) (P3HT) exhibit over 30% enhancement in PCE relative to the organic blend P3HT/$PC_{71}BM$ due to the synergistic effects between MoS_2 and organic layers.[173]

TMD layers may also be incorporated as the charge extraction/transport layers in organic photovoltaic cells. Lin et al. constructed organic/inorganic heterostructures by blending PBDB-T-2F, Y6, and $PC_{71}BM$ with a hole transport layer (HTL) made of chemically exfoliated WS_2. Here, PBDB-T-2F represents poly[[4,8-bis[5-(2-ethylhexyl)-4-fluoro-2-thienyl]benzo[1,2-b:4,5-b′]dithiophene-2,6-diyl]-2,5-thiophenediyl[5,7-bis(2-ethylhexyl)-4,8-dioxo-4H,8H-benzo[1,2-c:4,5-c′]dithiophene-1,3-diyl]-2,5-thiophenediyl] and Y6 indicates thieno-thienopyrrolo-thienothienoindole.[174] They reported that the heterojunction solar cell demonstrated greater photovoltaic performances than the conventional device utilizing PEDOT:PSS as a HTL. Figure 15d shows the current-voltage responses of the binary PBDB-T-2F:Y6 and the ternary PBDB-T-2F:Y6:$PC_{71}BM$ layers with different HTLs. The device with the ternary composite and a WS_2 HTL demonstrates the highest short-circuit current density of ~26 mA/cm^2 (red line in the figure). This suggests that the TMD HTL may be adopted to replace the conventional PEDOT:PSS HTLs which show several drawbacks such as hygroscopicity and degrading contact electrodes. They also estimated that the WS_2-layer-

attached PBDB-T-2F:Y6:PC71BM exhibits the highest PCE of ~17 %. They attributed the high PCE to the lower work function (-5.5 eV) of WS_2 than that (-4.8 eV) of PEDOT:PSS, allowing a greater extent of hole extraction and a minimal electron-hole recombination. They estimated the recombination rate $k_{rec} = 1/(\lambda+1)n\tau$, where τ and n represent the carrier lifetime and density monitored by transient photovoltage measurements, respectively (Figures 15e and 15f). λ is the recombination order determined by estimating the linear relationship between τ and n. Their analysis suggested that the WS_2 incorporated device shows a higher λ (1.76) than the others ($\lambda_{PEDOT:PSS}$ = 1.73 and λ_{MoS2} = 1.67) . The WS_2-layer-attached organic photovoltaics presents greater values of n, τ, and λ than the others, leading to the suppressed recombination. As a result, the WS_2-organic photovoltaics demonstrates the high current density and the outstanding PCE.

4.4. Optical Memory

The industry of memory and logic devices has exponentially grown to meet the demands for fast and reliable writing/reading, and energy-efficient operation of extensive data storage. While the electrically driven memories have dominated the market share due to their energy-efficient switching and high-density data storage, the conventional strategy for implementing more electric circuits in a given footprint encounters several challenges.[175] These include almost saturated technologies to reduce gate length below a few nanometers and quantum tunneling effects through extremely thin gate dielectric.[176, 177] To address the limitations, multi-level responsive logic devices manipulated by chemical reaction or photo-irradiation along with electrical switching have attracted significant attention. Such devices may enable additional functionalities for writing and reading operation.[85, 178-181] In 2019, Qiu and coworkers reported that WSe_2 memory functionalized with photochromic diarylethene (DAE) may be optically switched under ultraviolet (UV) and visible (Vis) irradiation which was used to generate four distinct current levels based on the duration of illumination.[178] Here, the optical memory can write and read the optical signal simultaneously. Figure 16a illustrates the modulation of DAE energy levels under UV and Vis light illumination against WSe_2 CBM. DAE can be switched between open and closed isomers by irradiating Vis and UV irradiation, respectively. The conformational changes regulate the interlayer charge trapping at the WSe_2/organic interface, promoting the trap-induced writing and erasing of memories. Due to the trapped electrons in closed DAE under UV, the WSe_2/DAE device exhibits a reduction of drain current (from blue to purple in Figure 16b). The current returns to the initial level (green) after the Vis irradiation. Figure 16c demonstrates the multi-level currents of the device

governed by different illumination times, where the level 1 current is obtained upon UV irradiation of 2 sec, and the levels 2, 3, and 4 are achieved with 4, 8, and 16 sec irradiations, respectively. The same group recently advanced the optical memory system further, showing 128 distinct current levels with a similar WSe2/DAE hybrid structure by controlling both hole and electron trapping behaviors.[85]

4.5. Supercapacitors

TMDs present many attractive features for energy storage applications.[27] These include layered structures with high ion capacity and diverse morphologies depending on synthesis methods. For example, Figure 17a presents chemically synthesized MoS_2 via a solvothermal method, having flower-like nanostructures with dense surface area. This allows for a great extent of ion accumulation at the surface.[182] It is worth noting that the flower-like structures are also beneficial in exposing their edges to the surroundings. It was reported that the edges of TMDs behave as active sites for efficient charge transport.[183] As the heterogeneous charge transfer occurs at the TMD edges, the nano-patterned structures may increase not only the surface area, but also the catalytic effects.[184-186] Among various types of energy storage devices, supercapacitors may be one of the ideal platforms to fully utilize such excellent characteristics. TMD-based supercapacitors offer high energy and power densities with remarkable durability.[187, 188] The devices are expected to overcome the limitations of conventional electrochemical capacitors with low energy densities and batteries with relatively poor cyclability and low power densities.

Despite the promising features, TMDs have several limitations to be used for the electrode materials. TMDs are inherently semiconductors, thus they may not be ideal for conductive charge collection.[126] In addition, the densely packed TMDs may also lack porosity, which limits ion diffusion across the electrodes and charging/discharging process during the electrochemical storage.[189] These limitations may be overcome by integrating TMDs with organic materials, including conjugated polymers, MOFs, and carbonaceous composites (e.g., carbon nanotubes and GO).[126, 189-199] The hybrid approach can offer distinct advantages for energy storage applications. Table 3 summarizes the recent progress in energy applications made of binary or ternary hybrids, highlighting the preparation methods, the electrode morphologies, and the device performances.

Conductive polymers such as polyaniline (PANI), polypyrrole (PPy), and PEDOT can be

excellent supporting materials for TMDs to increase the electrical conductivity, reduce the production cost, and enhance the flexibility of TMD-based supercapacitor electrodes.[200, 201] Kim et al. introduced PANI/MoS_2 nanocomposites via a self-stabilized polymerization process.[200] When they estimated the electrical conductivities of MoS_2, PANI, and PANI/MoS_2 electrodes, the nanocomposite demonstrated an electrical conductivity of ~30 S/cm. This conductivity is five orders of magnitude higher than that of MoS_2. They also estimated the specific capacitance of each supercapacitor electrode with galvanostatic charging and discharging (GCD) process as shown in Figure 17b. The PANI/MoS_2 electrode demonstrates a galvanometric capacitance of ~400 F/g with an energy density of ~4 Wh/kg and a power density of ~2,000 W/kg. This performance is far greater than those of pristine MoS_2 and pure PANI samples. They reported that the composite shows a higher capacitance retention of ~84 % than that (64 %) of PANI, which is attributed to the outstanding electrochemical stability of MoS_2. For the same combination of the materials, the electrochemical performance of supercapacitor electrodes may be enhanced by engineering the topology of the composites. Zhang et al. prepared hollow microspheres made of MoS_2/PANI as illustrated in Figure 17c.[191] The MoS_2 spheres provide ion channels and large surface areas, while the PANI layer increases the electric conductivity of the composite. Figure 17d shows the performance curve of energy versus power densities. The topologically engineered MoS_2/PANI composite exhibits a high energy density of about 30 Wh/kg at a power density of ~320 W/kg.

Combining TMDs with MOFs may exploit synergetic effects for energy storage.[190, 202-205] MOFs are compounds of coordinated organic ligands chelating metal ions and thus form highly ordered three-dimensional structures. Govindan and coworkers introduced such an approach with MoS_2 synthesized with CeO_2/C, a type of MOFs.[205] Here, MoS_2 nanosheets provide active sites to store charges while the porous MOF allows for fast ion diffusion, resulting in a high energy density of approximately 35 Wh/kg at a power density of ~667 W/kg. The MoS_2-CeO_2/C hybrids form hierarchical structures (Figure 17e) which are beneficial in enhancing the structural integrity and allowing stable structural expansion and contraction during the charge and discharge processes. In their report, the electrode demonstrated pairs of redox peaks at about 0.5 and 0.3 V from the cyclic voltammetry (CV) measurements. This indicates that the charges are stored based on both surface- and diffusion-controlled processes. Figure 17f presents the contributions of the surface and diffusion processes, where the diffusion-controlled contribution is higher than that of the surface capacitance for most of scan rates. This may be attributed to the high ion diffusivity offered by MOF and reactivity by MoS_2 layers of the

electrode material.

With similar strategies, multi-components electrodes have been explored by many groups.[192-196, 206, 207] For example, Zhang and coworkers introduced multi-walled carbon nanotubes (MWCNTs)/PANI/MoS_2 nanocomposites as illustrated in Figure 18a.[192] The nanotubes offering conductive networks behave as a foundation for the polymerization of aniline and solvothermal growth of MoS_2, while preventing self-aggregation of each constituent material. Figure 18b shows the scanning electron microscope (SEM) image of the composite. The PANI-coated nanotube has an approximately 90 nm diameter, with the petal-like MoS_2 nanostructures attached, like flowers on a stem. The electrode made of the composites exhibits a high specific capacitance of over 540 F/g at 0.5 A/g with a strong cyclic behavior, showing ~70 % of capacitance retention after 3,000 cycles. Naz et al. demonstrated another ternary composite made of MoS_2, GO, and WO_3 (Figure 18c).[208] The MoS_2 has high ion capacity, the GO offers excellent conductivity, and the hexagonal WO_3 provides intracrystalline tunnels for efficient ion transport and multiple oxidation states for pseudocapacitive energy storage.[103, 182] The ternary MoS_2/WO_3/GO demonstrated an impressive specific capacitance of > 800 F/g at 1 A/g, which is over two times higher than that of MoS_2/GO (or WO_3/GO). In a similar study, Chen and coworkers introduced a flexible supercapacitor exploiting the bendable properties of a GO/MoS_2/PEDOT composite.[195] Figure 18d shows the scheme of fabricating the flexible electrode composite. They claimed that the composite is hierarchically piled up by π–π^* stacking, electrostatic interaction between GO and PEDOT, and vdW interaction at the GO/MoS_2 interface. They explored the influence of mechanical deformation on the performance of the flexible supercapacitor (Figure 18e). Regardless of bending, the device showed a uniform current-voltage response with an areal capacitance of ~240 mF/cm^2. It should be noted that the abovementioned studies employed a hierarchical synthesis of the composites to exploit the distinct benefits of the constituent materials.

4.6. Catalysts for Renewable Energy

TMDs and TMD-organic hybrids have been adopted for various catalysis applications, including hydrogen evolution reaction (HER), photo-driven HER (PHER), and pollution reduction.[189, 209-212] The catalytic degradation of hazardous materials using TMD hybrids has been discussed previously.[211, 213] Rather, this article focuses on the energy applications using the catalytic properties of the TMD-based materials. Generating electricity from HER and PHER in water electrolysis received global interests to realize sustainable, renewable, clean

energy sources at affordable cost on a large scale.[214] Such methods require low-cost and reliable catalysts to achieve high current densities at low electric potential. Noble metals such as Pt have been explored for excellent catalytic performances, yet the high price of the material significantly limits the commercial usage.[215] The approach of developing hybrid TMD-organic composites may present a breakthrough to achieve low-cost catalysts without compromising the high current densities.[189, 209, 216-221] MoS_2/PPy composites introduced by Wang et al. exhibited a HER performance comparable to that of the Pt electrode (Figure 19a).[222] For the composite, the molybdenum sulfide structure was synthesized with excessive sulfur. Figure 19b shows the polarization curves of the composite electrodes. A Tafel slope (TS) of MoS_x/PPy electrode (marked 'd') was estimated to be approximately 30 mV/dec, which is comparable to that of the ideal Pt electrode (marked 'e'). Here, TS determines the rate of an electrochemical reaction to the overpotential with an equation: , where represents the overpotential. I and I_0 indicate the measured and exchange current densities, respectively. The exchange current density defines the current at the zero overpotential under the absence of net electrolysis. They attributed the excellent performance to the high conductivity with PPy and abundant catalytic sites in MoS_x for efficient HER.

In addition to the conductive polymers, integrating other kinds of functional materials such as carbonaceous composites with TMD layers could be advantageous for developing high-performance HER devices. Lee et al. demonstrated that ball-shaped MoS_2 nanostructures (Figure 19c) may be transformed into petal-decorated nanosheets (Figure 19d) by adding GO precursors during the solvothermal synthesis.[47] Figure 19d shows that small MoS_2 flakes are attached to large GO sheets. As the well-distributed MoS_2 flakes are exposed to the surrounding, the composite material may bear more MoS_2 edges (i.e., catalytically active sites) than the pure MoS_2 electrode.

Besides the TMD hybrids prepared with conductive polymers and carbonaceous materials, the TMD-MOF composites also show promising HER behaviors. Tong et al. constructed electrodes from MoS_2 and zeolitic imidazolate framework (ZIF), a type of MOFs, forming highly porous networks.[223] As shown in Figure 19e, the ZIF exhibits a rhombic dodecahedron structure and presents a large surface area. The small sheets on the rhombic structure are MoS_2 flakes from solvothermal synthesis. They reported that the MOF-MoS_2 composite electrode demonstrated a good durability that is comparable to that of the platinum electrode (Figure 19f). They attributed the excellent stability to the mesoporous MOF structures allowing a fast

ion diffusion without damaging the electrode. Overall, the strategies for TMD hybrids may be beneficial for enhancing the catalytic performance as well as improving the durability.

The TMD hybrid catalysts also have been adopted to generate hydrogen by converting external photon energy to the electrochemical energy.[48, 210, 224-228] The TMD layers in the hybrid materials offer sizable bandgaps with strong light-matter interaction suitable for the photo-catalytic effects. Additionally, the TMD-based composites provide high specific areas and fast charge transfer at the active sites.[210, 225, 229-231] These characteristics make TMD hybrids strong candidates for high-performance PHER devices. Ma and coworkers explored photocatalysts made of MoS_2 and $Cu_{0.9}Co_{2.1}S_4$ (a type of MOFs), where the MOF behaves as a template to grow edge-rich MoS_2 nanoflowers via solvothermal method.[229] The dense flower-like structures shown in Figure 20a expose the active edges with high surface area. Note that the inset shows the MOF structure without MoS_2 layers. Figure 20b presents the photocatalytic performances of the composites with various chelated metals, including Co, Zn, Ni, and Cu, in MOFs. Among the composites, bimetallic ($Cu_{0.9}/Co_{2.1}$) MOF/MoS_2 shows the best performance at a photoinduced hydrogen production rate of ~40 mM/hour·g in aqueous solution with ~3 % of quantum efficiency. They claimed that the homogeneously doped metal ions (Cu^{2+}) with a 1:3 ratio to the host Co ions could provide additional energy levels to promote the photoinduced charge transfer, facilitating the hydrogen evolution. Choi et al. introduced nanocomposite electrodes made of ternary MoS_2/CdS/nickel phosphide (Ni_2P)-derived MOFs to enhance the quantum efficiency of PHER.[225] Figure 20c illustrates the schematic of the composite synthesis, where the CdS QDs are decorated with MoS_2 flakes and Ni_2P-MOFs. They reported that the composite electrode generates an excellent photocatalytic hydrogen evolution rate (~73 mM/hour·g) with a quantum efficiency of ~24 %, thanks to the energetically favorable charge transfer as illustrated in Figure 20d. With the high PHER performances, the TMD hybrids may be utilized for sustainable and renewable energy.

5. Conclusions and Outlook

In this review, we have highlighted the extraordinary (opto)electronic and electrochemical properties of TMD/organic and multi-component hybrids based on the synergistic effects between the hetero materials. We focused on the interactions between molecular systems and TMDs, including interlayer charge transfer (dark-state and photoinduced processes), band-alignment-dependent behaviors, electronic screening effects, dipolar interactions, and defect-assisted chemistry. The discussion elucidates the working mechanisms and provide insights on

how the exceptional properties of the hybrids can be exploited. We also have introduced recent advances in diverse engineering applications including optoelectronic devices (LEDs, phototransistors, photovoltaics, and optical memories) and energy applications such as supercapacitors and catalysts. The studies not only demonstrated excellent performances of the devices but also presented the strategies for exploiting properties vital to applications. Given the importance of the hybrid structures in both fundamental science and promising applications, this research field will advance rapidly and make transformative impacts in material science. Below we present perspectives and outlook on opportunities and challenges.

5.1. Optoelectronic Properties of Multilayered Hybrid Structures

Exciton dynamics in monolayer TMDs and TMD/TMD heterostructures have been studied extensively to understand many-body phenomena in charge-to-charge interactions and light-matter interactions.[232-235] Excitons in 2D materials can dominate the absorption and emission characteristics.[236, 237] The light-matter interaction may be highly affected by charge densities, dielectric environments, and external stimuli such as electric potential and optical carrier injection.[91, 148, 238, 239] Despite the importance, the study of TMD/organic hybrid materials has been limited.[138] For example, the dynamic behaviors of IXs in TMD/TMD heterostructures are still not well understood, including the lifetime, diffusion characteristics, and relaxation under external electrical fields. The organic-embedded multi-components hybrids may be used as testbeds to investigate the detailed IX dynamics. As discussed in section 3, the charge densities of individual TMDs and TMD/TMD heterostructures can be modulated in nondestructive, facile ways by the organic-layer-dependent doping processes. Besides the doping, ferroelectric organic compounds such as tetrathiafulvalene, pyromellitic diimide, haloimidazole, and poly(vinylidene fluoride-trifluoroethylene)[152, 198, 218] may be adopted to provide a local polarization of electric field, which can alter the IX energy. As the organic layers may build distinct energy level alignments with TMDs, the exciton dynamics may also be studied under different interlayer charge transfer processes such as tunneling of charges and type II junction-supported transport.[33, 90, 240] The approaches that control exciton populations may enable comprehensive studies on IX-IX correlation.[148]

In addition, the optoelectronic properties of TMD/organic hybrids may be dependent on the nature of the molecular system that responds to external stimuli. As introduced in subsection 4.1, photochromic molecules can change their configurations and energy levels under different irradiation energies.[178, 241] Similarly, other environmentally sensitive molecules such as electro-

[242] and chemo-[86], and magneto-responsive[243] molecules may provide additional functionalities and multi-responsive features in TMD/organic-based devices.

5.2. Challenges in Practical Applications

Thanks to the tremendous efforts on scalable production of large-area TMDs, the synthesis of fabricating millimeter- and centimeter-scale 2D TMD layers is now possible.[244-246] However, the structures may still have significant amounts of grain boundaries and defects.[247, 248] The defective 2D layers may not have homogeneous (opto)electronic properties. Moreover, the polycrystalline structures of synthesized TMDs may hinder the uniform deposition of organic layers that are required to tune their properties for applications. Thus, it is necessary to develop reliable processes to integrate TMDs and organic molecules uniformly at a large-scale. Another challenge on the ultrathin TMD hybrids originates from the stability of the organic layers in high temperature or harsh chemical environments. The molecular systems may not be compatible with the conventional microfabrication techniques such as thermal evaporation at high temperatures, strong solvents, and electron bombardment by e-beam evaporators.[25] To overcome the limitations, it is required to passivate the TMD hybrids without deteriorating the quality of the organic layers.

Better fabrication strategies for TMD hybrids should benefit 2D optoelectronics as well as energy storage applications. In subsection 4.2, we discussed that the energy storage device performance depends on both the components and the topology of the material. Even though numerous studies provided valuable information for designing composite electrodes made of TMDs, MOFs, and carbonaceous composites,[249-251] it may be nearly impossible to explore all the combinations and optimize the topology and amount of each constituent material. Thus, we now may shift our attention to another resource to develop efficient methodologies that could help us understand the correlation between the performance and the electrode structures. Here, the metaheuristic machine-learning-based approaches may be beneficial for such studies.[252-255] For example, Patra and coworkers utilized genetic algorithms with density functional theory to anticipate the role of defects in MoS_2 to convert the semiconducting 2H phase to the metallic 1T phase.[256] Ahmed et al. performed a similar computational study on the effects of porosities of electrode materials on the supercapacitor performances.[252] Such an approach may be adopted to optimize the pore-rich architectures of MOF-based electrodes to enhance energy storage performances. The ability of rapid calculation and data-oriented investigation without sacrificing significant physical resources will help reduce the time and the cost of the research.

In summary, the TMD research, stemming from early graphene studies in 2004,[257] has advanced considerably and now appreciates the benefits of diverse hetero-materials. Especially, the most recent approaches integrating multi-components TMD heterostructures with molecular systems[33, 90, 93, 94, 142, 143, 159] may build a foundation to discover new physics in ultrathin materials and give rise to additional turnabilities and functionalities for the applications. The research on TMD hybrids will open new possibilities.

Author Contributions

J. Ji and J.H. Choi conceived the idea. J. Ji prepared the contents of this article and wrote the original draft. J.H. Choi supervised the entire process. The manuscript was revised and edited by all authors. The authors have approved the final version of the manuscript.

Acknowledgements

This work was supported by the U.S. National Science Foundation (award no. 1334088).

References

(1) Zeng, M.; Xiao, Y.; Liu, J.; Yang, K.; Fu, L. Exploring Two-Dimensional Materials toward the Next-Generation Circuits: From Monomer Design to Assembly Control. *Chemical Reviews* **2018**, *118*, 6236-6296.

(2) Khan, K.; Tareen, A. K.; Aslam, M.; Wang, R.; Zhang, Y.; Mahmood, A.; Ouyang, Z.; Zhang, H.; Guo, Z. Recent developments in emerging two-dimensional materials and their applications. *Journal of Materials Chemistry C* **2020**, *8*, 387-440.

(3) Manzeli, S.; Ovchinnikov, D.; Pasquier, D.; Yazyev, O. V.; Kis, A. 2D transition metal dichalcogenides. *Nature Reviews Materials* **2017**, *2*, 17033.

(4) Allen, M. J.; Tung, V. C.; Kaner, R. B. Honeycomb Carbon: A Review of Graphene. *Chemical Reviews* **2010**, *110*, 132-145.

(5) Jiang, X.-F.; Weng, Q.; Wang, X.-B.; Li, X.; Zhang, J.; Golberg, D.; Bando, Y. Recent Progress on Fabrications and Applications of Boron Nitride Nanomaterials: A Review. *Journal of Materials Science & Technology* **2015**, *31*, 589-598.

(6) Ayari, A.; Cobas, E.; Ogundadegbe, O.; Fuhrer, M. S. Realization and electrical characterization of ultrathin crystals of layered transition-metal dichalcogenides. *Journal of Applied Physics* **2007**, *101*, 014507.

(7) Tong, X.; Ashalley, E.; Lin, F.; Li, H.; Wang, Z. M. Advances in MoS2-Based Field Effect Transistors (FETs). *Nano-Micro Letters* **2015**, *7*, 203-218.

(8) Chhowalla, M.; Jena, D.; Zhang, H. Two-dimensional semiconductors for transistors. *Nature Reviews Materials* **2016**, *1*, 16052.

(9) Radisavljevic, B.; Radenovic, A.; Brivio, J.; Giacometti, V.; Kis, A. Single-layer MoS2 transistors. *Nature Nanotechnology* **2011**, *6*, 147-150.

(10) Zhang, H.; Ji, J.; Gonzalez, A. A.; Choi, J. H. Tailoring photoelectrochemical properties of semiconducting transition metal dichalcogenide nanolayers with porphyrin functionalization. *Journal of Materials Chemistry C* **2017**, *5*, 11233-11238.

(11) Choi, J.; Zhang, H.; Choi, J. H. Modulating Optoelectronic Properties of Two-Dimensional Transition Metal Dichalcogenide Semiconductors by Photoinduced Charge Transfer. *ACS Nano* **2016**, *10*, 1671-1680.

(12) Huo, N.; Konstantatos, G. Ultrasensitive all-2D MoS2 phototransistors enabled by an out-of-plane MoS2 PN homojunction. *Nature Communications* **2017**, *8*, 572.

(13) Gao, L. Flexible Device Applications of 2D Semiconductors. *Small* **2017**, *13*, 1603994.

(14) Akinwande, D.; Petrone, N.; Hone, J. Two-dimensional flexible nanoelectronics. *Nature Communications* **2014**, *5*, 5678.

(15) Liu, Y.; Weiss, N. O.; Duan, X.; Cheng, H.-C.; Huang, Y.; Duan, X. Van der Waals heterostructures and devices. *Nature Reviews Materials* **2016**, *1*, 16042.

(16) Liao, W.; Huang, Y.; Wang, H.; Zhang, H. Van der Waals heterostructures for optoelectronics: Progress and prospects. *Applied Materials Today* **2019**, *16*, 435-455.

(17) Song, J. C. W.; Gabor, N. M. Electron quantum metamaterials in van der Waals heterostructures. *Nature Nanotechnology* **2018**, *13*, 986-993.

(18) Prabhu, P.; Jose, V.; Lee, J.-M. Design Strategies for Development of TMD-Based Heterostructures in Electrochemical Energy Systems. *Matter* **2020**, *2*, 526-553.

(19) Li, C.; Cao, Q.; Wang, F.; Xiao, Y.; Li, Y.; Delaunay, J.-J.; Zhu, H. Engineering graphene and TMDs based van der Waals heterostructures for photovoltaic and photoelectrochemical solar energy conversion. *Chemical Society Reviews* **2018**, *47*, 4981-5037.

(20) Liu, H.; Hussain, S.; Ali, A.; Naqvi, B. A.; Vikraman, D.; Jeong, W.; Song, W.; An, K.-S.; Jung, J. A vertical WSe2–MoSe2 p–n heterostructure with tunable gate rectification. *RSC Advances* **2018**, *8*, 25514-25518.

(21) Zhang, N.; Surrente, A.; Baranowski, M.; Maude, D. K.; Gant, P.; Castellanos-Gomez, A.; Plochocka, P. Moiré Intralayer Excitons in a MoSe2/MoS2 Heterostructure. *Nano Letters* **2018**, *18*, 7651-7657.

(22) Yang, W.; Kawai, H.; Bosman, M.; Tang, B.; Chai, J.; Tay, W. L.; Yang, J.; Seng, H. L.; Zhu, H.; Gong, H.; Liu, H.; Goh, K. E. J.; Wang, S.; Chi, D. Interlayer interactions in 2D WS2/MoS2 heterostructures monolithically grown by in situ physical vapor deposition. *Nanoscale* **2018**, *10*, 22927-22936.

(23) Lee, W.; Lu, L.-S.; Chang, W.-H.; Shih, C.-K. Momentum-Resolved Electronic Structures of a Monolayer-MoS2/Multilayer-MoSe2 Heterostructure. *The Journal of Physical Chemistry C* **2021**, *125*, 16591-16597.

(24) Kunstmann, J.; Mooshammer, F.; Nagler, P.; Chaves, A.; Stein, F.; Paradiso, N.; Plechinger, G.; Strunk, C.; Schüller, C.; Seifert, G.; Reichman, D. R.; Korn, T. Momentum-space indirect interlayer excitons in transition-metal dichalcogenide van der Waals heterostructures. *Nature Physics* **2018**, *14*, 801-805.

(25) Bertolazzi, S.; Gobbi, M.; Zhao, Y.; Backes, C.; Samorì, P. Molecular chemistry approaches for tuning the properties of two-dimensional transition metal dichalcogenides. *Chemical Society Reviews* **2018**, *47*, 6845-6888.

(26) Wang, X.; Li, H.; Li, H.; Lin, S.; Ding, W.; Zhu, X.; Sheng, Z.; Wang, H.; Zhu, X.; Sun, Y. 2D/2D 1T-MoS2/Ti3C2 MXene Heterostructure with Excellent Supercapacitor Performance. *Advanced Functional Materials* **2020**, *30*, 0190302.

(27) Baig, M. M.; Pervaiz, E.; Yang, M.; Gul, I. H. High-Performance Supercapacitor Electrode Obtained by Directly Bonding 2D Materials: Hierarchal MoS2 on Reduced Graphene Oxide. *Frontiers in Materials* **2020**, *7*, 323.

(28) Thangappan, R.; Kalaiselvam, S.; Elayaperumal, A.; Jayavel, R.; Arivanandhan, M.; Karthikeyan, R.; Hayakawa, Y. Graphene decorated with MoS2 nanosheets: a synergetic energy storage composite electrode for supercapacitor applications. *Dalton Transactions* **2016**, *45*, 2637-2646.

(29) Huang, Y. L.; Zheng, Y. J.; Song, Z.; Chi, D.; Wee, A. T. S.; Quek, S. Y. The organic–2D transition metal dichalcogenide heterointerface. *Chemical Society Reviews* **2018**, *47*, 3241-3264.

(30) Pei, K.; Zhai, T. Emerging 2D Organic-Inorganic Heterojunctions. *Cell Reports Physical Science* **2020**, *1*, 100166.

(31) Ahmadi, M.; Zabihi, O.; Jeon, S.; Yoonessi, M.; Dasari, A.; Ramakrishna, S.; Naebe, M. 2D transition metal dichalcogenide nanomaterials: advances, opportunities, and challenges in multi-functional polymer nanocomposites. *Journal of Materials Chemistry A* **2020**, *8*, 845-883.

(32) Hu, Z.; Wu, Z.; Han, C.; He, J.; Ni, Z.; Chen, W. Two-dimensional transition metal dichalcogenides: interface and defect engineering. *Chemical Society Reviews* **2018**, *47*, 3100-3128.

(33) Ji, J.; Delehey, C. M.; Houpt, D. N.; Heighway, M. K.; Lee, T.; Choi, J. H. Selective Chemical Modulation of Interlayer Excitons in Atomically Thin Heterostructures. *Nano Letters* **2020**, *20*, 2500-2506.

(34) Ji, J.; Choi, J. H. Layer-Number-Dependent Electronic and Optoelectronic Properties of 2D WSe2-Organic Hybrid Heterojunction. *Advanced Materials Interfaces* **2019**, *6*, 1900637.

(35) Fahlman, M.; Fabiano, S.; Gueskine, V.; Simon, D.; Berggren, M.; Crispin, X. Interfaces in organic electronics. *Nature Reviews Materials* **2019**, *4*, 627-650.

(36) Morin, J.-F. Recent advances in the chemistry of vat dyes for organic electronics. *Journal of Materials Chemistry C* **2017**, *5*, 12298-12307.

(37) Tien, H.-C.; Huang, Y.-W.; Chiu, Y.-C.; Cheng, Y.-H.; Chueh, C.-C.; Lee, W.-Y. Intrinsically stretchable polymer semiconductors: molecular design, processing and device applications. *Journal of Materials Chemistry C* **2021**, *9*, 2660-2684.

(38) Yarali, M.; Zhong, Y.; Reed, S. N.; Wang, J.; Ulman, K. A.; Charboneau, D. J.; Curley, J. B.; Hynek, D. J.; Pondick, J. V.; Yazdani, S.; Hazari, N.; Quek, S. Y.; Wang, H.; Cha, J. J. Near-Unity Molecular Doping Efficiency in Monolayer MoS2. *Advanced Electronic Materials* **2021**, *7*, 2000873.

(39) Sim, D. M.; Kim, M.; Yim, S.; Choi, M.-J.; Choi, J.; Yoo, S.; Jung, Y. S. Controlled Doping of Vacancy-Containing Few-Layer MoS2 via Highly Stable Thiol-Based Molecular Chemisorption. *ACS Nano* **2015**, *9*, 12115-12123.

(40) Makarova, M.; Okawa, Y.; Aono, M. Selective Adsorption of Thiol Molecules at Sulfur Vacancies on MoS2(0001), Followed by Vacancy Repair via S–C Dissociation. *The Journal of Physical Chemistry C* **2012**, *116*, 22411-22416.

(41) Hong, J.; Hu, Z.; Probert, M.; Li, K.; Lv, D.; Yang, X.; Gu, L.; Mao, N.; Feng, Q.; Xie, L.; Zhang, J.; Wu, D.; Zhang, Z.; Jin, C.; Ji, W.; Zhang, X.; Yuan, J.; Zhang, Z. Exploring atomic defects in molybdenum disulphide monolayers. *Nature Communications* **2015**, *6*, 6293.

(42) Chhowalla, M.; Shin, H. S.; Eda, G.; Li, L.-J.; Loh, K. P.; Zhang, H. The chemistry of two-dimensional layered transition metal dichalcogenide nanosheets. *Nature Chemistry* **2013**, *5*, 263-275.

(43) Zhang, Y.; Yao, Y.; Sendeku, M. G.; Yin, L.; Zhan, X.; Wang, F.; Wang, Z.; He, J. Recent Progress in CVD Growth of 2D Transition Metal Dichalcogenides and Related Heterostructures. *Advanced Materials* **2019**, *31*, 1901694.

(44) Sokolikova, M. S.; Mattevi, C. Direct synthesis of metastable phases of 2D transition metal dichalcogenides. *Chemical Society Reviews* **2020**, *49*, 3952-3980.

(45) Lee, Y.; Park, S.; Kim, H.; Han, G. H.; Lee, Y. H.; Kim, J. Characterization of the structural defects in CVD-grown monolayered MoS2 using near-field photoluminescence imaging. *Nanoscale* **2015**, *7*, 11909-11914.

(46) Chae, W. H.; Cain, J. D.; Hanson, E. D.; Murthy, A. A.; Dravid, V. P. Substrate-induced strain and charge doping in CVD-grown monolayer MoS2. *Applied Physics Letters* **2017**, *111*, 143106.

(47) Lee, J. E.; Jung, J.; Ko, T. Y.; Kim, S.; Kim, S.-I.; Nah, J.; Ryu, S.; Nam, K. T.; Lee, M. H. Catalytic synergy effect of MoS2/reduced graphene oxide hybrids for a highly efficient hydrogen evolution reaction. *RSC Advances* **2017**, *7*, 5480-5487.

(48) Mu, H.; Wan, J.; Wu, Y.; Xu, J.; Wang, L.; Cao, X. Novel polymer supported graphene and molybdenum sulfide as highly efficient cocatalyst for photocatalytic hydrogen evolution. *International Journal of Hydrogen Energy* **2018**, *43*, 18105-18114.

(49) Xie, J.; Zhang, H.; Li, S.; Wang, R.; Sun, X.; Zhou, M.; Zhou, J.; Lou, X. W.; Xie, Y. Defect-Rich MoS2 Ultrathin Nanosheets with Additional Active Edge Sites for Enhanced Electrocatalytic Hydrogen Evolution. *Advanced Materials* **2013**, *25*, 5807-5813.

(50) Huang, Z.; Zhang, L.; Li, M.; Ran, W.; Lu, Y.; Yang, B.; Long, Z. Hollow Tubular Morphology of MoS2 via the Solvothermal Method with a Single Source Precursor.

Nanoscience and Nanotechnology Letters **2017**, *9*, 56-60.

(51) Song, W.; Nie, T.; Lai, W.; Yang, W.; Jiang, X. Tailoring the morphology of Co-doped MoS2 for enhanced hydrodeoxygenation performance of p-cresol. *CrystEngComm* **2018**, *20*, 4069-4074.

(52) Li, H.; Wu, J.; Yin, Z.; Zhang, H. Preparation and Applications of Mechanically Exfoliated Single-Layer and Multilayer MoS2 and WSe2 Nanosheets. *Accounts of Chemical Research* **2014**, *47*, 1067-1075.

(53) Pradhan, N. R.; Rhodes, D.; Xin, Y.; Memaran, S.; Bhaskaran, L.; Siddiq, M.; Hill, S.; Ajayan, P. M.; Balicas, L. Ambipolar Molybdenum Diselenide Field-Effect Transistors: Field-Effect and Hall Mobilities. *ACS Nano* **2014**, *8*, 7923-7929.

(54) Iqbal, M. W.; Iqbal, M. Z.; Khan, M. F.; Shehzad, M. A.; Seo, Y.; Park, J. H.; Hwang, C.; Eom, J. High-mobility and air-stable single-layer WS2 field-effect transistors sandwiched between chemical vapor deposition-grown hexagonal BN films. *Scientific Reports* **2015**, *5*, 10699.

(55) Fang, H.; Chuang, S.; Chang, T. C.; Takei, K.; Takahashi, T.; Javey, A. High-Performance Single Layered WSe2 p-FETs with Chemically Doped Contacts. *Nano Letters* **2012**, *12*, 3788-3792.

(56) Nepal, N. K.; Yu, L.; Yan, Q.; Ruzsinszky, A. First-principles study of mechanical and electronic properties of bent monolayer transition metal dichalcogenides. *Physical Review Materials* **2019**, *3*, 073601.

(57) Han, S. A.; Bhatia, R.; Kim, S.-W. Synthesis, properties and potential applications of two-dimensional transition metal dichalcogenides. *Nano Convergence* **2015**, *2*, 17.

(58) Wang, H.; Li, C.; Fang, P.; Zhang, Z.; Zhang, J. Z. Synthesis, properties, and optoelectronic applications of two-dimensional MoS2 and MoS2-based heterostructures. *Chemical Society Reviews* **2018**, *47*, 6101-6127.

(59) Zhu, H.; Wang, Y.; Xiao, J.; Liu, M.; Xiong, S.; Wong, Z. J.; Ye, Z.; Ye, Y.; Yin, X.; Zhang, X. Observation of piezoelectricity in free-standing monolayer MoS2. *Nature Nanotechnology* **2015**, *10*, 151-155.

(60) Kumar, A.; Yagodkin, D.; Stetzuhn, N.; Kovalchuk, S.; Melnikov, A.; Elliott, P.; Sharma, S.; Gahl, C.; Bolotin, K. I. Spin/Valley Coupled Dynamics of Electrons and Holes at the MoS2–MoSe2 Interface. *Nano Letters* **2021**, *21*, 7123-7130.

(61) Geim, A. K.; Grigorieva, I. V. Van der Waals heterostructures. *Nature* **2013**, *499*, 419-425.

(62) Nourbakhsh, A.; Zubair, A.; Dresselhaus, M. S.; Palacios, T. Transport Properties of a

MoS2/WSe2 Heterojunction Transistor and Its Potential for Application. *Nano Letters* **2016**, *16*, 1359-1366.

(63) Hu, R.; Wu, E.; Xie, Y.; Liu, J. Multifunctional anti-ambipolar p-n junction based on MoTe2/MoS2 heterostructure. *Applied Physics Letters* **2019**, *115*, 073104.

(64) Li, Y.; Wang, Y.; Huang, L.; Wang, X.; Li, X.; Deng, H.-X.; Wei, Z.; Li, J. Anti-Ambipolar Field-Effect Transistors Based On Few-Layer 2D Transition Metal Dichalcogenides. *ACS Applied Materials & Interfaces* **2016**, *8*, 15574-15581.

(65) On, S.; Kim, Y.-J.; Lee, H.-K.; Yoo, H. Ambipolar and anti-ambipolar thin-film transistors from edge-on small-molecule heterostructures. *Applied Surface Science* **2021**, *542*, 148616.

(66) Shim, J.; Jo, S.-H.; Kim, M.; Song, Y. J.; Kim, J.; Park, J.-H. Light-Triggered Ternary Device and Inverter Based on Heterojunction of van der Waals Materials. *ACS Nano* **2017**, *11*, 6319-6327.

(67) Beck, M. E.; Shylendra, A.; Sangwan, V. K.; Guo, S.; Gaviria Rojas, W. A.; Yoo, H.; Bergeron, H.; Su, K.; Trivedi, A. R.; Hersam, M. C. Spiking neurons from tunable Gaussian heterojunction transistors. *Nature Communications* **2020**, *11*, 1565.

(68) Liu, F.; Qiu, C.; Zhang, Z.; Peng, L.; Wang, J.; Guo, H. Dirac Electrons at the Source: Breaking the 60-mV/Decade Switching Limit. *IEEE Transactions on Electron Devices* **2018**, *65*, 2736-2743.

(69) Georgiou, T.; Jalil, R.; Belle, B. D.; Britnell, L.; Gorbachev, R. V.; Morozov, S. V.; Kim, Y.-J.; Gholinia, A.; Haigh, S. J.; Makarovsky, O.; Eaves, L.; Ponomarenko, L. A.; Geim, A. K.; Novoselov, K. S.; Mishchenko, A. Vertical field-effect transistor based on graphene–WS2 heterostructures for flexible and transparent electronics. *Nature Nanotechnology* **2013**, *8*, 100-103.

(70) Rivera, P.; Schaibley, J. R.; Jones, A. M.; Ross, J. S.; Wu, S.; Aivazian, G.; Klement, P.; Seyler, K.; Clark, G.; Ghimire, N. J.; Yan, J.; Mandrus, D. G.; Yao, W.; Xu, X. Observation of long-lived interlayer excitons in monolayer MoSe2–WSe2 heterostructures. *Nature Communications* **2015**, *6*, 6242.

(71) Ciarrocchi, A.; Unuchek, D.; Avsar, A.; Watanabe, K.; Taniguchi, T.; Kis, A. Polarization switching and electrical control of interlayer excitons in two-dimensional van der Waals heterostructures. *Nature Photonics* **2019**, *13*, 131-136.

(72) Miller, B.; Steinhoff, A.; Pano, B.; Klein, J.; Jahnke, F.; Holleitner, A.; Wurstbauer, U. Long-Lived Direct and Indirect Interlayer Excitons in van der Waals Heterostructures. *Nano Letters* **2017**, *17*, 5229-5237.

(73) Unuchek, D.; Ciarrocchi, A.; Avsar, A.; Watanabe, K.; Taniguchi, T.; Kis, A. Room-

temperature electrical control of exciton flux in a van der Waals heterostructure. *Nature* **2018**, *560*, 340-344.

(74) Jiang, Y.; Chen, S.; Zheng, W.; Zheng, B.; Pan, A. Interlayer exciton formation, relaxation, and transport in TMD van der Waals heterostructures. *Light: Science & Applications* **2021**, *10*, 72.

(75) Cai, Z.; Liu, B.; Zou, X.; Cheng, H.-M. Chemical Vapor Deposition Growth and Applications of Two-Dimensional Materials and Their Heterostructures. *Chemical Reviews* **2018**, *118*, 6091-6133.

(76) McManus, D.; Vranic, S.; Withers, F.; Sanchez-Romaguera, V.; Macucci, M.; Yang, H.; Sorrentino, R.; Parvez, K.; Son, S.-K.; Iannaccone, G.; Kostarelos, K.; Fiori, G.; Casiraghi, C. Water-based and biocompatible 2D crystal inks for all-inkjet-printed heterostructures. *Nature Nanotechnology* **2017**, *12*, 343-350.

(77) Yun, T.; Kim, J.-S.; Shim, J.; Choi, D. S.; Lee, K. E.; Koo, S. H.; Kim, I.; Jung, H. J.; Yoo, H.-W.; Jung, H.-T.; Kim, S. O. Ultrafast Interfacial Self-Assembly of 2D Transition Metal Dichalcogenides Monolayer Films and Their Vertical and In-Plane Heterostructures. *ACS Applied Materials & Interfaces* **2017**, *9*, 1021-1028.

(78) Illarionov, Y. Y.; Rzepa, G.; Waltl, M.; Knobloch, T.; Grill, A.; Furchi, M. M.; Mueller, T.; Grasser, T. The role of charge trapping in MoS 2 /SiO 2 and MoS 2 /hBN field-effect transistors. *2D Materials* **2016**, *3*, 035004.

(79) Jariwala, D.; Marks, T. J.; Hersam, M. C. Mixed-dimensional van der Waals heterostructures. *Nature Materials* **2017**, *16*, 170-181.

(80) Zhang, H.; Choi, J.; Ramani, A.; Voiry, D.; Natoli, S. N.; Chhowalla, M.; McMillin, D. R.; Choi, J. H. Engineering Chemically Exfoliated Large-Area Two-Dimensional MoS2 Nanolayers with Porphyrins for Improved Light Harvesting. *ChemPhysChem* **2016**, *17*, 2854-2862.

(81) Liu, F.; Chow, W. L.; He, X.; Hu, P.; Zheng, S.; Wang, X.; Zhou, J.; Fu, Q.; Fu, W.; Yu, P.; Zeng, Q.; Fan, H. J.; Tay, B. K.; Kloc, C.; Liu, Z. Van der Waals p–n Junction Based on an Organic–Inorganic Heterostructure. *Advanced Functional Materials* **2015**, *25*, 5865-5871.

(82) He, D.; Pan, Y.; Nan, H.; Gu, S.; Yang, Z.; Wu, B.; Luo, X.; Xu, B.; Zhang, Y.; Li, Y.; Ni, Z.; Wang, B.; Zhu, J.; Chai, Y.; Shi, Y.; Wang, X. A van der Waals pn heterojunction with organic/inorganic semiconductors. *Applied Physics Letters* **2015**, *107*, 183103.

(83) Vélez, S.; Ciudad, D.; Island, J.; Buscema, M.; Txoperena, O.; Parui, S.; Steele, G. A.; Casanova, F.; van der Zant, H. S. J.; Castellanos-Gomez, A.; Hueso, L. E. Gate-tunable diode and photovoltaic effect in an organic–2D layered material p–n junction. *Nanoscale* **2015**, *7*,

15442-15449.
(84) Shastry, T. A.; Balla, I.; Bergeron, H.; Amsterdam, S. H.; Marks, T. J.; Hersam, M. C. Mutual Photoluminescence Quenching and Photovoltaic Effect in Large-Area Single-Layer MoS2–Polymer Heterojunctions. *ACS Nano* **2016**, *10*, 10573-10579.
(85) Qiu, H.; Liu, Z.; Yao, Y.; Herder, M.; Hecht, S.; Samorì, P. Simultaneous Optical Tuning of Hole and Electron Transport in Ambipolar WSe2 Interfaced with a Bicomponent Photochromic Layer: From High-Mobility Transistors to Flexible Multilevel Memories. *Advanced Materials* **2020**, *32*, 1907903.
(86) Li, P.; Sui, Q.; Guo, M.-Y.; Yang, S.-L.; Bu, R.; Gao, E.-Q. Selective chemochromic and chemically-induced photochromic response of a metal–organic framework. *Chemical Communications* **2020**, *56*, 5929-5932.
(87) Welsh, T. A.; Draper, E. R. Water soluble organic electrochromic materials. *RSC Advances* **2021**, *11*, 5245-5264.
(88) Wang, S.; Xu, Z.; Wang, T.; Xiao, T.; Hu, X.-Y.; Shen, Y.-Z.; Wang, L. Warm/cool-tone switchable thermochromic material for smart windows by orthogonally integrating properties of pillar[6]arene and ferrocene. *Nature Communications* **2018**, *9*, 1737.
(89) Shokouh, S. H. H.; Jeon, P. J.; Pezeshki, A.; Choi, K.; Lee, H. S.; Kim, J. S.; Park, E. Y.; Im, S. High-Performance, Air-Stable, Top-Gate, p-Channel WSe2 Field-Effect Transistor with Fluoropolymer Buffer Layer. *Advanced Functional Materials* **2015**, *25*, 7208-7214.
(90) Ji, J.; Choi, J. H. Understanding the Effects of Dielectric Property, Separation Distance, and Band Alignment on Interlayer Excitons in 2D Hybrid MoS2/WSe2 Heterostructures. *ACS Applied Electronic Materials* **2021**, *3*, 3052-3059.
(91) Lin, Y.; Ling, X.; Yu, L.; Huang, S.; Hsu, A. L.; Lee, Y.-H.; Kong, J.; Dresselhaus, M. S.; Palacios, T. Dielectric Screening of Excitons and Trions in Single-Layer MoS2. *Nano Letters* **2014**, *14*, 5569-5576.
(92) Yu, Z.; Pan, Y.; Shen, Y.; Wang, Z.; Ong, Z.-Y.; Xu, T.; Xin, R.; Pan, L.; Wang, B.; Sun, L.; Wang, J.; Zhang, G.; Zhang, Y. W.; Shi, Y.; Wang, X. Towards intrinsic charge transport in monolayer molybdenum disulfide by defect and interface engineering. *Nature Communications* **2014**, *5*, 5290.
(93) Qiao, J.-W.; Niu, M.-S.; Wen, Z.-C.; Yang, X.-K.; Chen, Z.-H.; Wang, Y.-X.; Feng, L.; Qin, W.; Hao, X.-T. Efficient photoluminescence enhancement and tunable photocarrier transfer in vertical 2D organic–inorganic heterostructure by energy funneling. *2D Materials* **2021**, *8*, 025026.
(94) Kim, J. Y.; Park, H. J.; Lee, S.-h.; Seo, C.; Kim, J.; Joo, J. Distinctive Field-Effect

Transistors and Ternary Inverters Using Cross-Type WSe2/MoS2 Heterojunctions Treated with Polymer Acid. *ACS Applied Materials & Interfaces* **2020**, *12*, 36530-36539.

(95) Chamlagain, B.; Withanage, S. S.; Johnston, A. C.; Khondaker, S. I. Scalable lateral heterojunction by chemical doping of 2D TMD thin films. *Scientific Reports* **2020**, *10*, 12970.

(96) Wang, J.; Yu, H.; Zhou, X.; Liu, X.; Zhang, R.; Lu, Z.; Zheng, J.; Gu, L.; Liu, K.; Wang, D.; Jiao, L. Probing the crystallographic orientation of two-dimensional atomic crystals with supramolecular self-assembly. *Nature Communications* **2017**, *8*, 377.

(97) Tian, T.; Shih, C.-J. Molecular Epitaxy on Two-Dimensional Materials: The Interplay between Interactions. *Industrial & Engineering Chemistry Research* **2017**, *56*, 10552-10581.

(98) Park, S.; Mutz, N.; Kovalenko, S. A.; Schultz, T.; Shin, D.; Aljarb, A.; Li, L.-J.; Tung, V.; Amsalem, P.; List-Kratochvil, E. J. W.; Stähler, J.; Xu, X.; Blumstengel, S.; Koch, N. Type-I Energy Level Alignment at the PTCDA—Monolayer MoS2 Interface Promotes Resonance Energy Transfer and Luminescence Enhancement. *Advanced Science* **2021**, *8*, 2100215.

(99) Park, J. H.; Sanne, A.; Guo, Y.; Amani, M.; Zhang, K.; Movva, H. C. P.; Robinson, J. A.; Javey, A.; Robertson, J.; Banerjee, S. K.; Kummel, A. C. Defect passivation of transition metal dichalcogenides via a charge transfer van der Waals interface. *Science Advances* **2017**, *3*, e1701661.

(100) Wang, S.; Chen, C.; Yu, Z.; He, Y.; Chen, X.; Wan, Q.; Shi, Y.; Zhang, D. W.; Zhou, H.; Wang, X.; Zhou, P. A MoS2/PTCDA Hybrid Heterojunction Synapse with Efficient Photoelectric Dual Modulation and Versatility. *Advanced Materials* **2019**, *31*, 1806227.

(101) He, X.; Zhang, L.; Chua, R.; Wong, P. K. J.; Arramel, A.; Feng, Y. P.; Wang, S. J.; Chi, D.; Yang, M.; Huang, Y. L.; Wee, A. T. S. Selective self-assembly of 2,3-diaminophenazine molecules on MoSe2 mirror twin boundaries. *Nature Communications* **2019**, *10*, 2847.

(102) Lin, X.; Lu, J. C.; Shao, Y.; Zhang, Y. Y.; Wu, X.; Pan, J. B.; Gao, L.; Zhu, S. Y.; Qian, K.; Zhang, Y. F.; Bao, D. L.; Li, L. F.; Wang, Y. Q.; Liu, Z. L.; Sun, J. T.; Lei, T.; Liu, C.; Wang, J. O.; Ibrahim, K.; Leonard, D. N.; Zhou, W.; Guo, H. M.; Wang, Y. L.; Du, S. X.; Pantelides, S. T.; Gao, H. J. Intrinsically patterned two-dimensional materials for selective adsorption of molecules and nanoclusters. *Nature Materials* **2017**, *16*, 717-721.

(103) Choi, J.; Chen, H.; Li, F.; Yang, L.; Kim, S. S.; Naik, R. R.; Ye, P. D.; Choi, J. H. Nanomanufacturing of 2D Transition Metal Dichalcogenide Materials Using Self-Assembled DNA Nanotubes. *Small* **2015**, *11*, 5520-5527.

(104) Ding, Q.; Czech, K. J.; Zhao, Y.; Zhai, J.; Hamers, R. J.; Wright, J. C.; Jin, S. Basal-Plane Ligand Functionalization on Semiconducting 2H-MoS2 Monolayers. *ACS Applied Materials & Interfaces* **2017**, *9*, 12734-12742.

(105) Im, H.; Bala, A.; So, B.; Kim, Y. J.; Kim, S. Customization of MoS2 Phototransistors via Thiol-Based Functionalization. *Advanced Electronic Materials* **2021**, *7*, 2100644.
(106) Chu, X. S.; Yousaf, A.; Li, D. O.; Tang, A. A.; Debnath, A.; Ma, D.; Green, A. A.; Santos, E. J. G.; Wang, Q. H. Direct Covalent Chemical Functionalization of Unmodified Two-Dimensional Molybdenum Disulfide. *Chemistry of Materials* **2018**, *30*, 2112-2128.
(107) Li, D. O.; Chu, X. S.; Wang, Q. H. Reaction Kinetics for the Covalent Functionalization of Two-Dimensional MoS2 by Aryl Diazonium Salts. *Langmuir* **2019**, *35*, 5693-5701.
(108) Cho, K.; Pak, J.; Kim, J.-K.; Kang, K.; Kim, T.-Y.; Shin, J.; Choi, B. Y.; Chung, S.; Lee, T. Contact-Engineered Electrical Properties of MoS2 Field-Effect Transistors via Selectively Deposited Thiol-Molecules. *Advanced Materials* **2018**, *30*, 1705540.
(109) Voiry, D.; Goswami, A.; Kappera, R.; Silva, C. d. C. C. e.; Kaplan, D.; Fujita, T.; Chen, M.; Asefa, T.; Chhowalla, M. Covalent functionalization of monolayered transition metal dichalcogenides by phase engineering. *Nature Chemistry* **2015**, *7*, 45-49.
(110) Raja, A.; Chaves, A.; Yu, J.; Arefe, G.; Hill, H. M.; Rigosi, A. F.; Berkelbach, T. C.; Nagler, P.; Schüller, C.; Korn, T.; Nuckolls, C.; Hone, J.; Brus, L. E.; Heinz, T. F.; Reichman, D. R.; Chernikov, A. Coulomb engineering of the bandgap and excitons in two-dimensional materials. *Nature Communications* **2017**, *8*, 15251.
(111) Zhang, L.; Sharma, A.; Zhu, Y.; Zhang, Y.; Wang, B.; Dong, M.; Nguyen, H. T.; Wang, Z.; Wen, B.; Cao, Y.; Liu, B.; Sun, X.; Yang, J.; Li, Z.; Kar, A.; Shi, Y.; Macdonald, D.; Yu, Z.; Wang, X.; Lu, Y. Efficient and Layer-Dependent Exciton Pumping across Atomically Thin Organic–Inorganic Type-I Heterostructures. *Advanced Materials* **2018**, *30*, 1803986.
(112) Chamlagain, B.; Li, Q.; Ghimire, N. J.; Chuang, H.-J.; Perera, M. M.; Tu, H.; Xu, Y.; Pan, M.; Xaio, D.; Yan, J.; Mandrus, D.; Zhou, Z. Mobility Improvement and Temperature Dependence in MoSe2 Field-Effect Transistors on Parylene-C Substrate. *ACS Nano* **2014**, *8*, 5079-5088.
(113) Drüppel, M.; Deilmann, T.; Krüger, P.; Rohlfing, M. Diversity of trion states and substrate effects in the optical properties of an MoS2 monolayer. *Nature Communications* **2017**, *8*, 2117.
(114) Winkler, C.; Harivyasi, S. S.; Zojer, E. Controlling the electronic properties of van der Waals heterostructures by applying electrostatic design. *2D Materials* **2018**, *5*, 035019.
(115) Güven, K.; Tanatar, B. Simplified calculations of band-gap renormalization in quantum-wells. *Superlattices and Microstructures* **1996**, *20*, 81-85.
(116) Neaton, J. B.; Hybertsen, M. S.; Louie, S. G. Renormalization of Molecular Electronic Levels at Metal-Molecule Interfaces. *Physical Review Letters* **2006**, *97*, 216405.

(117) Shokr, F. S. Evaluation of the optical properties of photoconductive Eosin/PMMA nanocomposite film for flexible optoelectronic applications. *Optik* **2017**, *149*, 270-276.
(118) Qiu, Z.; Trushin, M.; Fang, H.; Verzhbitskiy, I.; Gao, S.; Laksono, E.; Yang, M.; Lyu, P.; Li, J.; Su, J.; Telychko, M.; Watanabe, K.; Taniguchi, T.; Wu, J.; Neto, A. H. C.; Yang, L.; Eda, G.; Adam, S.; Lu, J. Giant gate-tunable bandgap renormalization and excitonic effects in a 2D semiconductor. *Science Advances* **2019**, *5*, eaaw2347.
(119) Street, R. A. Doping and the Fermi Energy in Amorphous Silicon. *Physical Review Letters* **1982**, *49*, 1187-1190.
(120) Cui, Y.; Duan, X.; Hu, J.; Lieber, C. M. Doping and Electrical Transport in Silicon Nanowires. *The Journal of Physical Chemistry B* **2000**, *104*, 5213-5216.
(121) Lin, Y.-C.; Torsi, R.; Geohegan, D. B.; Robinson, J. A.; Xiao, K. Controllable Thin-Film Approaches for Doping and Alloying Transition Metal Dichalcogenides Monolayers. *Advanced Science* **2021**, *8*, 2004249.
(122) Stergiou, A.; Tagmatarchis, N. Molecular Functionalization of Two-Dimensional MoS2 Nanosheets. *Chemistry – A European Journal* **2018**, *24*, 18246-18257.
(123) Choi, J.; Zhang, H.; Du, H.; Choi, J. H. Understanding Solvent Effects on the Properties of Two-Dimensional Transition Metal Dichalcogenides. *ACS Applied Materials & Interfaces* **2016**, *8*, 8864-8869.
(124) Jo, S.-H.; Park, H.-Y.; Kang, D.-H.; Shim, J.; Jeon, J.; Choi, S.; Kim, M.; Park, Y.; Lee, J.; Song, Y. J.; Lee, S.; Park, J.-H. Broad Detection Range Rhenium Diselenide Photodetector Enhanced by (3-Aminopropyl)Triethoxysilane and Triphenylphosphine Treatment. *Advanced Materials* **2016**, *28*, 6711-6718.
(125) Kiriya, D.; Tosun, M.; Zhao, P.; Kang, J. S.; Javey, A. Air-Stable Surface Charge Transfer Doping of MoS2 by Benzyl Viologen. *Journal of the American Chemical Society* **2014**, *136*, 7853-7856.
(126) Benjamin, C. J.; Zhang, S.; Chen, Z. Controlled doping of transition metal dichalcogenides by metal work function tuning in phthalocyanine compounds. *Nanoscale* **2018**, *10*, 5148-5153.
(127) Peimyoo, N.; Yang, W.; Shang, J.; Shen, X.; Wang, Y.; Yu, T. Chemically Driven Tunable Light Emission of Charged and Neutral Excitons in Monolayer WS2. *ACS Nano* **2014**, *8*, 11320-11329.
(128) Kim, B.; Luo, Y.; Rhodes, D.; Bai, Y.; Wang, J.; Liu, S.; Jordan, A.; Huang, B.; Li, Z.; Taniguchi, T.; Watanabe, K.; Owen, J.; Strauf, S.; Barmak, K.; Zhu, X.; Hone, J. Free Trions with Near-Unity Quantum Yield in Monolayer MoSe2. *ACS Nano* **2022**, *16*, 140-147.

(129) Chakraborty, B.; Bera, A.; Muthu, D. V. S.; Bhowmick, S.; Waghmare, U. V.; Sood, A. K. Symmetry-dependent phonon renormalization in monolayer MoS2 transistor. *Physical Review B* **2012**, *85*, 161403.

(130) Kang, D.-H.; Kim, M.-S.; Shim, J.; Jeon, J.; Park, H.-Y.; Jung, W.-S.; Yu, H.-Y.; Pang, C.-H.; Lee, S.; Park, J.-H. High-Performance Transition Metal Dichalcogenide Photodetectors Enhanced by Self-Assembled Monolayer Doping. *Advanced Functional Materials* **2015**, *25*, 4219-4227.

(131) Seo, S. G.; Jeong, J.; Kim, S. Y.; Kumar, A.; Jin, S. H. Reversible and controllable threshold voltage modulation for n-channel MoS2 and p-channel MoTe2 field-effect transistors via multiple counter doping with ODTS/poly-L-lysine charge enhancers. *Nano Research* **2021**, *14*, 3214-3227.

(132) Daukiya, L.; Seibel, J.; De Feyter, S. Chemical modification of 2D materials using molecules and assemblies of molecules. *Advances in Physics: X* **2019**, *4*, 1625723.

(133) Wang, Y.; Gali, S. M.; Slassi, A.; Beljonne, D.; Samorì, P. Collective Dipole-Dominated Doping of Monolayer MoS2: Orientation and Magnitude Control via the Supramolecular Approach. *Advanced Functional Materials* **2020**, *30*, 2002846.

(134) Najmaei, S.; Zou, X.; Er, D.; Li, J.; Jin, Z.; Gao, W.; Zhang, Q.; Park, S.; Ge, L.; Lei, S.; Kono, J.; Shenoy, V. B.; Yakobson, B. I.; George, A.; Ajayan, P. M.; Lou, J. Tailoring the Physical Properties of Molybdenum Disulfide Monolayers by Control of Interfacial Chemistry. *Nano Letters* **2014**, *14*, 1354-1361.

(135) Jariwala, D.; Howell, S. L.; Chen, K.-S.; Kang, J.; Sangwan, V. K.; Filippone, S. A.; Turrisi, R.; Marks, T. J.; Lauhon, L. J.; Hersam, M. C. Hybrid, Gate-Tunable, van der Waals p–n Heterojunctions from Pentacene and MoS2. *Nano Letters* **2016**, *16*, 497-503.

(136) Park, H. J.; Park, C.-J.; Kim, J. Y.; Kim, M. S.; Kim, J.; Joo, J. Hybrid Characteristics of MoS2 Monolayer with Organic Semiconducting Tetracene and Application to Anti-Ambipolar Field Effect Transistor. *ACS Applied Materials & Interfaces* **2018**, *10*, 32556-32566.

(137) Huang, Y.; Zhuge, F.; Hou, J.; Lv, L.; Luo, P.; Zhou, N.; Gan, L.; Zhai, T. Van der Waals Coupled Organic Molecules with Monolayer MoS2 for Fast Response Photodetectors with Gate-Tunable Responsivity. *ACS Nano* **2018**, *12*, 4062-4073.

(138) Zhu, T.; Yuan, L.; Zhao, Y.; Zhou, M.; Wan, Y.; Mei, J.; Huang, L. Highly mobile charge-transfer excitons in two-dimensional WS2/tetracene heterostructures. *Science Advances* **2018**, *4*, eaao3104.

(139) Rijal, K.; Rudayni, F.; Kafle, T. R.; Chan, W.-L. Collective Effects of Band Offset and Wave Function Dimensionality on Impeding Electron Transfer from 2D to Organic Crystals.

The Journal of Physical Chemistry Letters **2020**, *11*, 7495-7501.

(140) Petoukhoff, C. E.; Kosar, S.; Goto, M.; Bozkurt, I.; Chhowalla, M.; Dani, K. M. Charge transfer dynamics in conjugated polymer/MoS2 organic/2D heterojunctions. *Molecular Systems Design & Engineering* **2019**, *4*, 929-938.

(141) Park, S.; Schultz, T.; Xu, X.; Wegner, B.; Aljarb, A.; Han, A.; Li, L.-J.; Tung, V. C.; Amsalem, P.; Koch, N. Demonstration of the key substrate-dependent charge transfer mechanisms between monolayer MoS2 and molecular dopants. *Communications Physics* **2019**, *2*, 109.

(142) Cheng, C.-H.; Li, Z.; Hambarde, A.; Deotare, P. B. Efficient Energy Transfer across Organic–2D Inorganic Heterointerfaces. *ACS Applied Materials & Interfaces* **2018**, *10*, 39336-39342.

(143) Zhou, G.; Shen, F.; Zhu, Z. Fast response photodetectors based on Van der Waals coupled organic molecules with MoS2-graphene. *Materials Express* **2020**, *10*, 2080-2086.

(144) Petoukhoff, C. E.; Krishna, M. B. M.; Voiry, D.; Bozkurt, I.; Deckoff-Jones, S.; Chhowalla, M.; O'Carroll, D. M.; Dani, K. M. Ultrafast Charge Transfer and Enhanced Absorption in MoS2–Organic van der Waals Heterojunctions Using Plasmonic Metasurfaces. *ACS Nano* **2016**, *10*, 9899-9908.

(145) Bettis Homan, S.; Sangwan, V. K.; Balla, I.; Bergeron, H.; Weiss, E. A.; Hersam, M. C. Ultrafast Exciton Dissociation and Long-Lived Charge Separation in a Photovoltaic Pentacene–MoS2 van der Waals Heterojunction. *Nano Letters* **2017**, *17*, 164-169.

(146) Zhong, C.; Sangwan, V. K.; Wang, C.; Bergeron, H.; Hersam, M. C.; Weiss, E. A. Mechanisms of Ultrafast Charge Separation in a PTB7/Monolayer MoS2 van der Waals Heterojunction. *The Journal of Physical Chemistry Letters* **2018**, *9*, 2484-2491.

(147) Zimmermann, J. E.; Axt, M.; Mooshammer, F.; Nagler, P.; Schüller, C.; Korn, T.; Höfer, U.; Mette, G. Ultrafast Charge-Transfer Dynamics in Twisted MoS2/WSe2 Heterostructures. *ACS Nano* **2021**, *15*, 14725-14731.

(148) Laikhtman, B.; Rapaport, R. Exciton correlations in coupled quantum wells and their luminescence blue shift. *Physical Review B* **2009**, *80*, 195313.

(149) Chowdhury, T.; Sadler, E. C.; Kempa, T. J. Progress and Prospects in Transition-Metal Dichalcogenide Research Beyond 2D. *Chemical Reviews* **2020**, *120*, 12563-12591.

(150) McDonnell, S.; Addou, R.; Buie, C.; Wallace, R. M.; Hinkle, C. L. Defect-Dominated Doping and Contact Resistance in MoS2. *ACS Nano* **2014**, *8*, 2880-2888.

(151) Li, Q.; Zhao, Y.; Ling, C.; Yuan, S.; Chen, Q.; Wang, J. Towards a Comprehensive Understanding of the Reaction Mechanisms Between Defective MoS2 and Thiol Molecules.

Angewandte Chemie International Edition **2017**, *56*, 10501-10505.
(152) Wang, X.; Wang, P.; Wang, J.; Hu, W.; Zhou, X.; Guo, N.; Huang, H.; Sun, S.; Shen, H.; Lin, T.; Tang, M.; Liao, L.; Jiang, A.; Sun, J.; Meng, X.; Chen, X.; Lu, W.; Chu, J. Ultrasensitive and Broadband MoS2 Photodetector Driven by Ferroelectrics. *Advanced Materials* **2015**, *27*, 6575-6581.
(153) Lei, B.; Hu, Z.; Xiang, D.; Wang, J.; Eda, G.; Han, C.; Chen, W. Significantly enhanced optoelectronic performance of tungsten diselenide phototransistor via surface functionalization. *Nano Research* **2017**, *10*, 1282-1291.
(154) Huang, Y.; Zheng, W.; Qiu, Y.; Hu, P. Effects of Organic Molecules with Different Structures and Absorption Bandwidth on Modulating Photoresponse of MoS2 Photodetector. *ACS Applied Materials & Interfaces* **2016**, *8*, 23362-23370.
(155) Pak, J.; Jang, J.; Cho, K.; Kim, T.-Y.; Kim, J.-K.; Song, Y.; Hong, W.-K.; Min, M.; Lee, H.; Lee, T. Enhancement of photodetection characteristics of MoS2 field effect transistors using surface treatment with copper phthalocyanine. *Nanoscale* **2015**, *7*, 18780-18788.
(156) Yu, S. H.; Lee, Y.; Jang, S. K.; Kang, J.; Jeon, J.; Lee, C.; Lee, J. Y.; Kim, H.; Hwang, E.; Lee, S.; Cho, J. H. Dye-Sensitized MoS2 Photodetector with Enhanced Spectral Photoresponse. *ACS Nano* **2014**, *8*, 8285-8291.
(157) Mutz, N.; Park, S.; Schultz, T.; Sadofev, S.; Dalgleish, S.; Reissig, L.; Koch, N.; List-Kratochvil, E. J. W.; Blumstengel, S. Excited-State Charge Transfer Enabling MoS2/Phthalocyanine Photodetectors with Extended Spectral Sensitivity. *The Journal of Physical Chemistry C* **2020**, *124*, 2837-2843.
(158) Cusati, T.; Fiori, G.; Gahoi, A.; Passi, V.; Lemme, M. C.; Fortunelli, A.; Iannaccone, G. Electrical properties of graphene-metal contacts. *Scientific Reports* **2017**, *7*, 5109.
(159) Ko, J. S.; Shin, D. H.; Lee, W. J.; Jang, C. W.; Kim, S.; Choi, S.-H. All-two-dimensional semitransparent and flexible photodetectors employing graphene/MoS2/graphene vertical heterostructures. *Journal of Alloys and Compounds* **2021**, *864*, 158118.
(160) Li, P.; Yuan, K.; Lin, D.-Y.; Xu, X.; Wang, Y.; Wan, Y.; Yu, H.; Zhang, K.; Ye, Y.; Dai, L. A mixed-dimensional light-emitting diode based on a p-MoS2 nanosheet and an n-CdSe nanowire. *Nanoscale* **2017**, *9*, 18175-18179.
(161) Kim, C.; Nguyen, T. P.; Le, Q. V.; Jeon, J.-M.; Jang, H. W.; Kim, S. Y. Performances of Liquid-Exfoliated Transition Metal Dichalcogenides as Hole Injection Layers in Organic Light-Emitting Diodes. *Advanced Functional Materials* **2015**, *25*, 4512-4519.
(162) Guo, K.; Si, C.; Han, C.; Pan, S.; Chen, G.; Zheng, Y.; Zhu, W.; Zhang, J.; Sun, C.; Wei, B. High-performance flexible inverted organic light-emitting diodes by exploiting MoS2

nanopillar arrays as electron-injecting and light-coupling layers. *Nanoscale* **2017**, *9*, 14602-14611.

(163) Choi, M.; Bae, S.-R.; Hu, L.; Hoang, A. T.; Kim, S. Y.; Ahn, J.-H. Full-color active-matrix organic light-emitting diode display on human skin based on a large-area MoS2 backplane. *Science Advances* **2020**, *6*, eabb5898.

(164) Park, M.; Nguyen, T. P.; Choi, K. S.; Park, J.; Ozturk, A.; Kim, S. Y. MoS2-nanosheet/graphene-oxide composite hole injection layer in organic light-emitting diodes. *Electronic Materials Letters* **2017**, *13*, 344-350.

(165) Choudhary, R. B.; Mandal, G. MoS2 decorated with graphene and polyaniline nanocomposite as an electron transport layer for OLED applications. *Journal of Materials Science: Materials in Electronics* **2020**, *31*, 1302-1316.

(166) Hummers, W. S.; Offeman, R. E. Preparation of Graphitic Oxide. *Journal of the American Chemical Society* **1958**, *80*, 1339-1339.

(167) Zhang, H.; Pan, J.; Ghimire, S.; Bork, M. A.; Riccitelli, M. M.; McMillin, D. R.; Choi, J. H. Regeneration of Light-Harvesting Complexes via Dynamic Replacement of Photodegraded Chromophores. *ACS Applied Materials & Interfaces* **2015**, *7*, 7833-7837.

(168) Zhang, H.; Baker, B. A.; Cha, T.-G.; Sauffer, M. D.; Wu, Y.; Hinkson, N.; Bork, M. A.; McShane, C. M.; Choi, K.-S.; McMillin, D. R.; Choi, J. H. DNA Oligonucleotide Templated Nanohybrids Using Electronic Type Sorted Carbon Nanotubes for Light Harvesting. *Advanced Materials* **2012**, *24*, 5447-5451.

(169) Zhang, H.; Bork, M. A.; Riedy, K. J.; McMillin, D. R.; Choi, J. H. Understanding Photophysical Interactions of Semiconducting Carbon Nanotubes with Porphyrin Chromophores. *The Journal of Physical Chemistry C* **2014**, *118*, 11612-11619.

(170) Baker, B. A.; Zhang, H.; Cha, T. G.; Choi, J. H. 9 - Carbon nanotube solar cells. In *Carbon Nanotubes and Graphene for Photonic Applications*, Yamashita, S., Saito, Y., Choi, J. H. Eds.; Woodhead Publishing, 2013; pp 241-269.

(171) Fontana, M.; Deppe, T.; Boyd, A. K.; Rinzan, M.; Liu, A. Y.; Paranjape, M.; Barbara, P. Electron-hole transport and photovoltaic effect in gated MoS2 Schottky junctions. *Scientific Reports* **2013**, *3*, 1634.

(172) Kesavan, A. V.; Rao, A. D.; Ramamurthy, P. C. Optical and electronic property tailoring by MoS2-polymer hybrid solar cell. *Organic Electronics* **2017**, *48*, 138-146.

(173) Ahmad, R.; Srivastava, R.; Yadav, S.; Chand, S.; Sapra, S. Functionalized 2D-MoS2-Incorporated Polymer Ternary Solar Cells: Role of Nanosheet-Induced Long-Range Ordering of Polymer Chains on Charge Transport. *ACS Applied Materials & Interfaces* **2017**, *9*, 34111-

34121.
(174) Lin, Y.; Adilbekova, B.; Firdaus, Y.; Yengel, E.; Faber, H.; Sajjad, M.; Zheng, X.; Yarali, E.; Seitkhan, A.; Bakr, O. M.; El-Labban, A.; Schwingenschlögl, U.; Tung, V.; McCulloch, I.; Laquai, F.; Anthopoulos, T. D. 17% Efficient Organic Solar Cells Based on Liquid Exfoliated WS2 as a Replacement for PEDOT:PSS. *Advanced Materials* **2019**, *31*, 1902965.
(175) Ieong, M.; Doris, B.; Kedzierski, J.; Rim, K.; Yang, M. Silicon Device Scaling to the Sub-10-nm Regime. *Science* **2004**, *306*, 2057-2060.
(176) Ishii, T.; Osabe, T.; Mine, T.; Sano, T.; Atwood, B.; Yano, K. A poly-silicon TFT with a sub-5-nm thick channel for low-power gain cell memory in mobile applications. *IEEE Transactions on Electron Devices* **2004**, *51*, 1805-1810.
(177) Seabaugh, A. The Tunneling Transistor. *IEEE Spectrum* **2013**, *50*, 35-62.
(178) Qiu, H.; Zhao, Y.; Liu, Z.; Herder, M.; Hecht, S.; Samorì, P. Modulating the Charge Transport in 2D Semiconductors via Energy-Level Phototuning. *Advanced Materials* **2019**, *31*, 1903402.
(179) Zhao, Y.; Bertolazzi, S.; Maglione, M. S.; Rovira, C.; Mas-Torrent, M.; Samorì, P. Molecular Approach to Electrochemically Switchable Monolayer MoS2 Transistors. *Advanced Materials* **2020**, *32*, 2000740.
(180) Carroli, M.; Dixon, A. G.; Herder, M.; Pavlica, E.; Hecht, S.; Bratina, G.; Orgiu, E.; Samorì, P. Multiresponsive Nonvolatile Memories Based on Optically Switchable Ferroelectric Organic Field-Effect Transistors. *Advanced Materials* **2021**, *33*, 2007965.
(181) Wang, Y.; Iglesias, D.; Gali, S. M.; Beljonne, D.; Samorì, P. Light-Programmable Logic-in-Memory in 2D Semiconductors Enabled by Supramolecular Functionalization: Photoresponsive Collective Effect of Aligned Molecular Dipoles. *ACS Nano* **2021**, *15*, 13732-13741.
(182) Lu, Y.; Yao, X.; Yin, J.; Peng, G.; Cui, P.; Xu, X. MoS2 nanoflowers consisting of nanosheets with a controllable interlayer distance as high-performance lithium ion battery anodes. *RSC Advances* **2015**, *5*, 7938-7943.
(183) Jaramillo, T. F.; Jørgensen, K. P.; Bonde, J.; Nielsen, J. H.; Horch, S.; Chorkendorff, I. Identification of Active Edge Sites for Electrochemical H2 Evolution from MoS2 Nanocatalysts. *Science* **2007**, *317*, 100-102.
(184) Joseph, N.; Shafi, P. M.; Bose, A. C. Recent Advances in 2D-MoS2 and its Composite Nanostructures for Supercapacitor Electrode Application. *Energy & Fuels* **2020**, *34*, 6558-6597.
(185) Wei, S.; Zhou, R.; Wang, G. Enhanced Electrochemical Performance of Self-Assembled

Nanoflowers of MoS2 Nanosheets as Supercapacitor Electrode Materials. *ACS Omega* **2019**, *4*, 15780-15788.

(186) Li, Z.; Ma, J.; Zhou, Y.; Yin, Z.; Tang, Y.; Ma, Y.; Wang, D. Synthesis of sulfur-rich MoS2 nanoflowers for enhanced hydrogen evolution reaction performance. *Electrochimica Acta* **2018**, *283*, 306-312.

(187) Acerce, M.; Voiry, D.; Chhowalla, M. Metallic 1T phase MoS2 nanosheets as supercapacitor electrode materials. *Nature Nanotechnology* **2015**, *10*, 313-318.

(188) Houpt, D.; Ji, J.; Yang, D.; Choi, J. H. High-Performance Supercapacitor Electrodes Based on Composites of MoS2 Nanosheets, Carbon Nanotubes, and ZIF-8 Metal–Organic Framework Nanoparticles. *ACS Applied Nano Materials* **2022**, *5*, 1491-1499.

(189) Choudhary, N.; Islam, M. A.; Kim, J. H.; Ko, T.-J.; Schropp, A.; Hurtado, L.; Weitzman, D.; Zhai, L.; Jung, Y. Two-dimensional transition metal dichalcogenide hybrid materials for energy applications. *Nano Today* **2018**, *19*, 16-40.

(190) Ren, Y.; Yang, X.; Zhou, L.; Mao, J.-Y.; Han, S.-T.; Zhou, Y. Recent Advances in Ambipolar Transistors for Functional Applications. *Advanced Functional Materials* **2019**, *29*, 1902105.

(191) Zhang, S.; Song, X.; Liu, S.; Sun, F.; Liu, G.; Tan, Z. Template-assisted synthesized MoS2/polyaniline hollow microsphere electrode for high performance supercapacitors. *Electrochimica Acta* **2019**, *312*, 1-10.

(192) Zhang, R.; Liao, Y.; Ye, S.; Zhu, Z.; Qian, J. Novel ternary nanocomposites of MWCNTs/PANI/MoS2: preparation, characterization and enhanced electrochemical capacitance. *Royal Society Open Science* **2018**, *5*, 171365.

(193) Heydari, H.; Abdouss, M.; Mazinani, S.; Bazargan, A. M.; Fatemi, F. Electrochemical study of ternary polyaniline/MoS2−MnO2 for supercapacitor applications. *Journal of Energy Storage* **2021**, *40*, 102738.

(194) Majumder, M.; Choudhary, R. B.; Koiry, S. P.; Thakur, A. K.; Kumar, U. Gravimetric and volumetric capacitive performance of polyindole/carbon black/MoS2 hybrid electrode material for supercapacitor applications. *Electrochimica Acta* **2017**, *248*, 98-111.

(195) Chen, Y.; Bai, J.; Yang, D.; Sun, P.; Li, X. Excellent performance of flexible supercapacitor based on the ternary composites of reduced graphene oxide/molybdenum disulfide/poly (3,4-ethylenedioxythiophene). *Electrochimica Acta* **2020**, *330*, 135205.

(196) Chu, C.-W.; Sari, F. N. I.; Ke, J. C.-R.; Ting, J.-M. A novel ternary nanocomposite for improving the cycle life and capacitance of polypyrrole. *Applied Surface Science* **2018**, *462*, 526-539.

(197) Thiyagarajan, K.; Song, W.-J.; Park, H.; Selvaraj, V.; Moon, S.; Oh, J.; Kwak, M.-J.; Park, G.; Kong, M.; Pal, M.; Kwak, J.; Giri, A.; Jang, J.-H.; Park, S.; Jeong, U. Electroactive 1T-MoS2 Fluoroelastomer Ink for Intrinsically Stretchable Solid-State In-Plane Supercapacitors. *ACS Applied Materials & Interfaces* **2021**, *13*, 26870-26878.

(198) Wang, Z.; Yue, H. Y.; Yu, Z. M.; Yao, F.; Gao, X.; Guan, E. H.; Zhang, H. J.; Wang, W. Q.; Song, S. S. One-pot hydrothermal synthesis of MoSe2 nanosheets spheres-reduced graphene oxide composites and application for high-performance supercapacitor. *Journal of Materials Science: Materials in Electronics* **2019**, *30*, 8537-8545.

(199) Balasingam, S. K.; Lee, J. S.; Jun, Y. Molybdenum diselenide/reduced graphene oxide based hybrid nanosheets for supercapacitor applications. *Dalton Transactions* **2016**, *45*, 9646-9653.

(200) Kim, M.; Kim, Y. K.; Kim, J.; Cho, S.; Lee, G.; Jang, J. Fabrication of a polyaniline/MoS2 nanocomposite using self-stabilized dispersion polymerization for supercapacitors with high energy density. *RSC Advances* **2016**, *6*, 27460-27465.

(201) Shi, Y.; Peng, L.; Ding, Y.; Zhao, Y.; Yu, G. Nanostructured conductive polymers for advanced energy storage. *Chemical Society Reviews* **2015**, *44*, 6684-6696.

(202) Yue, L.; Wang, X.; Sun, T.; Liu, H.; Li, Q.; Wu, N.; Guo, H.; Yang, W. Ni-MOF coating MoS2 structures by hydrothermal intercalation as high-performance electrodes for asymmetric supercapacitors. *Chemical Engineering Journal* **2019**, *375*, 121959.

(203) Huang, S.; Shi, X.-R.; Sun, C.; Duan, Z.; Ma, P.; Xu, S. The Application of Metal–Organic Frameworks and Their Derivatives for Supercapacitors. *Nanomaterials* **2020**, *10*, 2268.

(204) Wang, S.; Zhu, J.; Shao, Y.; Li, W.; Wu, Y.; Zhang, L.; Hao, X. Three-Dimensional MoS2@CNT/RGO Network Composites for High-Performance Flexible Supercapacitors. *Chemistry – A European Journal* **2017**, *23*, 3438-3446.

(205) Govindan, R.; Hong, X.-J.; Sathishkumar, P.; Cai, Y.-P.; Gu, F. L. Construction of metal-organic framework-derived CeO2/C integrated MoS2 hybrid for high-performance asymmetric supercapacitor. *Electrochimica Acta* **2020**, *353*, 136502.

(206) Xu, X.; Chu, H.; Zhang, Z.; Dong, P.; Baines, R.; Ajayan, P. M.; Shen, J.; Ye, M. Integrated Energy Aerogel of N,S-rGO/WSe2/NiFe-LDH for Both Energy Conversion and Storage. *ACS Applied Materials & Interfaces* **2017**, *9*, 32756-32766.

(207) Li, X.; Zhang, C.; Xin, S.; Yang, Z.; Li, Y.; Zhang, D.; Yao, P. Facile Synthesis of MoS2/Reduced Graphene Oxide@Polyaniline for High-Performance Supercapacitors. *ACS Applied Materials & Interfaces* **2016**, *8*, 21373-21380.

(208) Naz, R.; Liu, Q.; Abbas, W.; Imtiaz, M.; Zada, I.; Ahmad, J.; Li, T.; Gu, J. One-Pot

Hydrothermal Synthesis of Ternary 1T-MoS2/Hexa-WO3/Graphene Composites for High-Performance Supercapacitors. *Chemistry – A European Journal* **2019**, *25*, 16054-16062.

(209) Voiry, D.; Yang, J.; Chhowalla, M. Recent Strategies for Improving the Catalytic Activity of 2D TMD Nanosheets Toward the Hydrogen Evolution Reaction. *Advanced Materials* **2016**, *28*, 6197-6206.

(210) Nguyen, V.-H.; Nguyen, T. P.; Le, T.-H.; Vo, D.-V. N.; Nguyen, D. L.; Trinh, Q. T.; Kim, I. T.; Le, Q. V. Recent advances in two-dimensional transition metal dichalcogenides as photoelectrocatalyst for hydrogen evolution reaction. *Journal of Chemical Technology & Biotechnology* **2020**, *95*, 2597-2607.

(211) Wu, M.-h.; Li, L.; Liu, N.; Wang, D.-j.; Xue, Y.-c.; Tang, L. Molybdenum disulfide (MoS2) as a co-catalyst for photocatalytic degradation of organic contaminants: A review. *Process Safety and Environmental Protection* **2018**, *118*, 40-58.

(212) Singh, S.; Modak, A.; Pant, K. K.; Sinhamahapatra, A.; Biswas, P. MoS2–Nanosheets-Based Catalysts for Photocatalytic CO2 Reduction: A Review. *ACS Applied Nano Materials* **2021**, *4*, 8644-8667.

(213) Mohana Roopan, S.; Khan, M. A. MoS2 based ternary composites: review on heterogeneous materials as catalyst for photocatalytic degradation. *Catalysis Reviews* **2021**, 1-74.

(214) Dubouis, N.; Grimaud, A. The hydrogen evolution reaction: from material to interfacial descriptors. *Chemical Science* **2019**, *10*, 9165-9181.

(215) McKone, J. R.; Warren, E. L.; Bierman, M. J.; Boettcher, S. W.; Brunschwig, B. S.; Lewis, N. S.; Gray, H. B. Evaluation of Pt, Ni, and Ni–Mo electrocatalysts for hydrogen evolution on crystalline Si electrodes. *Energy & Environmental Science* **2011**, *4*, 3573-3583.

(216) Sajedi-Moghaddam, A.; Saievar-Iranizad, E.; Pumera, M. Two-dimensional transition metal dichalcogenide/conducting polymer composites: synthesis and applications. *Nanoscale* **2017**, *9*, 8052-8065.

(217) Wang, J.; Liu, J.; Zhang, B.; Ji, X.; Xu, K.; Chen, C.; Miao, L.; Jiang, J. The mechanism of hydrogen adsorption on transition metal dichalcogenides as hydrogen evolution reaction catalyst. *Physical Chemistry Chemical Physics* **2017**, *19*, 10125-10132.

(218) Guo, W.; Le, Q. V.; Hasani, A.; Lee, T. H.; Jang, H. W.; Luo, Z.; Kim, S. Y. MoSe2-GO/rGO Composite Catalyst for Hydrogen Evolution Reaction. *Polymers* **2018**, *10*, 1309.

(219) Salehi, S.; Molaei, M.; Karimipour, M. Mo-rich rGO–2H–MoSe2 nanocomposites with novel crystal growth plane of (106) for high hydrogen evolution reaction activity. *Materials Science in Semiconductor Processing* **2022**, *142*, 106475.

(220) Hou, Y.; Pang, H.; Xin, J.; Ma, H.; Li, B.; Wang, X.; Tan, L. Multi-Interface-Modulated CoS2@MoS2 Nanoarrays Derived by Predesigned Germanomolybdate Polymer Showing Ultrahighly Electrocatalytic Activity for Hydrogen Evolution Reaction in Wide pH Range. *Advanced Materials Interfaces* **2020**, *7*, 2000780.

(221) Ma, B.; Guan, P.-Y.; Li, Q.-Y.; Zhang, M.; Zang, S.-Q. MOF-Derived Flower-like MoS2@TiO2 Nanohybrids with Enhanced Activity for Hydrogen Evolution. *ACS Applied Materials & Interfaces* **2016**, *8*, 26794-26800.

(222) Wang, T.; Zhuo, J.; Du, K.; Chen, B.; Zhu, Z.; Shao, Y.; Li, M. Electrochemically Fabricated Polypyrrole and MoSx Copolymer Films as a Highly Active Hydrogen Evolution Electrocatalyst. *Advanced Materials* **2014**, *26*, 3761-3766.

(223) Tong, J.; Li, Q.; Li, W.; Wang, W.; Ma, W.; Su, B.; Bo, L. MoS2 Thin Sheet Growing on Nitrogen Self-Doped Mesoporous Graphic Carbon Derived from ZIF-8 with Highly Electrocatalytic Performance on Hydrogen Evolution Reaction. *ACS Sustainable Chemistry & Engineering* **2017**, *5*, 10240-10247.

(224) Nguyen, T. N.; Kampouri, S.; Valizadeh, B.; Luo, W.; Ongari, D.; Planes, O. M.; Züttel, A.; Smit, B.; Stylianou, K. C. Photocatalytic Hydrogen Generation from a Visible-Light-Responsive Metal–Organic Framework System: Stability versus Activity of Molybdenum Sulfide Cocatalysts. *ACS Applied Materials & Interfaces* **2018**, *10*, 30035-30039.

(225) Choi, J.; Amaranatha Reddy, D.; Han, N. S.; Jeong, S.; Hong, S.; Praveen Kumar, D.; Song, J. K.; Kim, T. K. Modulation of charge carrier pathways in CdS nanospheres by integrating MoS2 and Ni2P for improved migration and separation toward enhanced photocatalytic hydrogen evolution. *Catalysis Science & Technology* **2017**, *7*, 641-649.

(226) Kannichankandy, D.; Pataniya, P. M.; Sumesh, C. K.; Solanki, G. K.; Pathak, V. M. WSe2-PANI nanohybrid structure as efficient electrocatalyst for photo-enhanced hydrogen evolution reaction. *Journal of Alloys and Compounds* **2021**, *876*, 160179.

(227) Gao, M.-Y.; Li, C.-C.; Tang, H.-L.; Sun, X.-J.; Dong, H.; Zhang, F.-M. Boosting visible-light-driven hydrogen evolution of covalent organic frameworks through compositing with MoS2: a promising candidate for noble-metal-free photocatalysts. *Journal of Materials Chemistry A* **2019**, *7*, 20193-20200.

(228) Zang, S.; Zhang, G.; Lan, Z.-A.; Zheng, D.; Wang, X. Enhancement of photocatalytic H2 evolution on pyrene-based polymer promoted by MoS2 and visible light. *Applied Catalysis B: Environmental* **2019**, *251*, 102-111.

(229) Ma, B.; Chen, T.-T.; Li, Q.-Y.; Qin, H.-N.; Dong, X.-Y.; Zang, S.-Q. Bimetal–Organic-Framework-Derived Nanohybrids Cu0.9Co2.1S4@MoS2 for High-Performance Visible-

Light-Catalytic Hydrogen Evolution Reaction. *ACS Applied Energy Materials* **2019**, *2*, 1134-1148.

(230) Tong, R.; Ng, K. W.; Wang, X.; Wang, S.; Wang, X.; Pan, H. Two-dimensional materials as novel co-catalysts for efficient solar-driven hydrogen production. *Journal of Materials Chemistry A* **2020**, *8*, 23202-23230.

(231) Hasani, A.; Tekalgne, M.; Le, Q. V.; Jang, H. W.; Kim, S. Y. Two-dimensional materials as catalysts for solar fuels: hydrogen evolution reaction and CO2 reduction. *Journal of Materials Chemistry A* **2019**, *7*, 430-454.

(232) Yuan, L.; Wang, T.; Zhu, T.; Zhou, M.; Huang, L. Exciton Dynamics, Transport, and Annihilation in Atomically Thin Two-Dimensional Semiconductors. *The Journal of Physical Chemistry Letters* **2017**, *8*, 3371-3379.

(233) Kozawa, D.; Kumar, R.; Carvalho, A.; Kumar Amara, K.; Zhao, W.; Wang, S.; Toh, M.; Ribeiro, R. M.; Castro Neto, A. H.; Matsuda, K.; Eda, G. Photocarrier relaxation pathway in two-dimensional semiconducting transition metal dichalcogenides. *Nature Communications* **2014**, *5*, 4543.

(234) Chernikov, A.; Ruppert, C.; Hill, H. M.; Rigosi, A. F.; Heinz, T. F. Population inversion and giant bandgap renormalization in atomically thin WS2 layers. *Nature Photonics* **2015**, *9*, 466-470.

(235) Moody, G.; Schaibley, J.; Xu, X. Exciton dynamics in monolayer transition metal dichalcogenides [Invited]. *J. Opt. Soc. Am. B* **2016**, *33*, C39-C49.

(236) Yu, Y.; Yu, Y.; Cai, Y.; Li, W.; Gurarslan, A.; Peelaers, H.; Aspnes, D. E.; Van de Walle, C. G.; Nguyen, N. V.; Zhang, Y.-W.; Cao, L. Exciton-dominated Dielectric Function of Atomically Thin MoS2 Films. *Scientific Reports* **2015**, *5*, 16996.

(237) Xiao, J.; Zhao, M.; Wang, Y.; Zhang, X. Excitons in atomically thin 2D semiconductors and their applications. *Nanophotonics* **2017**, *6*, 1309-1328.

(238) Li, W.; Lu, X.; Dubey, S.; Devenica, L.; Srivastava, A. Dipolar interactions between localized interlayer excitons in van der Waals heterostructures. *Nature Materials* **2020**, *19*, 624-629.

(239) Wang, J.; Ardelean, J.; Bai, Y.; Steinhoff, A.; Florian, M.; Jahnke, F.; Xu, X.; Kira, M.; Hone, J.; Zhu, X.-Y. Optical generation of high carrier densities in 2D semiconductor heterobilayers. *Science Advances* **2019**, *5*, eaax0145.

(240) Novoselov, K. S.; Mishchenko, A.; Carvalho, A.; Castro Neto, A. H. 2D materials and van der Waals heterostructures. *Science* **2016**, *353*, aac9439.

(241) Kishimoto, Y.; Abe, J. A Fast Photochromic Molecule That Colors Only under UV Light.

Journal of the American Chemical Society **2009**, *131*, 4227-4229.
(242) Zhang, Y.-M.; Wang, X.; Zhang, W.; Li, W.; Fang, X.; Yang, B.; Li, M.; Zhang, S. X.-A. A single-molecule multicolor electrochromic device generated through medium engineering. *Light: Science & Applications* **2015**, *4*, e249-e249.
(243) Itkis, M. E.; Chi, X.; Cordes, A. W.; Haddon, R. C. Magneto-Opto-Electronic Bistability in a Phenalenyl-Based Neutral Radical. *Science* **2002**, *296*, 1443-1445.
(244) Choudhary, N.; Park, J.; Hwang, J. Y.; Chung, H.-S.; Dumas, K. H.; Khondaker, S. I.; Choi, W.; Jung, Y. Centimeter Scale Patterned Growth of Vertically Stacked Few Layer Only 2D MoS2/WS2 van der Waals Heterostructure. *Scientific Reports* **2016**, *6*, 25456.
(245) Hu, Y.; Zeng, X.; Ren, T.; Xiao, Y.; Zeng, Y.; Wang, W.; Guo, Z.; Jin, W.; Wang, S.; Lu, J.; Zeng, Y. One-step growth of centimeter-scale doped multilayer MoS2 films by pulsed laser-induced synthesis. *Journal of Materials Chemistry C* **2020**, *8*, 6900-6905.
(246) Seo, S.; Kim, S.; Choi, H.; Lee, J.; Yoon, H.; Piao, G.; Park, J.-C.; Jung, Y.; Song, J.; Jeong, S. Y.; Park, H.; Lee, S. Direct In Situ Growth of Centimeter-Scale Multi-Heterojunction MoS2/WS2/WSe2 Thin-Film Catalyst for Photo-Electrochemical Hydrogen Evolution. *Advanced Science* **2019**, *6*, 1900301.
(247) Qiu, X.; Wang, Y.; Jiang, Y. Dopants and grain boundary effects in monolayer MoS2: a first-principles study. *Physical Chemistry Chemical Physics* **2021**, *23*, 11937-11943.
(248) Huang, Y. L.; Chen, Y.; Zhang, W.; Quek, S. Y.; Chen, C.-H.; Li, L.-J.; Hsu, W.-T.; Chang, W.-H.; Zheng, Y. J.; Chen, W.; Wee, A. T. S. Bandgap tunability at single-layer molybdenum disulphide grain boundaries. *Nature Communications* **2015**, *6*, 6298.
(249) Poonam; Sharma, K.; Arora, A.; Tripathi, S. K. Review of supercapacitors: Materials and devices. *Journal of Energy Storage* **2019**, *21*, 801-825.
(250) Xu, Y.; Lu, W.; Xu, G.; Chou, T.-W. Structural supercapacitor composites: A review. *Composites Science and Technology* **2021**, *204*, 108636.
(251) Najib, S.; Erdem, E. Current progress achieved in novel materials for supercapacitor electrodes: mini review. *Nanoscale Advances* **2019**, *1*, 2817-2827.
(252) Ahmed, S. I.; Radhakrishnan, S.; Nair, B. B.; Thiruvengadathan, R. Efficient hyperparameter-tuned machine learning approach for estimation of supercapacitor performance attributes. *Journal of Physics Communications* **2021**, *5*, 115011.
(253) Su, H.; Lian, C.; Liu, J.; Liu, H. Machine learning models for solvent effects on electric double layer capacitance. *Chemical Engineering Science* **2019**, *202*, 186-193.
(254) Zhu, S.; Li, J.; Ma, L.; He, C.; Liu, E.; He, F.; Shi, C.; Zhao, N. Artificial neural network enabled capacitance prediction for carbon-based supercapacitors. *Materials Letters* **2018**, *233*,

294-297.
(255) Tabor, D. P.; Roch, L. M.; Saikin, S. K.; Kreisbeck, C.; Sheberla, D.; Montoya, J. H.; Dwaraknath, S.; Aykol, M.; Ortiz, C.; Tribukait, H.; Amador-Bedolla, C.; Brabec, C. J.; Maruyama, B.; Persson, K. A.; Aspuru-Guzik, A. Accelerating the discovery of materials for clean energy in the era of smart automation. *Nature Reviews Materials* **2018**, *3*, 5-20.
(256) Patra, T. K.; Zhang, F.; Schulman, D. S.; Chan, H.; Cherukara, M. J.; Terrones, M.; Das, S.; Narayanan, B.; Sankaranarayanan, S. K. R. S. Defect Dynamics in 2-D MoS2 Probed by Using Machine Learning, Atomistic Simulations, and High-Resolution Microscopy. *ACS Nano* **2018**, *12*, 8006-8016.
(257) Novoselov, K. S.; Geim, A. K.; Morozov, S. V.; Jiang, D.; Zhang, Y.; Dubonos, S. V.; Grigorieva, I. V.; Firsov, A. A. Electric Field Effect in Atomically Thin Carbon Films. *Science* **2004**, *306*, 666-669.
(258) Konnerth, H.; Matsagar, B. M.; Chen, S. S.; Prechtl, M. H. G.; Shieh, F.-K.; Wu, K. C. W. Metal-organic framework (MOF)-derived catalysts for fine chemical production. *Coordination Chemistry Reviews* **2020**, *416*, 213319.

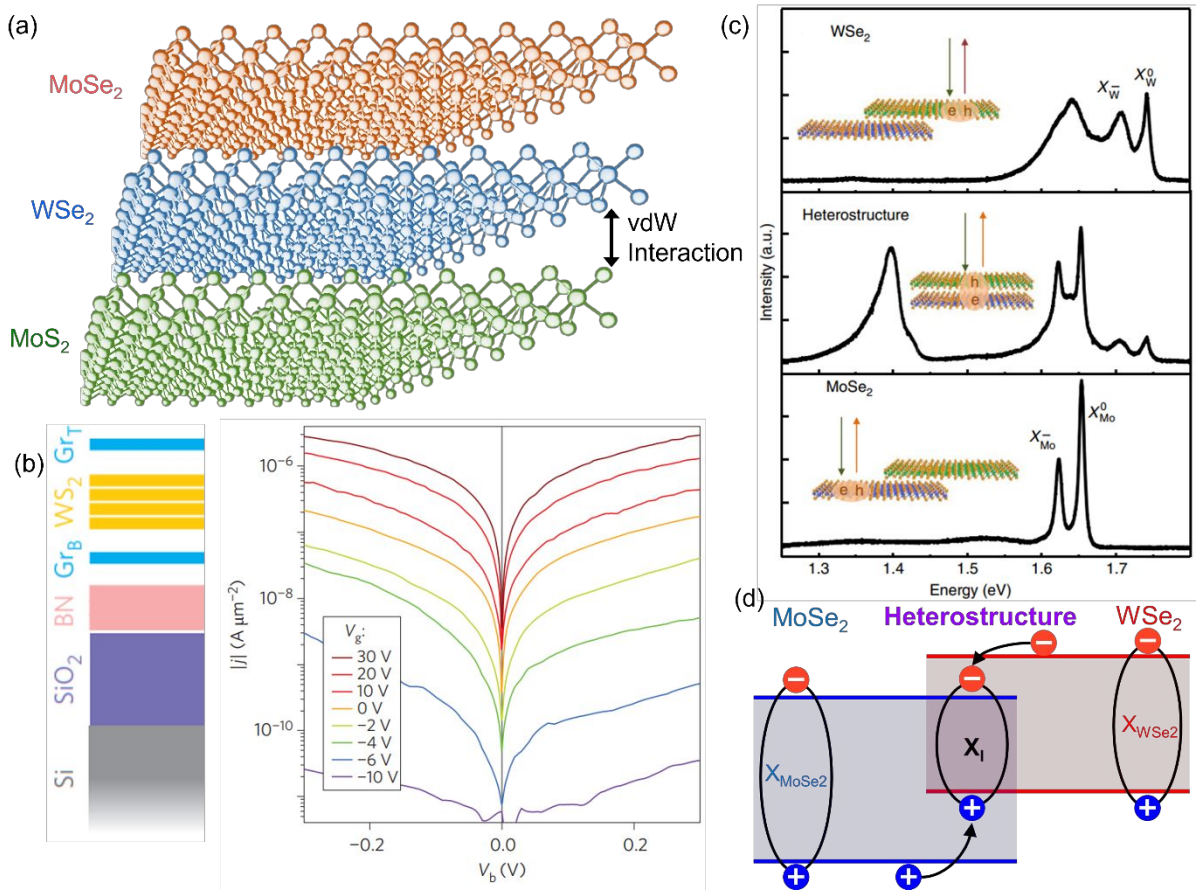

Figure 1. van der Waals (vdW) heterostructures. (a) Schematic illustration of vdW heterolayers that are built by stacking various 2D TMD layers. The vdW heterostructures exhibit extraordinary properties that cannot be achieved with individual 2D layers. (b) Room-temperature charge transport measurements in a BN/graphene/WS_2/graphene heterostructure,[69] which shows a high on/off ratio of ~10^6. (c) Intralayer PL spectra of $MoSe_2$ (top) and WSe_2 (bottom). The spectrum of $MoSe_2$/WSe_2 showing both intralayer and interlayer emissions (mid).[70] (d) Schematic of interlayer exciton (IX) formation in a staggered band alignment where interlayer charge transfer is facilitated. The IX has a distinct energy level compared to intralayer MoS_2 (X_{MoSe2}) and WSe_2 (X_{WSe2}) excitons.[71] Figures 1b, 1c, and 1d have been reproduced from refs. 69, 70, and 71, respectively, with permission from Springer Nature: ref. 69, copyright 2013; ref. 70, copyright 2015; and ref. 71, copyright 2019.

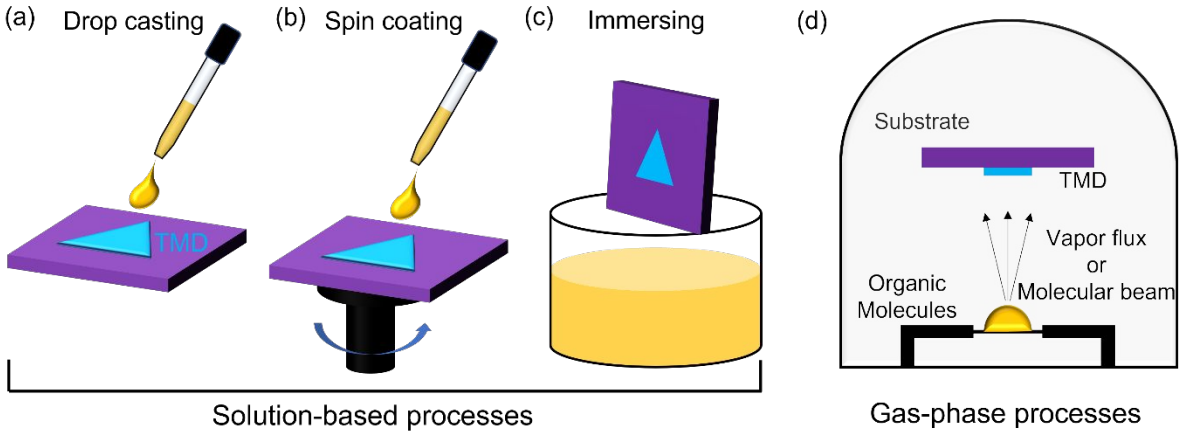

Figure 2. Schematics of preparation methods for TMD/organic hybrid structures. Organic molecules may be deposited on TMD flakes by solution or gas phase processes. The solution processes include (a) drop-casting, (b) spin coating, and (c) immersion. The molecules in the solutions can bind with TMDs via vdW, covalent, or electrostatic interactions and form uniform layers or self-patterned structures on TMDs. (d) The gas-phase deposition can be carried out in a temperature- and pressure-controlled chamber. In a low-pressure and high-temperature environment, the vaporized molecular flux builds molecular crystals on TMDs via vdW forces.

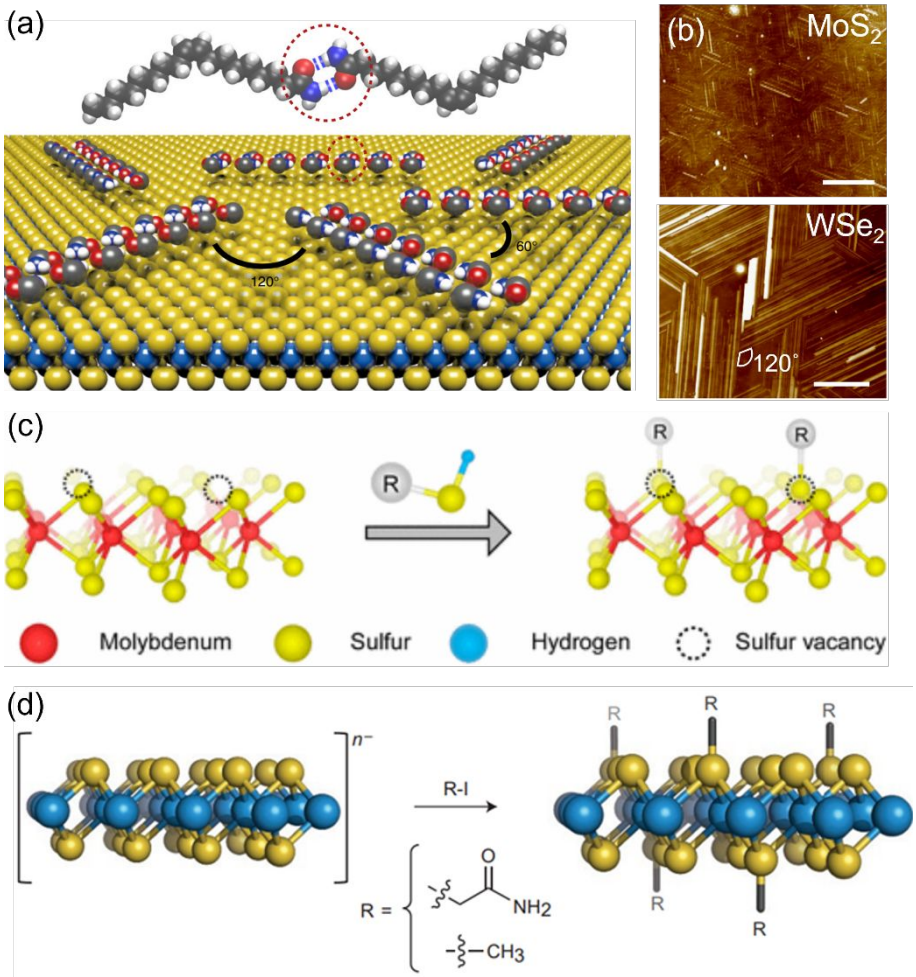

Figure 3. Molecular systems on TMDs via self-patterned, defects-mediated, and phase-assisted functionalization. (a) Schematic representation and (b) AFM images of self-patterned molecular assembly on TMDs, where organic molecules (oleamides) have a strong intermolecular interaction building a nanoribbon and align in zigzag directions.[96] (c) Defect-mediated organic functionalization. The molecules bearing thiol (-SH) groups fill the sulfur vacancies in TMDs.[104] (d) Phase-assisted decoration of organic molecules. The 1T-phase MoS_2 depicted by n^- in the diagram (indicating the electron-rich nature) shares excessive charges with organic halides and forms covalent bonds with the molecules.[109] Figures 3a-3b and 3d have been adapted from refs. 96 and 109, respectively, with permission from Springer Nature: ref. 96, copyright 2017 and ref. 109, copyright 2015. Figure 3c has been reproduced from ref. 104 with permission from the American Chemical Society, copyright 2017.

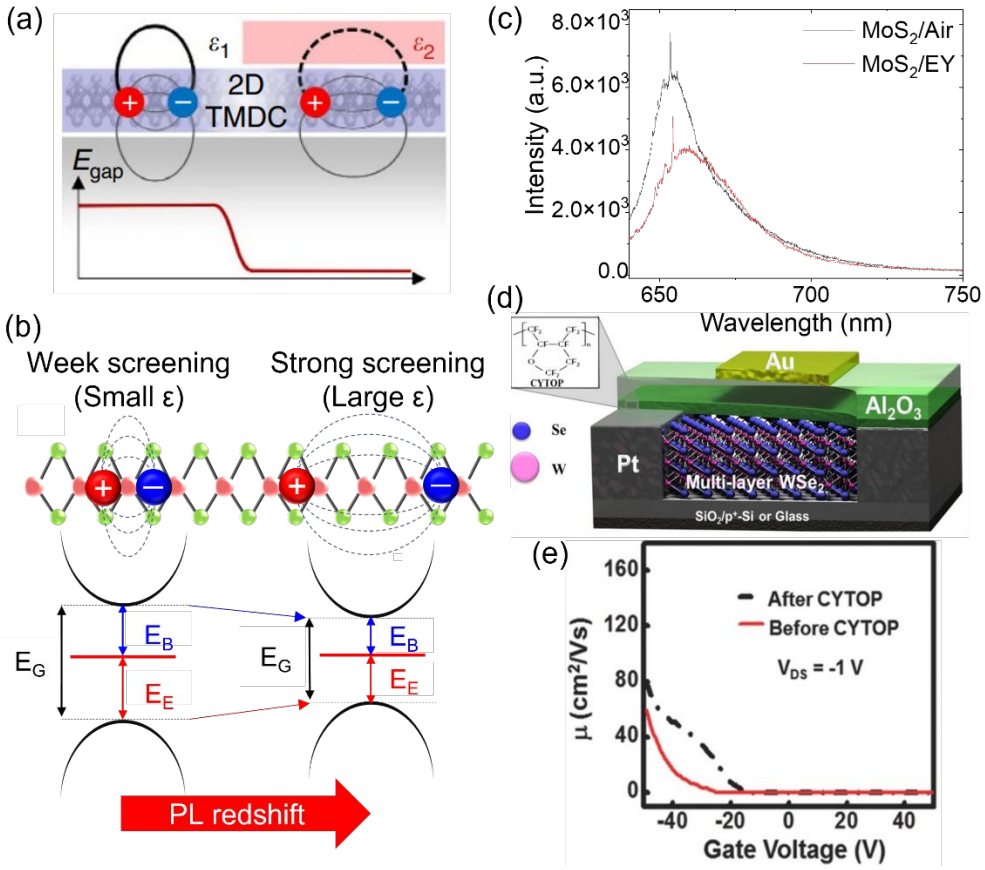

Figure 4. Dielectric screening in organic-integrated TMDs. (a) Schematic of a semiconducting 2D TMD partially encapsulated with a dielectric layer.[110] Due to the bandgap renormalization, the encapsulated region of the TMD layer may have a smaller bandgap than that without the dielectric layer. (b) Schematic of the emission energy modulation in an ultrathin TMD under different dielectric conditions. Here, E_E and E_B indicate the emission and the binding energies of an exciton, respectively. E_G is the bandgap energy. With the increased dielectric constant (ε), the emission energy may be reduced, thus resulting in the redshifted PL. (c) Emission spectra of MoS_2/eosin Y (EY) and MoS_2/air.[90] The organic layer with a greater dielectric screening leads to the redshifted emission peak by approximately ~6 nm. (d) Schematic of multilayer $MoSe_2$ FET with a dielectric layer of parylene molecules (CYTOP®).[112] (e) Conductivity measurements of $MoSe_2$ FET with and without the parylene layer. The hybrid device shows a greater mobility under negative gate voltage.[112] Figure 4a has been reproduced from ref. 110 with permission from Springer Nature, copyright 2017. Figures 4c and 4d-4e have been adapted from refs. 90 and 112, respectively, with permission from the American Chemical Society: ref. 90, copyright 2021 and ref.112, copyright 2014.

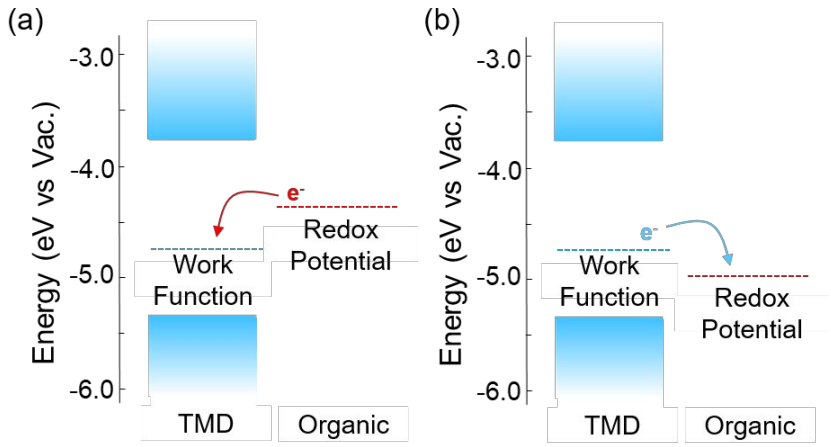

Figure 5. Dark-state doping at TMD/organic interfaces. Schematic representation of (a) n-doping and (b) p-doping on TMDs with the organic layers. The charge transfer characteristics are determined by the energy level difference between the work function of TMD and the redox potential of organic molecule.

Table 1. Various TMD-organic hybrid structures and their working mechanisms and applications.

TMD	Molecular system	Method/ interaction	Purpose	Mechanism	Demonstrated application	Ref.
MoS_2	4,4′-bipyridin (BP)	Dipping/ vdW	n-doping	Dark-state doping	FET	38
MoS_2	Benzyl viologen (BV)	Dipping/ vdW	n-doping	Dark-state doping	FET	125
WS_2	2,3,5,6-Tetrafluoro-7,7,8,8-tetracyanoquinodimethane (F_4TCNQ)	Drop casting/ vdW	p-doping	Dark-state doping	FET	127
MoS_2 and $MoSe_2$	Benzyl viologen (BV)	Dipping/ vdW	n-doping and preparing a lateral heterojunction	Dark-state doping	FET	88
MoS_2	2-mercaptoethylamine (MEA), 1H,1H,2H,2H-perfluorodecanethiol (FDT), and 2,2,2-trifluoroethanthiol (TFET)	Dipping/ covalent	Doping	Dark-state doping	FET	39
MoS_2 and WSe_2	Pt-phthalocyanine-4,4′,4″,4‴-tetrasulfonic acid tetrasodium salt (PtTsPc), Na_2TsPc, FeTsPc, CuTsPc, and fluororated-CuTsPc	Dipping/ vdW	Doping	Dark-state doping	FET	126
WSe_2 and MoS_2	Octadecyltrichlorosilane (OTS) and aminopropyltriethoxysilane (APTES)	Dipping/ vdW	Doping	Dark-state doping and dipolar interaction	FET	130

$MoTe_2$ and MoS_2	Octadecyltrichlorosilane (ODTS) and poly-L-lysine (PLL)	Dipping/ vdW	Doping	Dark-state doping and dipolar interaction	FET	131
MoS_2	3,5-difluoropyridine (3,5-FP), 3-fluoro-pyridine (3-FP), 2-fluoropyridine (2-FP), and 4-aminopyridine (4-AP) attached ZnPc	Dipping/ vdW	Doping	Dark-state doping and dipolar interaction	FET	133
MoS_2	Pentacene	Vapor deposition/ vdW	p-n heterojunction	Charge transfer supported by type II alignments	FET	135
MoS_2	Tetraene	Vapor deposition/ vdW	p-n heterojunction	Charge transfer supported by type II alignments	FET	136
WSe_2	Fluoropolymer	Spin-coating/ vdW	Gate-dielectric	Dielectric screening	FET	89
MoS_2	(3-mercaptopropyl)trimethoxysilane (MPS)	Dipping/ covalent	Defect healing	Disulfide bonding	FET	85
MoS_2	Bis(trifluoromethane) sulfonimide	Dipping	Defect healing	Disulfide bonding	FET	86
MoS_2	Decanethiol (DT) and perfluorodecanethiol (PFDT)	Vapor deposition/ covalent	Lowering the contact energy barrier	Disulfide bonding	FET	108
MoS_2	2-Iodoacetamide	Dipping/ covalent	Tuning the PL energy of MoS_2 and converting metallic MoS_2 to semiconducting phase	Charge transfer between metallic boundaries in $MoSe_2$ and 2-Iodoacetamide	FET	109

$MoSe_2$	Pentacene	Dry transfer/ vdW	Minimizing phonon scattering from Si substrate	Weak phonon interaction between $MoSe_2$ and pentacene	FET	112
$ReSe_2$	Triphenylphosphine (PPh3)	Spin-coating/ vdW	n-doping	Dark-state doping and dipolar interaction	Phototransistor	124
WSe_2	Cesium carbonate	Vapor deposition/ vdW	n-doping	Dark-state doping	Phototransistor	153
MoS_2	4-amino thiophenol (4ATP) and 4-nitro thiophenol (4NTP)	Dipping/ covalent bonding	Doping	Dark-state doping and dipolar interaction	Phototransistor	105
MoS_2	Zinc phthalocyanine (ZnPc)	Dipping/ vdW	Suppressing hole trapping	Photoinduced charge transfer	Phototransistor	137
MoS_2	Poly(vinylidene fluoride-trifluoroethylene) (P(VDF-TrFE))	Spin-coating/ vdW	Doping and exciton dissociation	Dipole-induced doping	Phototransistor	152
MoS_2	CuPc	Vapor deposition/ vdW	Doping and exciton dissociation	Photoinduced charge transfer	Phototransistor	155
MoS_2	R6G	Drop casting/ vdW	Doping and exciton dissociation	Photoinduced charge transfer	Phototransistor	156
MoS_2	H_2Pc	Vapor deposition/ vdW	Doping and exciton dissociation	Photoinduced charge transfer	Phototransistor	157
MoS_2	Methyl orange (MO), rhodamine 6G (R6G), and methylene blue (MB)	Drop casting/ vdW	Doping and exciton dissociation	Dark-state doping and photoinduced charge transfer	Phototransistor	154
MoS_2	Zn-, Fe-, Ga-, and H_2-	Dipping/	Amplification of photoinduced	Photoinduced charge transfer	Photovoltaics	77

	centered-protoporphyrin (PP)	vdW	current			
MoS_2	poly[[4,8-bis[(2-ethylhexyl)oxy]benzo[1,2-b:4,5-b']dithiophene-2,6-diyl][3-fluoro-2-[(2-ethylhexyl)carbonyl]thieno[3,4-b]thiophenediyl]] (PTB7), bis- [6,6]-Phenyl C71butyric acid methyl ester ($PC_{71}BM$)	Blending/ vdW	Charge injection and transport	Charge transfer supported by type II alignments	Photovoltaics	172, 204
MoS_2	$PC_{71}BM$ and Poly[[4,8-bis[(2-ethylhexyl)oxy]benzo[1,2-b:4,5-b']dithiophene-2,6-diyl][3-fluoro-2-[(2-ethylhexyl)carbonyl]thieno[3,4-b]thiophenediyl]] (PTB7), pol(3-hexylthiophene-2,5-diyl) (P3HT)	Blending/ vdW	Charge injection and transport	Charge transfer supported by type II alignments	Photovoltaics	173
MoS_2	Poly[[4,8-bis[5-(2-ethylhexyl)-4-fluoro-2-thienyl]benzo[1,2-b:4,5-b′]dithiophene-2,6-diyl]-2,5-thiophenediyl[5,7-	Spin-coating/ vdW	Hole injection and transport	Charge transfer supported by type II alignments	Photovoltaics	174

	bis(2-ethylhexyl)-4,8-dioxo-4H,8H-benzo[1,2-c:4,5-c′]dithiophene-1,3-diyl]-2,5-thiophenediyl] (PBDB-T-2F), thieno-thienopyrrolo-thienothienoindole (Y6), and $PC_{71}BM$					
MoS_2, WS_2, and TaS_2	Poly(3,4-ethylenedioxythiophene) polystyrene sulfonate (PEDOT:PSS), N , N′-Di(1-naphthyl)- N , N′-diphenyl-(1,1′-biphenyl)-4,4′-diamine (NPB), tris-(8-hydroxyquinoline)aluminum (Alq_3), 11H-10-(2-benzothiazolyl)quinolizino[9,9a,1gh]coumarin (C545T), and bathocuproine (BCP)	Spin-coating/ vdW	Hole injection and transport	Charge transfer supported by type II alignments	LED	[161]
MoS_2	NPB, Bathophenanthroline (Bphen), 4-tris(N-(2-naphthyl)-N-phenyl-	Spin-coating/ vdW	Electron injection and transport	Charge transfer supported by type II alignments	LED	[162]

	amino)triphenylamine /1,4-bis[N-(1-naphthyl)-N-phenylamino]-4,4-diamine/9,10-di(2-naphthyl)anthracene (ADN), and 1-4-di-[4-(N,N-di-phenyl)amino]styryl-benzene (DSA-ph)					
MoS_2	4-carboxybenzenediazonium tetrafluoroborate (4-CBD)	Dipping/ covalent	Tethering proteins to MoS_2	Carbon-sulfur (C-S) bonding	Biosensor	100
MoS_2	4-fluorobenzyl mercaptan and 5-pentanedithiol	Dipping/ covalent	Defect healing	Disulfide bonding	Catalyst	104
WSe_2	Diarylethene (DAE)	Spin-coating/ vdW	Photo-switching of carrier levels	Photoinduced charge transfer	Optical memory	78
WSe_2	Diarylethene (DAE)	Spin-coating/ vdW	Photo-switching of carrier levels	Photoinduced charge transfer	Optical memory	178
MoS_2	PTCDA	Molecular beam epitaxy/ vdW	Doping	Photoinduced charge transfer		94
WSe_2	Tetraene	Vapor deposition/ vdW	Observation of delocalized excitons in TMD/organic hybrids	Photoinduced charge transfer		138
MoS_2	PTCDA and 3,4,9,10-perylenetetracarboxyli	Vapor deposition/	Probing the effects of interfacial band- offset and	Charge transfer supported by type II alignments		139

	c diimide (PTCDI)	vdW	width on interlayer charge transfer			
MoS_2	P3HT and poly(N-9′-heptadecanyl-2,7-carbazole-alt-5,5-(4′,7′-di-2-thienyl-2′,1′,3′-benzothiadiazole)] (PCDTBT)	Spin-coating and dry transfer/ vdW	Investigating charge transfer dynamics in TMD/organic hybrids	Photoinduced charge transfer		140
MoS_2	(1,3,4,5,7,8-hexafluoro-tetracyano-naphthoquinodimethane (F_6TCNNQ))	Vapor deposition/ vdW	Exploring the effects of distinct charge transfer mechanisms in TMD/organic hybrids	Photoinduced charge transfer		141
WSe_2	Eosin Y (EY)	Dipping/ vdW	Doping	Dark-state doping and photoinduced charge transfer		34
MoS_2	Titanyl phthalocyanine (TiOPc)	Vapor deposition/ dipole-induced charge transfer	Defect healing	Dipolar interaction		93
$MoSe_2$	Pentacene	Dry transfer/ vdW	Enhancing PL intensity and tuning PL wavelength	Photoinduced charge transfer and dielectric screening on $MoSe_2$ exciton		111
MoS_2	Perylenetetracarboxylic dianhydride (PTCDA)	Vapor deposition/ vdW	Enhancing PL intensity of MoS_2	Resonant energy transfer		92
$MoSe_2$	2,3-diaminophenazine (DAP)	Vapor deposition/ vdW	Fabrication of a patterned structure	Charge transfer between metallic boundaries in $MoSe_2$ and DAP		95
$PtSe_2$	Pentacene	Molecular	Fabrication of a patterned	Charge transfer between 1H-		102

		beam epitaxy/ vdW	structure	$PtSe_2$ and pentacene		
MoS_2, $MoSe_2$, $MoTe_2$, WSe_2, and ReS_2	Oleamide	Spin-coating/ vdW	Fabrication of a patterned structure	Stronger binding interaction in the hybrid materials than the intermolecular interaction		[96]
MoS_2	Dodecanethiol and MPS	Dipping/ covalent	Defect healing	Disulfide bonding		[40]

Table 2. Working mechanisms and applications of multicomponent TMD/organic heterostructures

Hetero-structure	Molecular system	Method/ interaction	Purpose	Mechanism	Demonstrated application	Ref.
WSe_2/MoS_2 and MoS_2/WSe_2	TCNQ and EY	Dipping/ vdW	Control of IXs	Dark-state doping and photoinduced charge transfer		33
MoS_2/Wse_2	TCNQ, EY, cobalt phthalocyanine (CoPc), and 1,3-bis(3,5-dipyrid-3-ylphenyl)-benzene (B3PyPB)	Dipping/ vdW	Probing the effects of dielectric property, separation distance, and band alignment on IXs	Photoinduced charge transfer, dielectric screening, and dipolar interaction		90
$MoSe_2$/reduced graphene oxide (rGO)	Pentacene	Vapor deposition/ vdW	Enhancing PL intensity of $MoSe_2$	Photoinduced charge transfer		93
WSe_2/MoS_2	Poly(methyl methacrylate-co-methacrylic acid) (PMMA-coPMAA)	Spin-coating/ vdW	Doping	Dark-state doping	Ternary inverter	88
MoS_2/hexagonal boron nitride (hBN)	(5,6-dichloro-2[3-[5,6-dichloro-1-ethyl-3-(3-sulfopropyl)-2(3H)-benzimidazolidene]-1-propenyl]-1-ethyl-3-(3-sulfopropyl) benzimidazolium hydroxide) (TDBC)	Dipping/ vdW	Improving photosensitivity	Resonant energy transfer	Phototransistor	142
MoS_2/graphene	ZnPc	Dipping/ vdW	Facilitating photo-response	Dark-state doping and photoinduced charge transfer	Phototransistor	143
Graphene/MoS_2 /graphene	Bis (trifluoromethanesulfony	Drop casting/ vdW	Doping and exciton dissociation	Dark-state doping and photoinduced	Phototransistor	159

	l)-amide (TFSA) and triethylene tetramine (TETA)			charge transfer		
MoS_2/rGO	N , N′-Di(1-naphthyl)-N , N′-diphenyl-(1,1′-biphenyl)-4,4′-diamine (NPB), tris-(8-hydroxyquinoline)aluminum (Alq_3), 11H-10-(2-benzothiazolyl)quinolizino[9,9a,1gh]coumarin (C545T), and bathocuproine (BCP)	Spin-coating/ vdW	Hole injection and transport	Charge transfer supported by type II alignments	LED	164
MoS_2/rGO	Polyaniline (PANI)	Self-polymerization/ covalent chemistry	Electron injection and transport	Charge transfer supported by type II alignments	LED	165

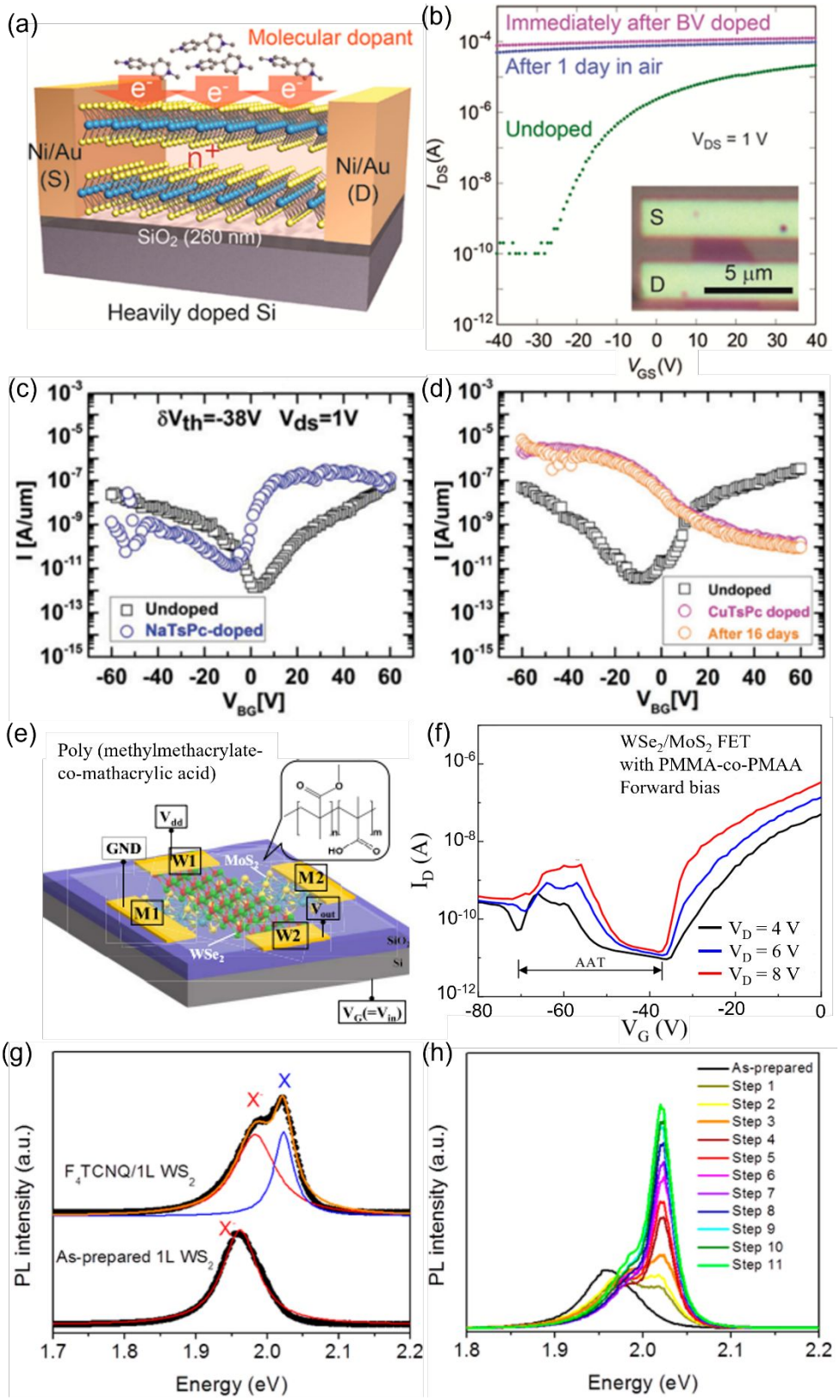

Figure 6. Doping effects on the optoelectronic properties of TMD/organic and TMD/TMD/organic hybrids. (a) Schematic illustration of a back-gated MoS_2 FET doped with BV molecules.[125] (b) Current-gate voltage plots of the devices with (green) and without BV doping (purple). The organic-layer-functionalized device kept in air for 1 day is also plotted in

blue.[125] The BV doped device exhibits higher currents under the same gate potential. Electrical transport characteristics of (c) Na_2TsPc-functionalized WSe_2 and (d) CuTsPc-attached MoS_2 FET.[126] (e) Schematic of the cross-type p−n heterojunction of WSe_2/MoS_2-based FET passivated with PMMA-coPMAA polymer.[94] (f) Current transport plot of WSe_2/MoS_2/PMMA-coPMAA devices under various source-drain voltage.[94] The hybrid FET exhibits the anti-ambipolar behavior in the gate potential range of $-71 \leq V_G \leq -37$ V. (g) PL spectra of 1L WS_2 with and without F_4TCNQ.[127] The molecular functionalization on the n-type WS_2 leads to a significant p-doping, which results in a balanced charge polarity in the TMD layer. The TMD hybrid exhibits both the exciton- and the trion emission at ~2.05 and ~1.95 eV, respectively. In contrast, the as-prepared WS_2 layer only emits the trion PL at ~1.95 eV due to the electron-rich nature. (h) Emission spectra of WS_2 under consecutive F_4TCNQ doping.[127] The emission intensity increases with increased doping due to the balanced populations of electrons and holes. Figures 6a-6b, 6e-6f, and 6g-6h have been adapted from ref. 125, 94, and 127, respectively, with permission from the American Chemical Society: ref. 125, copyright 2014; ref. 94, copyright 2020; and ref. 127, copyright 2014. Figures 6c and 6d reproduced from ref. 126 with permission from the Royal Society of Chemistry, copyright 2018.

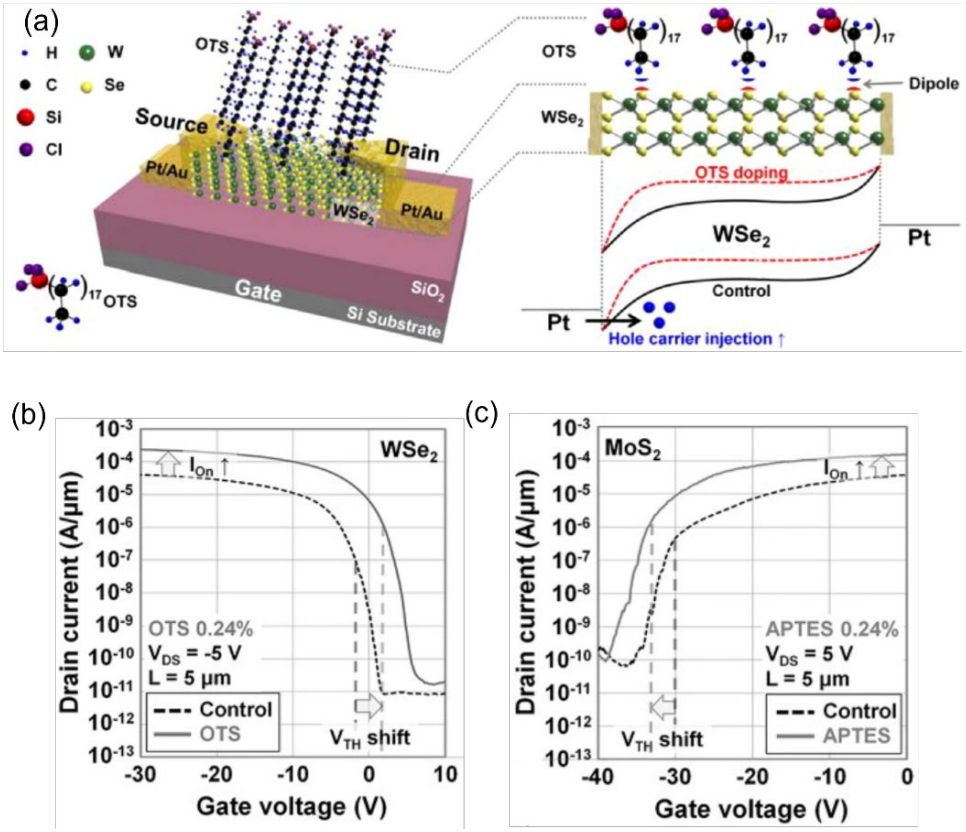

Figure 7. Dipole-induced doping in organic-integrated TMDs. (a) Schematic of dipolar molecule attached WSe_2 FET along with corresponding energy band diagram.[130] Current transport characteristics of (b) OTS/WSe_2 and (c) APTES/MoS_2 FETs, where OTS induces a p-doping and APTES leads to an n-doping.[130] Reproduced from ref. 130 with permission from Wiley, copyright 2015.

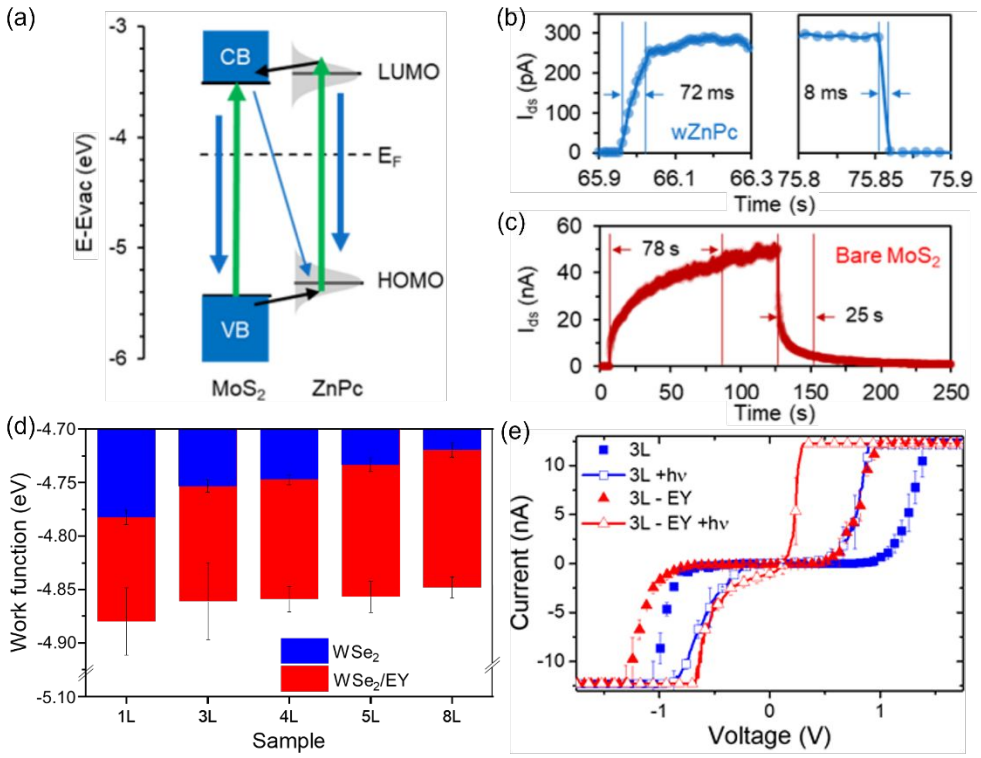

Figure 8. Photoinduced charge transfer facilitated by the type II band alignment. (a) Schematic of the band alignment for MoS_2/ZnPc.[137] The photoresponse of (b) ZnPc-applied MoS_2 and (c) pristine MoS_2 plotted in the electric current versus time.[137] Due to the exciton dissociation at the interface, MoS_2/ZnPc shows a faster response than the pristine MoS_2. (d) Work functions of pristine WSe_2 and WSe_2/EY hybrids with various layer numbers of WSe_2.[34] EY withdraws electrons from WSe_2, resulting in a decrease of the work functions. (e) Current (filled objects) and photocurrent (open objects) of 3L WSe_2 (blue) and 3L WSe_2/EY (red).[34] A greater photocurrent is observed with the organic-attached TMD. Figures 8a-8c and 8d-8e have been reproduced from refs. 137 and 34, respectively, with permission from the American Chemical Society, copyright 2018 and Wiley, copyright 2019.

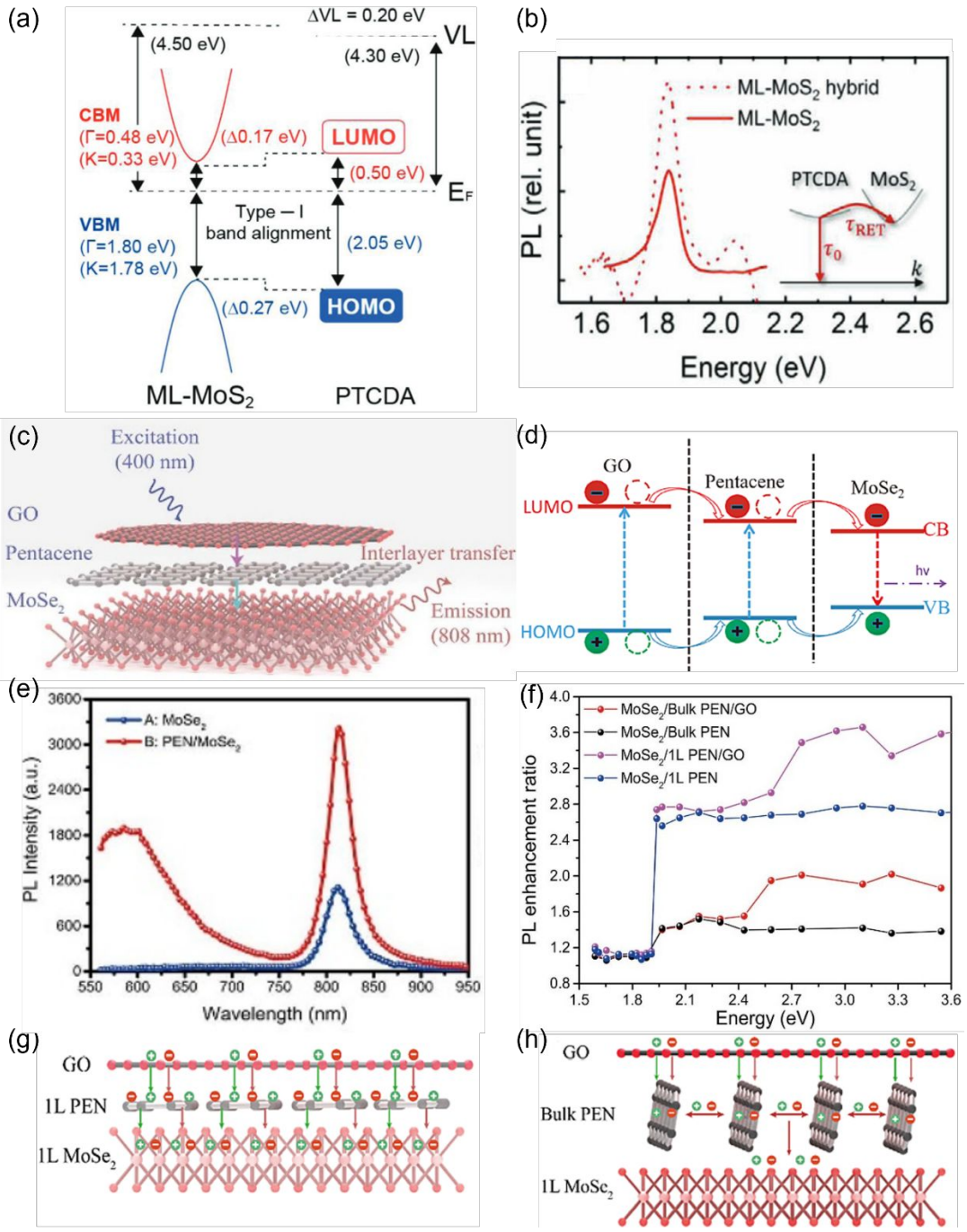

Figure 9. Resonant energy transfer in type I (straddling) alignments. (a) Type I energy band diagram and (b) PL spectra of a hybrid MoS_2/PTCDA junction.[98] The PL intensity of the MoS_2/PTCDA hybrid is normalized with that of pristine MoS_2, demonstrating an increase by a factor of 2 with the organic functionalization.[98] (c) Schematic of $MoSe_2$/pentacene/GO hybrid structure and (d) corresponding energy band diagram.[93] (e) PL spectra of $MoSe_2$ and pentacene-attached $MoSe_2$. The hybrid structure shows a greater $MoSe_2$ PL peak at ~820 nm than the pristine flake due to the organic-to-TMD energy transfer.[93] (f) PL enhancement chart of $MoSe_2$/1L-pentacene and $MoSe_2$/bulk-pentacene with and without the GO layer as a function

of excitation energy.[93] The $MoSe_2$/pentacene/GO hybrid structures exhibit the greatest enhancement under the excitation energies above 2.5 eV. Schematics of energy transfer processes in (g) 1L and (h) bulk pentacene-inserted $MoSe_2$/GO layers.[93] Figures 9a-9b and 9c-9h have been adapted from refs. 98 (permission from Wiley, copyright 2021) and 93 (permission from the IOP publishing group, copyright 2021), respectively.

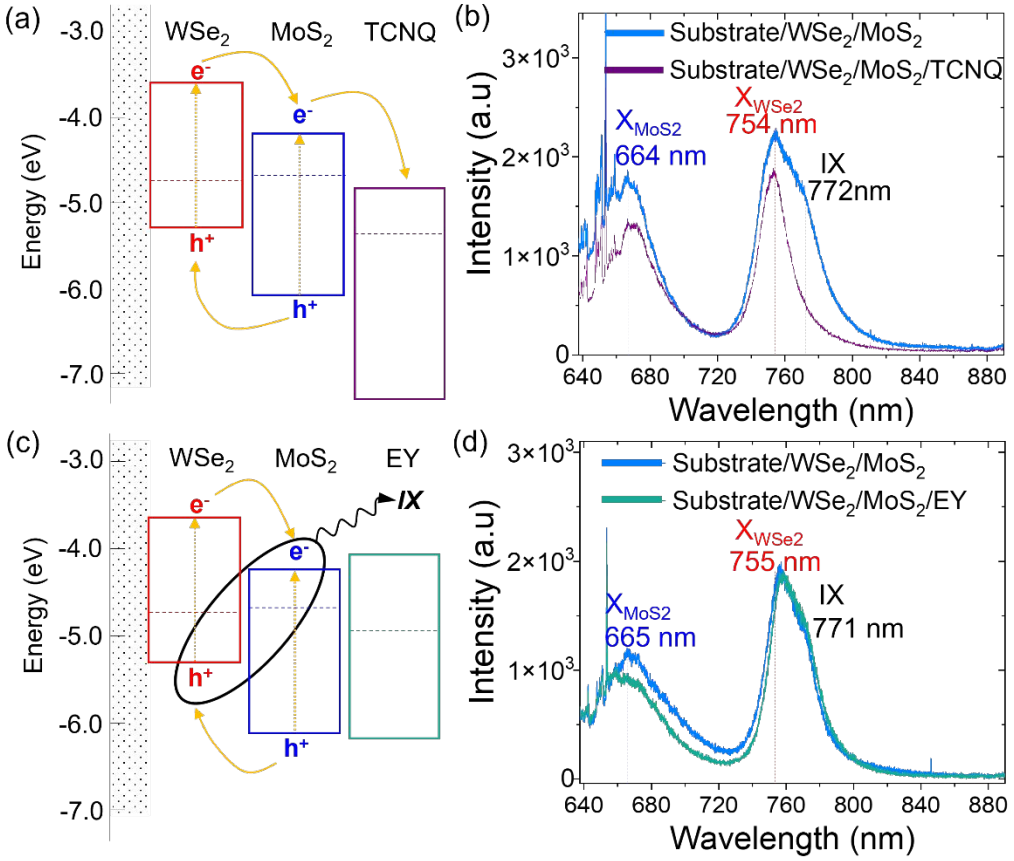

Figure 10. Photoinduced interlayer charge transfer in multi-layered hybrid structures. (d) Schematic and (e) PL spectra of consecutive type II/type II $WSe_2/MoS_2/TCNQ$. The interfacial charge transfer in the consecutive type II/type II band leads to a drastic quenching of IX emission.[33] (f) Schematic and (g) PL spectra of dissimilar type II/type I $WSe_2/MoS_2/EY$ hybrids.[33] Unlike $WSe_2/MoS_2/TCNQ$, the EY-layer-integrated WSe_2/MoS_2 shows the unchanged IX, as the dissimilar energy level alignments prevent the interlayer charge transfer to the organic layer. Reproduced from ref. 33 with permission from the American Chemical Society, copyright 2020.

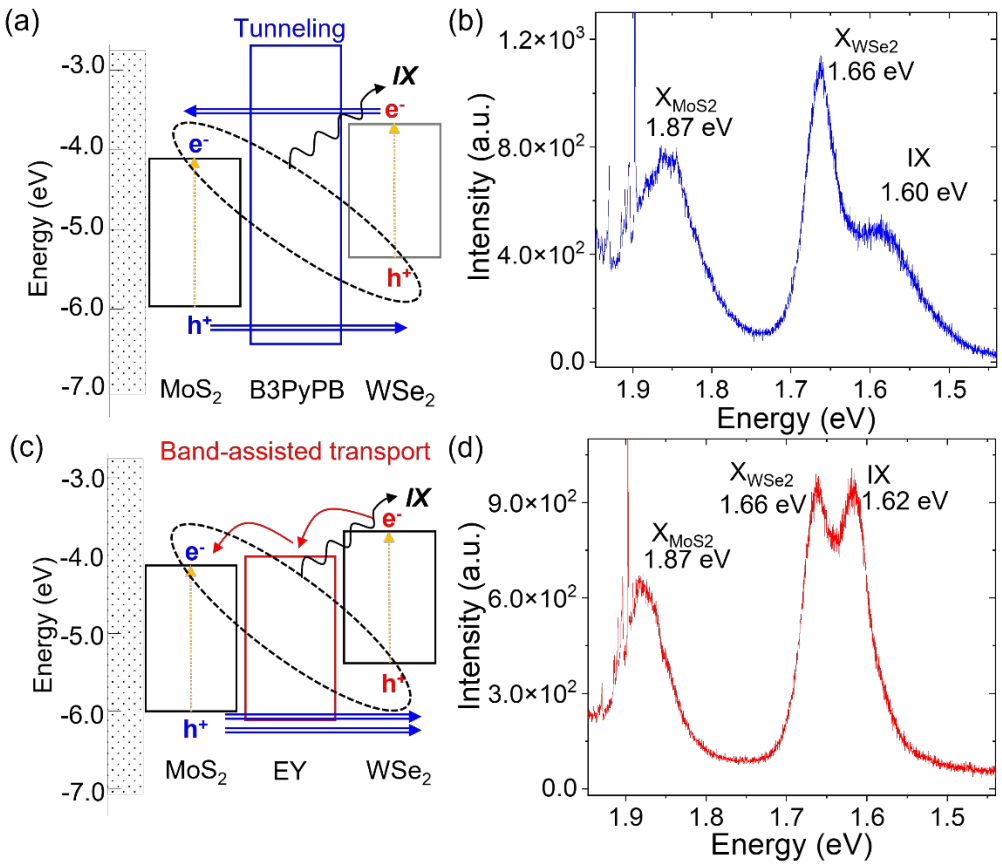

Figure 11. Band-alignment-dependent behaviors of interlayer excitons. Energy band diagrams of (a) B3PyPB and (c) EY inserted MoS_2/WSe_2 hybrid structures.[90] Tunneling of photogenerated charges is the predominant mechanism in MoS_2/B3PyPB/WSe_2, while MoS_2/EY/WSe_2 facilitates photoinduced electron transfer. PL spectra of (b) B3PyPB and (d) EY inserted MoS_2/WSe_2 heterobilayers.[90] Note that the IX emission peak (at ~1.60 eV) of MoS_2/B3PyPB/WSe_2 is blueshifted from the control $MoSe_2/WSe_2$ (at ~1.55 eV). The blueshift may be attributed to the reduced dielectric screening and the increased separation distance in IX. Besides, the EY layer may enhance the dipolar interaction of IX. As a result, the EY-inserted sample shows the IX emission at ~1.62 eV, which is blueshifted by ~25 meV from that of MoS_2/B3PyPB/WSe_2. Reproduced from ref. 90 with permission from the American Chemical Society, copyright 2021.

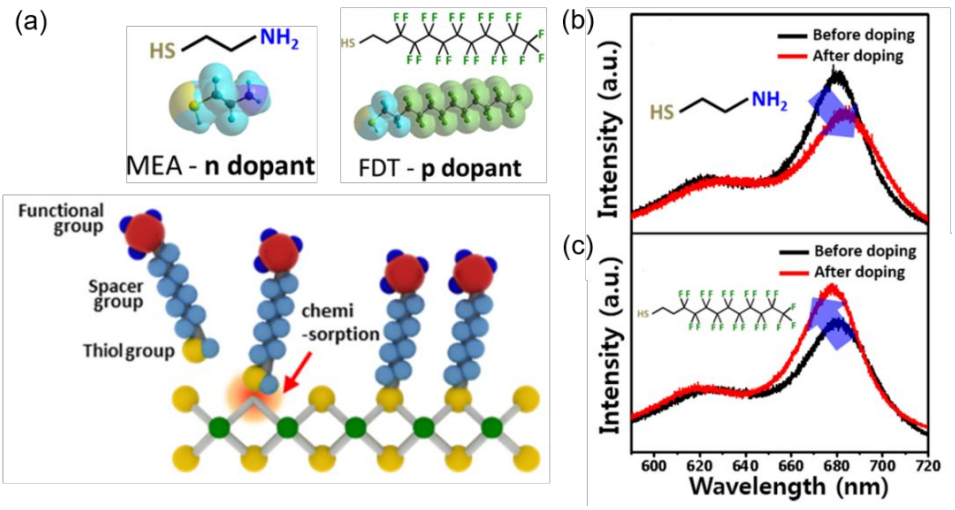

Figure 12. Defects-induced molecular functionalization. (a) Schematics of MEA and FDT molecules and their defect-healing process on TMDs.[39] PL spectra of (b) MEA and (c) FDT treated MoS_2.[39] Reproduced from ref. 39 with permission from the American Chemical Society, copyright 2015.

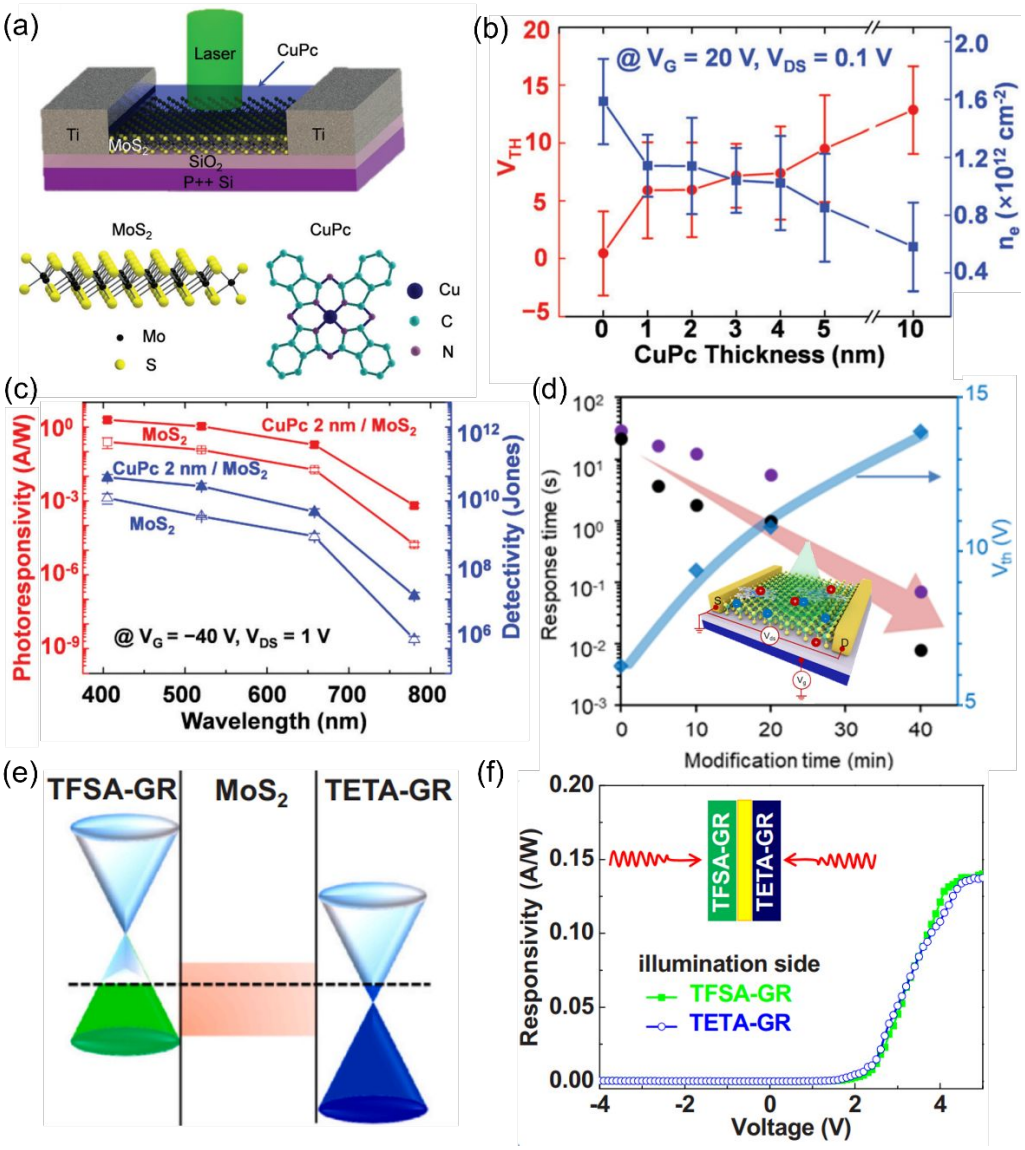

Figure 13. Phototransistors made of TMD/organic hybrids. (a) Schematic of a CuPc-integrated MoS_2 phototransistor.[155] (b) Threshold voltage (red) and carrier concentration (blue) of the MoS_2 phototransistors with various thicknesses of CuPc.[155] As the CuPc layer thickens, the threshold voltage transitions from ~0 V to ~12 V. (c) Photoresponsivity and detectivity of MoS_2/CuPc hybrid layers.[155] (d) Photoresponse time (left axis) and threshold voltage (V_{th}, right axis) of MoS_2/ZnPc.[137] Here, the black and the purple dots indicate the rise and the decay time to turn on and off the MoS_2/ZnPc phototransistor, respectively. The blue dots represent the threshold voltage of the device. As more ZnPc molecules are attached on the MoS_2 flake with increased incubation time, the hybrid exhibits a faster response time and a greater threshold voltage. (e) Schematic band diagram and (f) bias-dependent photoresponsivity of TFSA-graphene/MoS_2/TETA-graphene.[159] Figures 13a-13c (ref. 155), 13d (ref. 137), and 13e-13f (ref.159) have been reproduced with permission from the Royal Society of Chemistry

(copyright 2015), the American Chemical Society (copyright 2018), and Elsevier (copyright 2021), respectively.

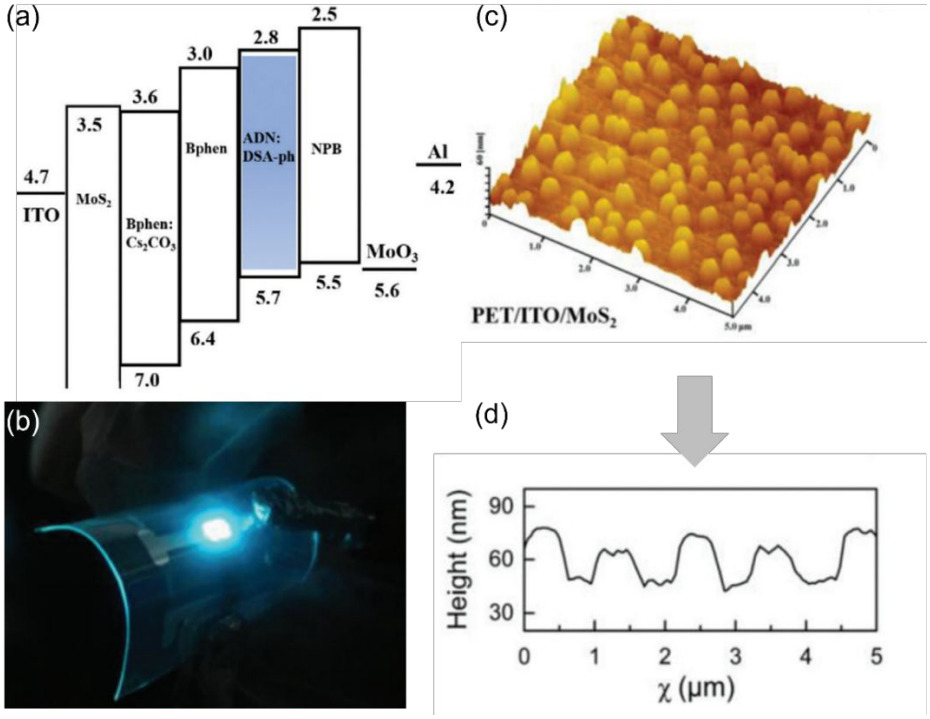

Figure 14. Inorganic-organic light emitting diodes (IOLEDs). (a) Band diagram and (b) photograph of MoS_2-based IOLED.[162] The deice is bendable and emits blue light.[162] (c) AFM image and (d) height profile of a thermally deposited MoS_2 film on an ITO substrate. As the thermal expansion coefficient of the ITO substrate is different from that of MoS_2, the MoS_2 layer fractures during the deposition. As a result, the cracked MoS_2 layers may form individual islands on the substrate and grow vertically. The nanopillars exhibit an average height of ~30 nm. The pillars may suppress the internal reflection and thus improve the electroluminescence of the device.[162] Reproduced from ref. 162 with permission from the Royal Society of Chemistry, copyright 2017.

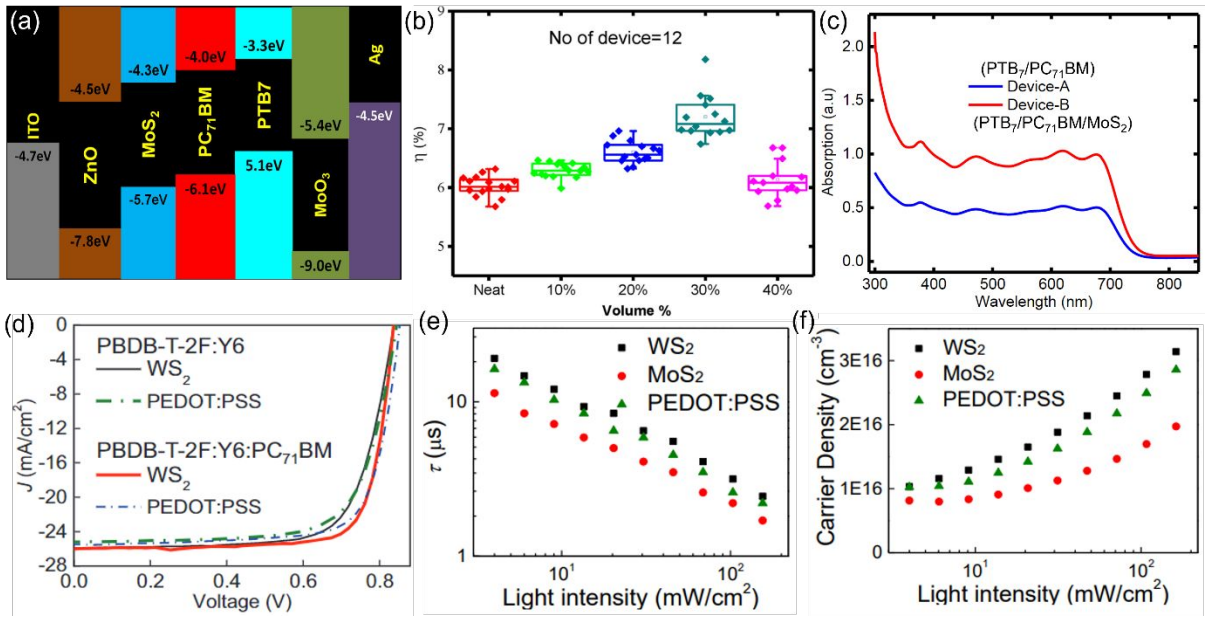

Figure 15. High performance photovoltaics. (a) Energy level alignments of PTB7/$PC_{71}BM$/MoS_2-based photovoltaics.[172] (b) Efficiency distribution of the composites with different volume ratios of MoS_2.[172] (c) Absorption spectra of PTB7/$PC_{71}BM$ (Device A) and PTB7/$PC_{71}BM$/MoS_2 (Device B).[172] (d) Current density-voltage plots of PBDB-T-2F:Y6 and PBDB-T-2F:Y6:PC71BM photovoltaics with different HTLs: WS_2 and PEDOT:PSS.[174] (e) Charge carrier lifetime (τ) and (f) carrier density as a function of light intensity.[174] WS_2 has a longer lifetime than the other two samples. With an extended lifetime, WS_2 offers the largest carrier density, resulting in an outstanding PCE (17 %). Figures 15a-15c and 15d-15f have been reproduced from refs. 172 and 174, respectively, with permission from Elsevier, copyright 2017 and Wiley, copyright 2019, respectively.

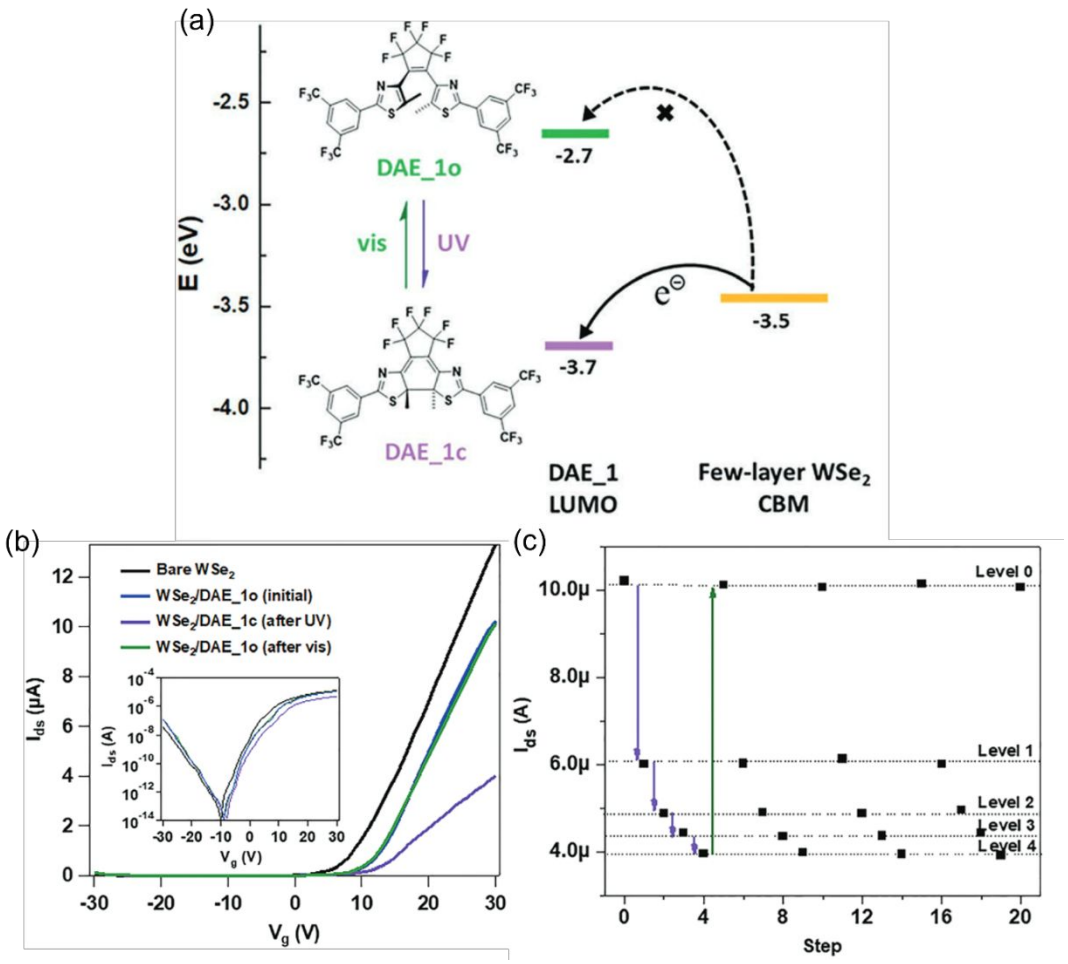

Figure 16. Optical memories operated by the interaction between photochromic DAE molecules and TMDs. (a) Energy diagram of few-layer WSe_2 CBM as well as open (DAE_1o) and closed (DAE_1c) conformations of DAE. The DAE may switch between two isomers by illuminating Vis and UV light, and the energy level is modulated accordingly.[178] (b) Electrical transport plots of pristine WSe_2 and WSe_2/DAE.[178] Due to the interlayer charge transfer, WSe_2 with closed DAE after UV light illumination (marked as 'after UV' in Figure 16b, purple) demonstrates a smaller current than the as-prepared WSe_2/DAE (represented as 'initial' in the figure, blue) under the same gate voltage. In contrast, DAE may turn to be open state after Vis light irradiation ('after Vis' in the figure, green). Thus, the Vis-light-illuminated device shows the almost same current-voltage response with the as-prepared sample. (c) Multi-level current modulation with different illumination durations.[178] Reproduced from ref. 178 with permission from Wiley, copyright 2019.

Table 3. Energy applications based on binary or ternary TMD-organic hetero-materials.

Hybrid material	Method	Structure	Application	Performance	Ref.
MoS_2/PANI	Chemical exfoliation and self-polymerization	Plates	Supercapacitor	Energy density (ED, Wh/kg): ~3.8 and power density (PD, W/kg): ~2,000	200
MoS_2/PANI	Solvothermal synthesis and self-polymerization	Hollow spheres	Supercapacitor	ED: ~32 and PD: ~320	191
MoS_2/CeO_2C-MOF	Solvothermal synthesis and blending	Plates and flower-like structures	Supercapacitor	ED: ~35 and PD: ~667	205
MoS_2/Ni-MOF	Solvothermal synthesis	Flower-like structures	Supercapacitor	ED: ~73 and PD: ~375	202
$MoSe_2$/rGO	Solvothermal synthesis	Sphere-decorated plates	Supercapacitor	ED: ~6.9 and PD: ~260	198
$MoSe_2$/rGO	Solvothermal synthesis	Plates and flower-like structures	Supercapacitor	Specific capacitance (SC, F/g): 211	199
MoS_2/Fluoroelastomer	Chemical exfoliation and self-polymerization	Plates	Supercapacitor	ED: ~3.15 mWh/cm^3 and PD: N/A	197
MoS_2/Multi-walled-CNT/PANI	Solvothermal synthesis and self-polymerization	Flower-like structures woven with tubular networks	Supercapacitor	SC: ~540	192
MoS_2/MnO_2/PANI	Chemical exfoliation and Solvothermal synthesis	Tubular networks	Supercapacitor	ED: ~36 and PD: ~500	193
MoS_2/WO_3/GO	Solvothermal synthesis	Plates and flower-like structures	Supercapacitor	SC: ~836	208
MoS_2/carbon black/ polyindole	Chemical exfoliation and self-polymerization	Plates-decorated spheres	Supercapacitor	SC: ~440	194
MoS_2/MoO_3/polypyrrole (PPy)	Chemical exfoliation and self-polymerization	Plates-decorated spheres	Supercapacitor	SC: ~352	258
WSe_2/rGO/NiFe-OH	Solvothermal synthesis and blending	Porous plates	Supercapacitor	ED: ~45 and PD ~8,00	206
MoS_2/rGO/PANI	Solvothermal synthesis and self-polymerization	Plates	Supercapacitor	ED: ~22 and PD: ~5,000	207
CNT/ZIF/MoS_2	Ultrasonication and	Plates connected with	Supercapacitor	ED: ~50 and PD: ~3,700	188

	solvothermal synthesis	carbon networks			
MoS_2/CNT/rGO	Solvothermal synthesis	Flower-like structures-decorated plates	Supercapacitor	ED: ~4 μWh/cm^2 and PD: ~3 mW/cm^2	204
MoS_2/PPy	Solvothermal synthesis	Spheres	HER catalyst	Tafel slope (TS, mV/dec): ~29 and over potential (OV, mV in absolute value): ~30	222
MoS_2/N-ZIF	Solvothermal synthesis	Plates	HER catalyst	TS: ~57 and OV: ~185	223
MoS_2/rGO	Solvothermal synthesis	Plates and flower-like structures	HER catalyst	TS: ~48 and OV: ~100	47
MoS_2/CoS_2/polyoxometalate-based metal–organic polymer	Solvothermal synthesis	Tubular networks	HER catalyst	TS: ~87 and OV: ~65	220
$MoSe_2$/GO	Solvothermal synthesis and blending	Plates	HER catalyst	TS:~57 and OV: ~180	218
$MoSe_2$/rGO	Solvothermal synthesis	Plates and flower-like structures	HER catalyst	TS:~47 and OV: ~121	219
MoS_2/TiO_2/MOF	Solvothermal synthesis	Flower-like structures	HER catalyst	TS:~120 and OV: ~300	221
MoS_2/MOF	Solvothermal synthesis	Urchin-like structures	HER photocatalyst	Photoinduced hydrogen production rate (PHR): ~55 μM/hour	227
MoS_2/pyrene-based polymer	Solvothermal synthesis and blending	Flower-like structures	HER photocatalyst	PHR: ~27 μM/hour	228
WSe_2/PANI	Chemical exfoliation and self-polymerization	Plates	HER photocatalyst	TS:~120 and OV: ~190	226
MoS2/rGO/$Cd_{0.6}Zn_{0.4}S$	Solvothermal synthesis	Plate-decorated spheres	HER photocatalyst	PHR: ~12 mM/hour·g	48
MoS_2/$Cu_{0.9}Co_{2.1}S_4$-ZIF	Solvothermal synthesis	Flower-like structures	HER photocatalyst	PHR: ~40 mM/hour·g	229
MoS_2/CdS/Ni_2P-ZIF	Solvothermal synthesis	Plate-decorated spheres	HER photocatalyst	PHR: ~73 mM/hour·g	225

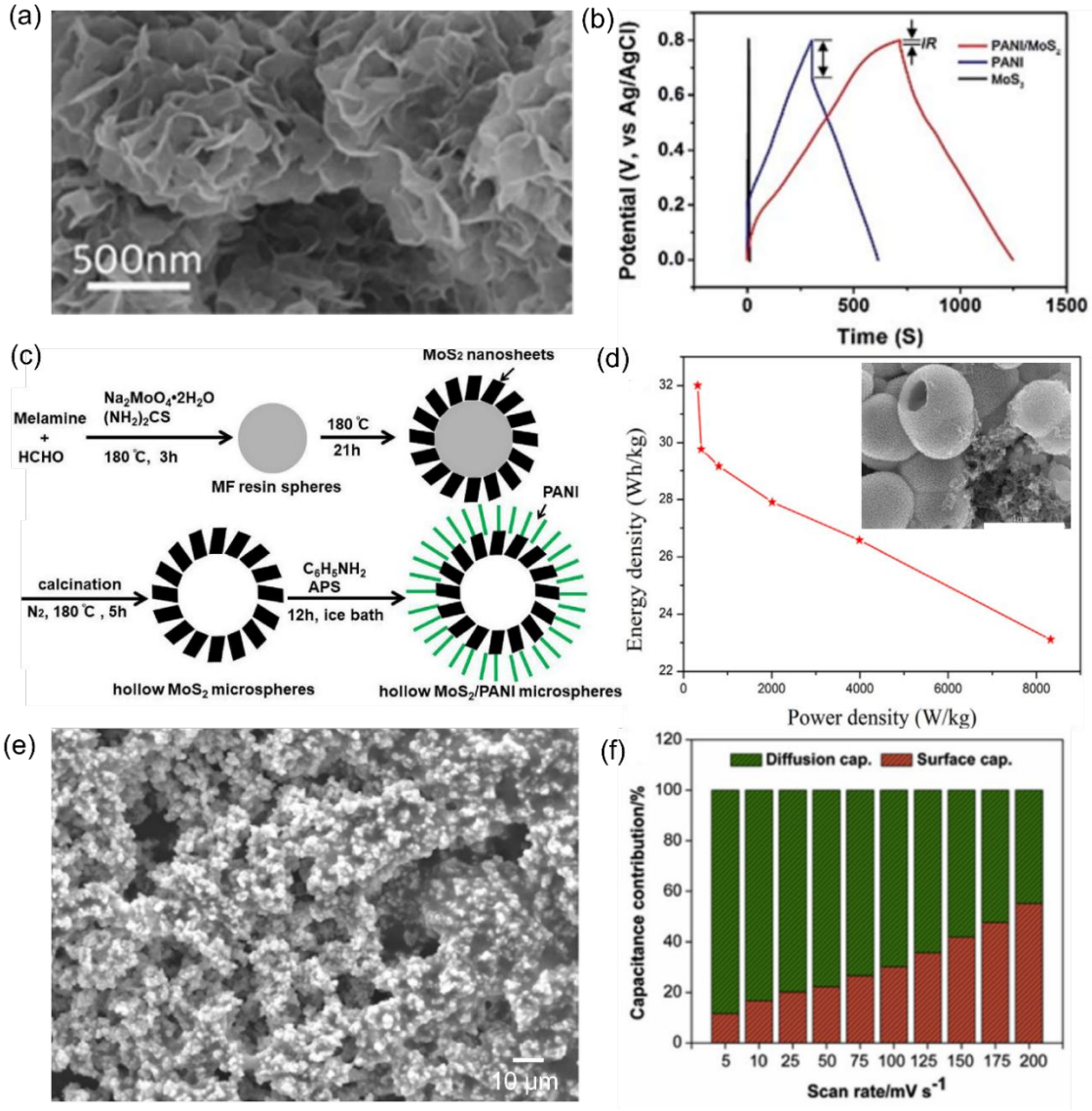

Figure 17. Supercapacitor electrodes made of topochemically synthesized various TMD hybrids. (a) SEM image of flower-like MoS_2 nanostructure, where the TMD layers were synthesized with a solvothermal process.[182] The nanostructure exposes its edges (petal-like structures) to the surrounding, where the edges of MoS_2 may behave as electrochemically active sites.[182] (b) GCD curves of MoS_2, PANI layer, and PANI/MoS_2 samples at a current density of 0.6 A/g.[200] The nanocomposite offers the greatest specific capacitance of ~400 F/g and the highest energy density of ~4.7 Wh/kg. (c) Schematic of topochemically synthesized MoS_2/PANI composite.[191] (d) Performance curves of the MoS_2/PANI hollow sphere. The inset shows an SEM image of the MoS_2/PANI structure (scale bar = 4 μm).[191] Due to the engineered topology, the electrode consisting of the hollow sphere hybrids exhibits an outstanding energy density of ~32 Wh/kg. (e) SEM image of MoS_2-CeO_2/C hybrid.[205] (f) Capacitance contributions (diffusion- and surface-controlled processes) of the MoS_2/MOF composite as a function of scan rate.[205] Figures 17a and 17b have been adapted from refs. 182 and 200,

respectively, with permission from the Royal Society of Chemistry (ref. 182, copyright 2015 and ref. 200, copyright 2016). Figures 17c-17d and 17e-17f have been adapted from refs. 191 and 205, respectively, with permission from Elsevier (ref. 191, copyright 2019 and ref. 205, copyright 2020).

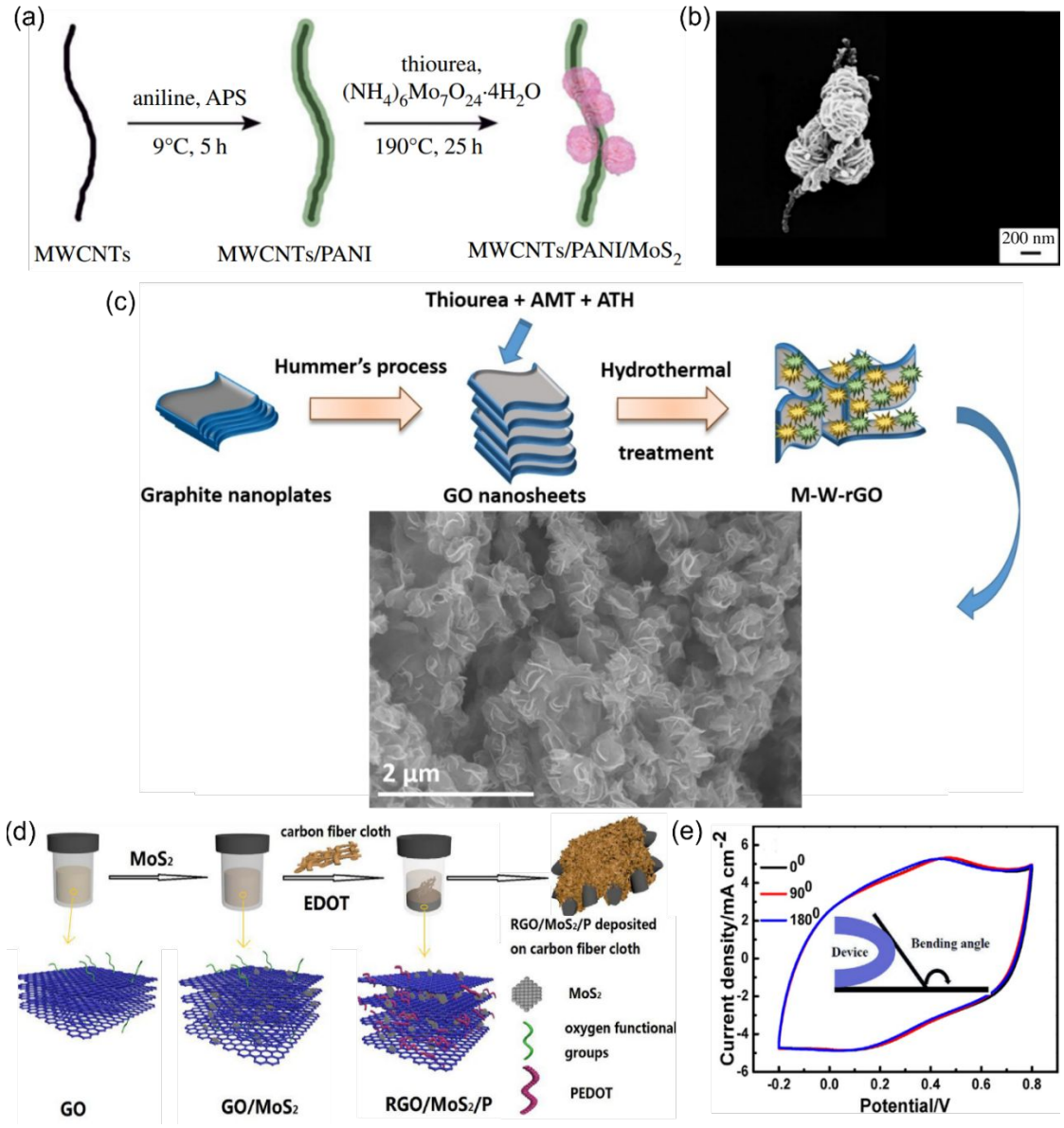

Figure 18. Supercapacitor electrodes made of ternary composites. (a) Scheme and (b) SEM image of MWCNTs/PANI/MoS_2 composite.[192] The nanostructure demonstrates a stem-flower-like structure, where MWCNTs/PANI serves as a conductive scaffold of the composite and MoS_2 decorates the architecture as a charge accumulating layer. (c) Schematic illustration of a MoS_2/GO/WO_3 hybrid electrode with an SEM image of the composite.[208] The large GO plates are surrounded with small MoS_2 and WO_3 flakes. (d) Synthesis processes of GO/MoS_2/PEDOT composite.[195] A multilayered GO structure includes MoS_2 and PEDOT nanosheets. (e) Current-voltage responses of the GO/MoS_2/PEDOT electrode with and without deformation.[195] The supercapacitor shows consistent CV response regardless of the applied mechanical stress. Figures 18a-18b (ref. 192), 18c (ref. 208), and 18d-18e (ref. 195) have been adapted with permission from the Royal Society (copyright 2018), Wiley (copyright 2019), and Elsevier (copyright 2020), respectively.

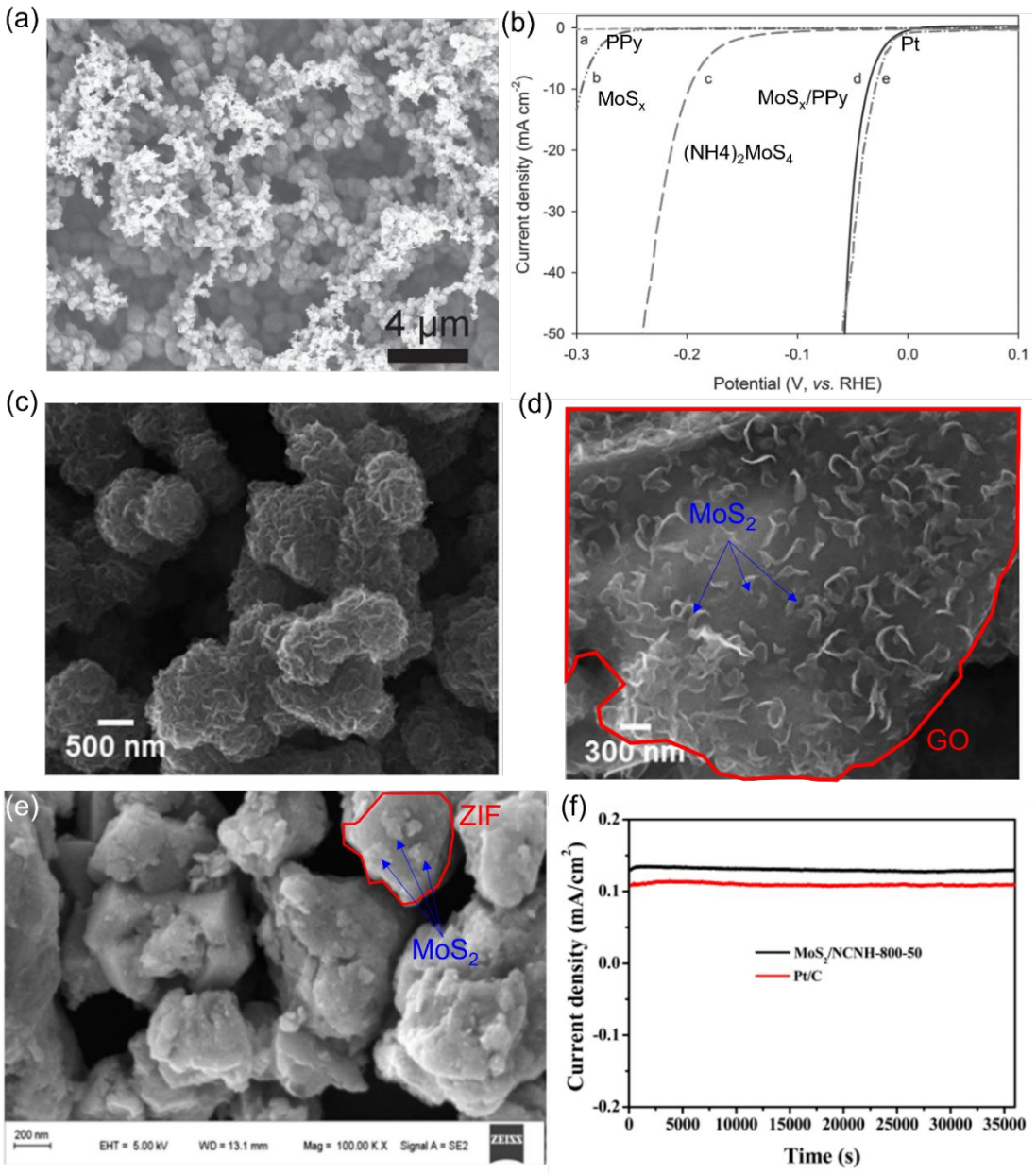

Figure 19. Hydrogen evolution reaction assisted by catalytic effects. (a) SEM image of a MoS_x/PPy electrode.[222] The spherical features are the agglomerated MoS_x and PPy. (b) Polarization curves of various electrodes made of PPy, MoS_x, $(NH_4)_2MoS_4$, MoS_x/PPy, and Pt.[222] The MoS_x/PPy exhibits a current-voltage response comparable to that of a Pt electrode. TEM images of (c) MoS_2 nanoball structure and (d) petal-decorated MoS_2/GO nanosheets.[47] (e) SEM image of MoS_2/ZIF. The small and thin MoS_2 plates are attached to the ZIF structure.[223] (f) Chronoamperometric curves of the MoS_2/ZIF composite and Pt electrodes.[223] In the plot, NCNH-800-50 represents the ZIF. Figures 19a-19b (ref. 222), 19c-19d (ref. 47), and 19e-19f (ref. 223) have been reproduced with permission from Wiley (copyright 2014), the Royal Society of Chemistry (copyright 2017), and the American Chemical Society (copyright 2017), respectively.

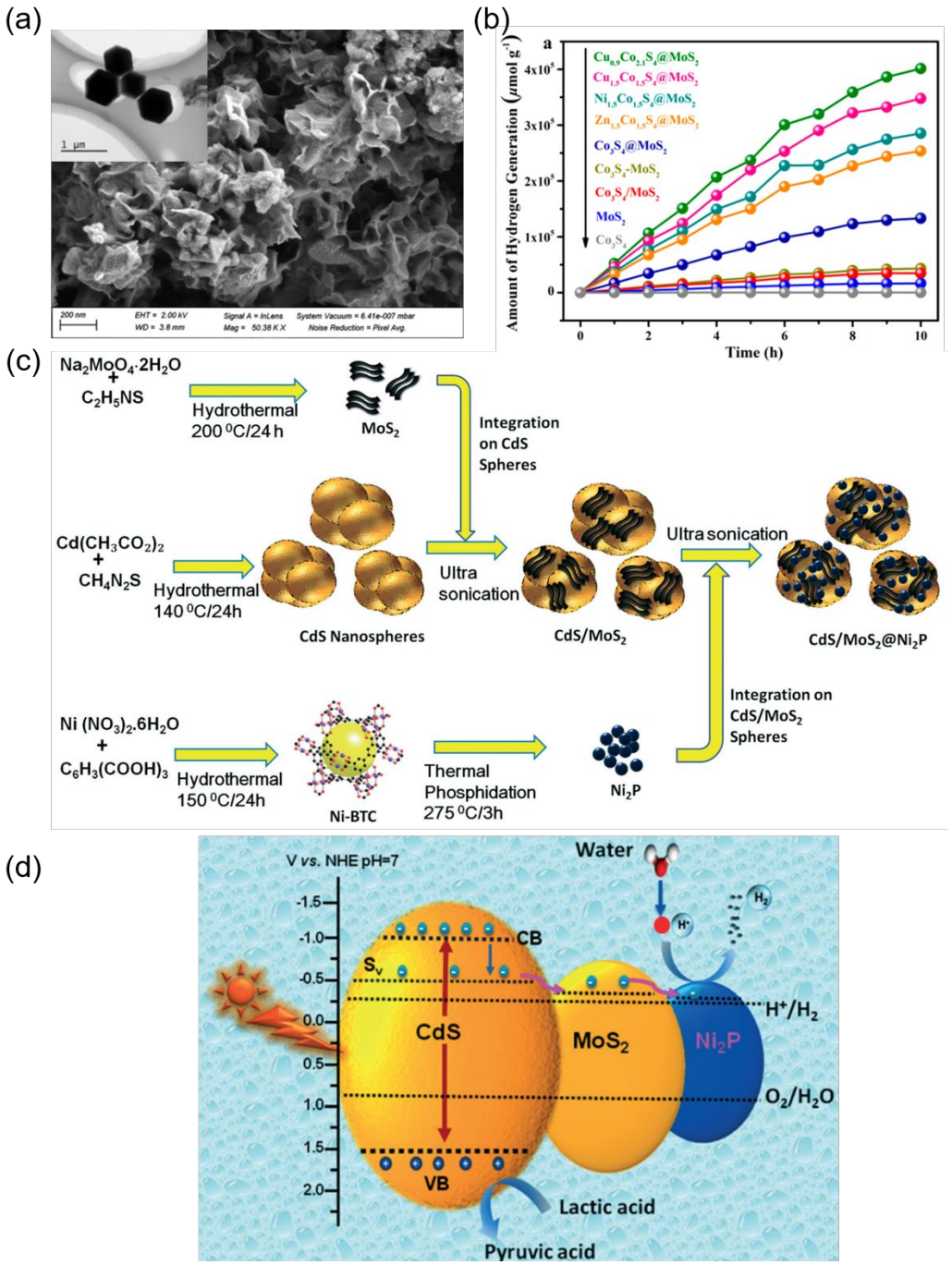

Figure 20. Photocatalytic hydrogen evolution reaction. (a) SEM image of as-synthesized $Cu_{0.9}Co_{2.1}S_4$-ZIF/MoS_2 hybrid.[229] The inset in the image shows hexagonal Cu-based ZIF structures without MoS_2. (b) Photocatalytic hydrogen evolution plots of different materials.[229] Among the various ZIF composites with different core metal ions, $Cu_{0.9}Co_{2.1}S_4$/MoS_2 demonstrates the best performance of hydrogen generation. (c) Schematics of the synthesis processes for MoS, CdS, Ni_2P, and CdS/MoS_2/Ni_2P nanocomposites. (d) Energy diagram of CdS/MoS_2/Ni_2P nanocomposites, where the excited electrons in CdS are transferred to Ni_2P.[225] The CB, VB, and S_v indicate the energy levels of conduction band, valance band, and sulfur

vacancy state of CdS, respectively. Figures 20a-20b and 20c-20d have been reproduced from refs. 229 and 225, respectively, with permission from the American Chemistry Society (copyright 2019) and the Royal Society of Chemistry (copyright 2017), respectively.